ВІСНИК
КИЇВСЬКОГО НАЦІОНАЛЬНОГО УНІВЕРСИТЕТУ ІМЕНІ ТАРАСА ШЕВЧЕНКА

ISSN 1728-2306

РАДІОФІЗИКА ТА ЕЛЕКТРОНІКА 14/2010

Засновано 1999 року

Публікуються результати експериментальних і теоретичних досліджень у галузях фізичної електроніки, фізики плазми, фізики поверхні твердого тіла, емісійної електроніки, кріогенної та мікроелектроніки, нанофізики та наноелектроніки, високотемпературної надпровідності, квантової радіофізики, функціональної електроніки, твердотільної електроніки, мобільного зв'язку, медичної радіофізики, методів отримання діагностичної інформації та її комп'ютерної обробки.

Для науковців, викладачів вищої школи, студентів.

Experimental and theoretical contributions are published in the following fields: physical electronics, plasma physics, solid-state surface physics, emission electronics, cryogenic electronics, microelectronics, nanophysics and nanoelectronics, high-temperature supercondactive electronics, solid-state electronics, functional electronics, microwave electronics, quantum electronics, mobile communication, medical radiophysics, methods of receipt and computer processing of diagnosis information

Designed for researches, university teachers, students.

ЗМІСТ

CONTENTS

UDC 004.4

I. Bilokon, stud., D. Gryaznov, assist.,
S. Pogorilyy, Doct. Sci.

BUILDING OF DYNAMICALLY RECONFIGURABLE COMPUTING ARCHITECTURE USING VIRTUALIZATION TECHNOLOGIES

Запропоновано концепцію побудови динамічно реконфігурованої кластерної обчислювальної архітектури на базі платформи віртуалізації Microsoft Hyper-V. Побудовано обчислювальний кластер згідно розробленого принципу. Розроблено систему керування обчислювальним кластером, вузлами якого є віртуальні машини.

Ключові слова: динамічно реконфігурована обчислювальна система, обчислювальний кластер, віртуалізація, віртуальна машина, Hyper-V, гіпервізор, SAN, iSCSI, WMI, API, HPC, MPI.

The concept of building of dynamically reconfigurable cluster computing architecture based on Microsoft Hyper-V virtualization platform was suggested. A computing cluster according to the concept was constructed. A management system for computing cluster with virtual machine nodes was developed.

Keywords: dynamically reconfigurable computing system, computing cluster, virtualization, virtual machine, Hyper-V, hypervisor, SAN, iSCSI, WMI, API, HPC, MPI.

Introduction. A widespread implementation of parallel computing technologies has led to a wide range of implementations built using various tools and based on different technologies. Accordingly, these software tools have various degrees of parallelism implemented and make a wide range of requirements for cross node, cross process and cross thread communication. Therefore, urgent problem is the construction of collective computing resource that meets the needs of a wide range of computing tasks and belongs to dynamically reconfigurable systems.

This paper proposes the concept of implementation of dynamically reconfigurable systems based on virtualization technology. Using virtual machines as computing nodes allows dynamically computing system architecture changing without hardware modifications. This concept allows building a computing system which optimally uses available computing hardware resources and designed for collective usage by tasks that have different requirements for the number of nodes, processors, computational kernels and communications between them.

Typically, in most organizations personal computers (PCs) are not used about 70% of the time. Taking into account that computing power of PC processors is almost equal to a capacity of server ones (because in most cases they are built on the same kernels and have the same frequency), and for Local Area Network organizing we could use widespread Gigabit Ethernet technology (it meets bandwidth and delay requirements for MPI protocol exchange network), we can conclude about the feasibility of deploying dynamically reconfigurable computing systems based on computer lab of organization.

Modern hardware and software virtualization technologies. Today there are two main types of architectures that are used for server virtualization. The fundamental difference between them concerns relationship between the level of virtualization and physical facilities. In architectures of the first type operating system (OS) runs on the same level as virtualization platform (VP). This approach is associated with significant system resources consuming and therefore not applicable for workloads. The second type of architectures provides the level of VP directly above the equipment level, below the OS level. To improve performance in VP which use this approach, there is a special layer between guest OS and hardware – hypervisor, or Virtual Machine Monitor, which allows guest OS directly use hardware resources. Using hypervisor, which is the link layer between guest OS and equipment, significantly increases the performance, bringing it to physical platform performance.

There are two types of hypervisor – microkernelized and monolithic. The monolithic hypervisor approach hosts the hypervisor/VMM in a single layer that also includes most of the required components, such as the kernel, device drivers, and the I/O stack. This is the approach used by such a solutions as VMware ESX and traditional mainframe systems.

The microkernelized approach uses a very thin, specialized hypervisor that only performs the core tasks of ensuring partition isolation and memory management. This layer does not include the I/O stack or device drivers. This is the approach used by Hyper-V. Using the microkernelized hypervisor architecture, Hyper-V has very low CPU overhead, leaving plenty of resources to virtualize workloads. Hyper-V enables virtual machines (VM) to take advantage of multicore and multiprocessor technology (up to four virtual processors per VM and up to 16 logical processors on host computer) and large amounts of memory, and consolidate 32-bit and 64-bit workloads on a single system. Quick Migration ability allows moving a running VM from one host to another in a few seconds. Abilities of Hyper-V mentioned above motivated to choose it as a VP for computing cluster.

Computing cluster components. Components of a computing cluster, which nodes are virtual machines on the Microsoft Hyper-V platform (CCVM) are:

- CCVM main node.
- CCVM physical nodes (hosts) containing virtual nodes.
- CCVM nodes which are VM.
- Storage Area Network (SAN).
- CCVM Management Infrastructure.

CCVM main node. CCVM main node (MN) is managing node of the cluster. It contains the necessary hardware and software for task management and cluster usage. The necessary requirement for CCVM to work properly is MN high availability.

It is supposed that CCVM MN has Microsoft Windows 2008 Server x64 OS. In addition to OS CCVM MN should contain all the elements of Management Infrastructure.

Minimum hardware requirements are made by CCVM main node's software. Minimum system requirements are:

- 1.5 GB of RAM.
- Intel or AMD CPU with x64 architecture.
- Gigabit Network Interface Card.
- At least 100 GB of disk space.

Physical nodes. CCVM physical nodes (PN) are actually a basis for virtual nodes (VN) operation. They should include required hardware and software and should to be connected via high speed connection lines (Gigabit Ethernet). An environment for VM operation is Microsoft Hyper-V, which is distributed as part of Microsoft Windows 2008 Server x64, or as a separate Microsoft Hyper-V Server Core OS.

Generally, PN system requirements are determined by quantity and quality of VM, which are in working state simultaneously. Minimum requirements for a single VN full work:

- Multicore x64 CPU architecture with Intel-VT or AMD-V hardware virtualization technology support.
- Appropriate chipset.
- At least 2 GB of RAM.
- Sufficient hard disk space.
- Gigabit Network Interface Card.

CCVM virtual nodes. VM for CCVM nodes are major executive component of the system. Therefore they must sustain intended workloads and properly interact with each other and with Management System. Accordingly, VN hardware and software requirements are made.

VN software should provide maximum control for nodes, task management capabilities by means of HPC Server 2008, communication between nodes via MPI protocol. Therefore following software requirements are made:

- Microsoft Windows Server 2008 x64 OS.
- Hyper-V Integration Components.
- HPC Server 2008 Integration Services including services to support interaction via MPI.

VN must have hardware that is adequate to intended workloads and provides network connectivity between VN. Here are the minimum system requirements for stable OS and all necessary components operation without requirements for specific tasks:

- Virtual CPU with x64 architecture.
- 1 GB of RAM.
- Virtual bridge to communicate with physical network equipment.
- Sufficient Virtual Hard Drive.

SAN for computing cluster. CCVM SAN provides necessary facilities and services for data storage, sharing and manipulation during computation process. There are several SAN technologies for today. Specifics of CCVM operation make a series of requirements to SAN:

- Sufficient storage and data transmission speed.
- High stability and error detections.
- Ability to stay working after some time of connection inactivity.
- High availability.

Consider using iSCSI SAN technology, because it fully satisfies these requirements, has OS-level support and requires quite simple deployment process. iSCSI SAN lays on a standard Ethernet network infrastructure equipment and communications environment. Application servers contain integrated iSCSI Initiators, which initiate requests to disk arrays, which in turn are iSCSI Targets. iSCSI Targets include user partitions (UP) to allow users to store their information and results.

CCVM Management Infrastructure. For CCVM management there are two necessary key components: means for VN and VP management and means for task management.

For VM based on Microsoft Hyper-V platform Microsoft gives following management tools:

- Hyper-V Management Console.
- System Center Virtual Machine Manager (SCVMM).
- Windows Management Instrumentation (WMI).

Hyper-V Management Console is a standard graphical user interface (GUI) for VM and VP management, which is a part of the OS. Its significant disadvantage is the lack of VM bulk control within Local Area Network (LAN) and absence of VM Quick Migration tools.

SCVMM is a separate commercial product for managing virtual infrastructure of organization. SCVMM allows managing all aspects of VP. Among the shortcomings of SCVMM as CCVM management tool there is the absence of a convenient user interface for VM bulk management.

WMI allows VP management via execution of WMI scripts or any other application that implements interaction with this interface.

For task management there are Microsoft HPC Server 2008 software package. The package is designed to convert common PC infrastructure to computing cluster. Its main functions are: computing task installations to cluster nodes, tasks management and monitoring, cluster nodes monitoring. The software package also provides services that allow solving the problem of automated deployment of the cluster.

Software tools and interfaces mentioned above allow management of different CCVM aspects and components not functionally related to each other. Manipulation of the cluster as a whole requires controls that integrate VM and VP management tools and task management tools as well. So it is important task to create a common CCVM management tool that allows managing all aspects of the cluster system.

CCVM management tool. Since CCVM infrastructure consists of a number of software products and interfaces, for convenience of cluster nodes handling, allocation of resources managing, tasks and nodes monitoring, user accounts and access policies managing it is necessary to develop a common CCVM management GUI (MGUI). This software must satisfy following requirements:

- Unified user interface for all CCVM aspects handling, such as PN, VM, Microsoft Hyper-V, tasks that are running on the cluster and so on.
- PN and VN bulk management and monitoring ability within LAN.
- Tasks bulk monitoring and controlling ability.
- User accounts and CCVM resources access policies management ability.
- Ability to protect the cluster from intentional or accidental injury by means of OS.

To meet the above-described requirements the application should interact with following components: Microsoft Hyper-V, Microsoft HPC Server 2008, Microsoft Windows 2008 Server OS of every PN and VN. Such interaction is performed via Application Program Interfaces (API). Let's consider the API of each listed component.

Microsoft HPC Server 2008 API. The usage of services provided by Microsoft HPC Server 2008 could be implemented by using .NET objects after linking corresponding dynamic linking libraries (DLL) that are distributed within the software package. So you can make all the operations that allow HPC GUI software in your application. Various reporting information can be obtained by accessing relevant SQL databases located on MN as a part of Microsoft HPC Server 2008. In addition to listed facilities the software package provides a number of utilities that can be invoked from the command line with arguments to perform some actions.

Microsoft Hyper-V API. The only API of VP Microsoft Hyper-V is WMI. WMI technology is one of the cornerstones Microsoft technologies for centralized management and supervision of various components of a computer network running Windows. This is the realization of management model based on the Web (Web-Based Enterprise Management, WBEM). In the context of WBEM Common Information Model (CIM) was proposed, which represents the structure of a computer system as a single scalable object-oriented model that is supported in WMI.

Each resource managed through WMI, has corresponding class. Each class has properties, methods and qualifiers. Also every property and method can have its own qualifiers too. Full path to the CIM class has the following structure:

\\ComputerName\Namespace:ClassName.KeyProperty1=Value1,KeyProperty2=Value2 ...

Where ComputerName – network name of computer (to indicate the local computer you can use the "." symbol); Namespace – namespace name; ClassName – class name; KeyProperty1 = Value1, KeyProperty2 = Value2 ... – list of object's key-value pairs "property = value".

When WMI event fires an instance of the class which corresponds to this event is automatically created. External events are represented by __ExtrinsicEvent class, timer events – __TimerEvent class, and internal events – __NamespaceOperationEvent, __ClassOperationEvent and __InstanceOperationEvent classes. In order to create an external event that event should be supported by appropriate WMI provider.

Internal events allow monitoring state changes of managed resources which are represented by particular WMI class. Events related to managed resources has corresponding classes that are inherited from the __InstanceOperationEvent class. Those classes are __InstanceCreationEvent, __InstanceModificationEvent and __InstanceDeletionEvent that responsible for creating, changing and deleting an instance of class. For event notification subscription a special type of query language WQL is used.

In addition to API it is possible to use command-line utilities such as, for example, a utility to make VM desktop connection – vmconnect.exe.

PN and VN OS API. In order to perform interaction with PN and VN Microsoft Windows 2008 OS there are a number of interfaces and services, cooperation with which is involved into modules of most of modern high-level programming languages and tools. Services that are not implemented as modules or dynamic libraries can be used directly through the Windows API or WMI.

In addition to listed means for interaction with VN Microsoft Windows 2008 OS Hyper-V provides integration components (IC), which support time synchronization, Volume Shadow Copy Service (VSS), shutting down guest (VM) OS, key-value pairs exchange (is used to access guest OS Registry), OS identification.

The architecture's block diagram is shown in Fig. 1. Solid lines with arrows mark system components interaction. Dotted lines indicate the interaction between elements through appropriate interfaces, dotted lines with arrows mark interaction inside components. Bold lines mark management infrastructure units developed in this paper.

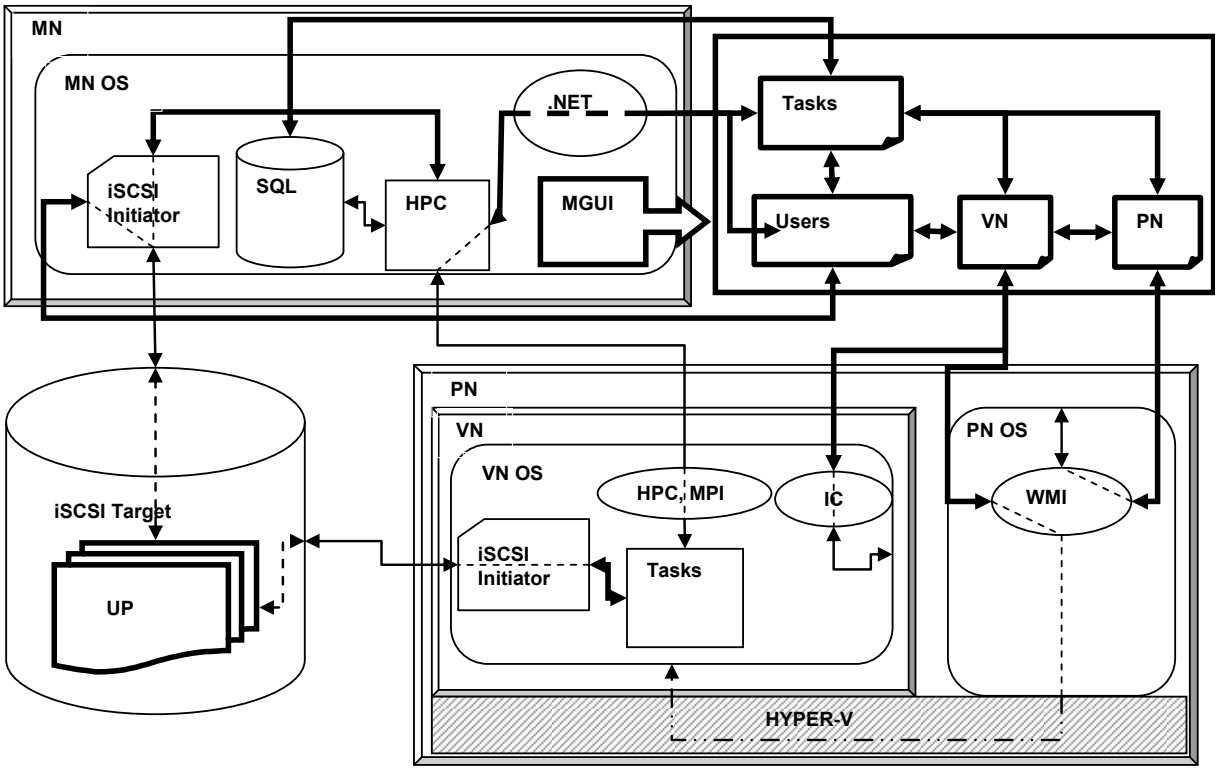

Fig. 1. The proposed architecture's block diagram

According to the proposed concept CCVM based on the computer class of Microsoft IT Academy in Information and Computing Centre of Taras Shevchenko National University of Kyiv was built. During development process a prototype of CCVM MGUI that implements interaction with corresponding components via interfaces, services and utilities above mentioned, was created. As a programming language C# had been chosen, GUI had been created by means of Windows Presentation Foundation (WPF) technology.

Summary. As a result of comparative analysis of modern computing technologies and software that was made the urgency of dynamically reconfigurable architecture creation problem were proved.

The proposed technique, based on modern virtualization technologies, enables creation of dynamically reconfigurable computing architecture that meets considerable amount of requirements that software makes to computer system.

The developed computing system with dynamically reconfigurable architecture based on virtualization technologies proved its effectiveness and efficiency during its usage in Taras Shevchenko National University of Kyiv.

1. Білоконь І., Грязнов Д., Мар'яновський В. Створення захищеного обчислювального windows-кластеру на платформі desktop PC // Вісник Київського університету імені Тараса Шевченка. Радіофізика та електроніка. Вип. 12. – К., 2009. 2. Погорілий С. Д., Бойко Ю. В., Грязнов Д. Б., Ломакін О. Д., Мар'яновський В. А. Концепція створення гнучких гомогенних архітектур кластерних систем // Проблеми

програмування. : Матер. шостої міжнар. наук.-практ. конф. з програмування "УкрПРОГ `2008", 27-29 трав. Україна, Київ, 2008. 3. Мережа розробників компанії Microsoft (Microsoft Developer Network, MSDN). – Доступ до сайту: http://msdn.microsoft.com 4. Технічна документація по платформі Microsoft Hyper-V. – Доступ до документів: http://technet.microsoft.com/en-us/library/cc753637%28WS.10%29.aspx 5. Технічна документація Microsoft HPC Server 2008. – Доступ до документів: http://www.microsoft.com/hpc/en/us/white-papers.aspx

Submitted on 1.04.10

PACS 73.61.Cw, Ng

A. Buianin, post grad. stud., V. Ilchenko, Ph. D., O. Tretyak, Doct. Sci

CAPACITANCE-VOLTAGE DEPENDENCES MODELLING FOR SIO_2/SI-NCS/SIO_2/SI STRUCTURES

Modeling of capacitance-voltage characteristics for metal-dielectric-semiconductor contact with siicon nanoclusters layers inbuilded in isolator has been carried out. Physical model of structure, which can explain the negative differential capacitance appearance have been created. Influence of the quantum states formed on the interfases of silicon clusters has been investigated.

Key words: silicon nanoclusters, negative differential capacitance, capacitance-voltage characteristic.

Проведено моделювання вольт-фарадних характеристик для контакту метал-діелектрик-напівпровідник з вбудованими в діелектрик шарами кремнієвих кластерів. Побудовано фізичну модель структури, яка дозволяє пояснити виникнення в них негативної диференціальної ємності. Досліджено вплив на цей ефект квантових станів, що виникають на інтерфейсах кремнієвих кластерів.

Ключові слова: кремнієві нанокластери, негативна диференціальна ємність, вольт-фарадна характеристика.

Introduction. In recent years, investigation of silicon nanoclusters (Si-NCs) properties, formed in SiO_2 using different technological methods, causes increased scientists attention because of the prospect of new nanoelectronic devices creation based on them [1-3]. With the structures SiO_2/Si-NCs/SiO_2/Si formed by methods of Si ion implantation in dielectric [4], memory effects have been successfully obtained and created light emitting diodes [5]. The literature describes the successful obtaining of the same structures using thermal conversion methods of SiO_X layers enriched by silicon [6]. This technology has certain advantages in terms of its compatibility with a standard silicon technology, that's why the use of thermal methods for creation of structures with silicon clusters in silicon oxide are the most actual and promising in nowadays.

This work is devoted to capacitance-voltage characteristics modeling of these structures and investigation of influence of nanoclusters and quantum states, which are formed at their interfaces, on temperature dependences of capacitance-voltage characteristics (CVC) for SiO_2/Si-NCs/SiO_2/Si structure. These calculations were performed for the constant AC test signal frequency.

Physical model. Capacitance-voltage characteristics of structures, which contain nanoformations of another material, have been deeply analyzed in the literature previously [9],[10],[11]. The specific feature of structure investigated in this paper is that the silicon clusters in it surrounded by silicon oxide from all sides, and their creation during annealing and formation processes occurred simultaneously throughout the dielectric volume. Since nanoclusters have had developed interface at Si-SiO_2 border, the main influence on potential profile creation in dielectric, surely, was caused by charge, accumulated most on their interfaces. This fact was taken into account in physical model using discrete silicon layers placement in silicon oxide only at certain distances L_{CL_n} from the dielectric-semiconductor border. This idealization was used only for the discretization of the numerical calculations. To simplify the calculations of potential profile in this structure it was assumed that the spatial distribution of silicon clusters can be represented as the delta functions. Besides, the statistical redistribution of nanocluster sizes was not considered in these calculations. In addition, it should be noted, that unlike the structures with quantum dots, which were built in the semiconductor in which typically dopant was present, in these structures additional charge, distributed in dielectric, was not considered. Thus, the simulation was done in assumption that the main influence on potential spatial distribution in dielectric causing only by electric charge, which was accumulated on quantum levels in dielectric.

The main objective, which was needed to be done to solve the task, was obtaining of a universal dependence of potential distribution from coordinates along the entire structure for any quantity of silicon nanocluster layers placed in dielectric.

In order to be able to calculate impact of one nanoclusters layer, it is needed to write down Poisson's equation and add the appropriate boundary conditions:

а) potential is required to be equal to zero at space-charge region (SCR) boundary in semiconductor;

б) electrical field is required to have a zero value at this boundary.

Get the following equations system:

$$\begin{cases} \dfrac{d^2\varphi}{dx^2} = -\dfrac{eN_{CV}}{\varepsilon_1\varepsilon_0}\theta(x-L_{SiOx}) + \dfrac{en_{CL}}{\varepsilon_2\varepsilon_0}\delta(x-L_{CL}) \\ \varphi(w) = 0 \\ \left.\dfrac{d\varphi}{dx}\right|_{x=w} = 0 \end{cases} \quad (1)$$

It can be seen from equations system (1) that, in the right side of Poisson's equation, charge density consists of two components: charge density of ionized impurity:

$$\rho_{bulk} = -\frac{eN_{CV}}{\varepsilon_1\varepsilon_0}\theta(x-L_{SiOx}), \quad (2)$$

where is $\theta(x-L_{SiOx})$ – Heaviside function, which takes the following values for investigated structure:

$$\theta(x-L_{SiOx}) = \begin{cases} 1, x > L_{SiOx} \\ 0, x < L_{SiOx} \end{cases} \quad (3)$$

Assume for definiteness that the semiconductor is n-type, so the charge of ionized donor impurity is positive, which is constant in semiconductor volume(homogeneously alloyed semiconductor). However it should be noted that the impurity is not distributed in dielectric. The second component is a density of charges, which accumulate at states in the cluster. These states are appeared due to dimensional quantization and lead to the creation of spatial quantization and discrete spectre in the cluster. The special fact is that all these states are localized in space, that's charges can only exist in a given point in space with some given energy, so the charge density in clusters can be recorded by δ-function:

$$\rho_{CL} = \frac{en_{CL}}{\varepsilon_1\varepsilon_0}\delta(x-L_{CL}), \quad (4)$$

where is n_{CL} – surface charges density in silicon clusters and the Dirac delta-function has a dimension of 1/sm.

The solution of equations system (3) as follows:

$$\frac{d\varphi}{dx} = \begin{cases} -\frac{eN_{CV}}{\varepsilon_2\varepsilon_0}(x-w), x > L_{SiOx} \\ \frac{eN_{CV}}{\varepsilon_1\varepsilon_0}(w-L_{SiOx}), L_{CL} < x < L_{SiOx} \\ \frac{eN_{CV}}{\varepsilon_1\varepsilon_0}(w-L_{SiOx}) - \frac{en_{CL}}{\varepsilon_1\varepsilon_0}, x < L_{CL} \end{cases}, \quad (5)$$

$$\varphi(x) = \begin{cases} -\frac{eN_{CV}}{2\varepsilon_2\varepsilon_0}(x-w)^2, x > L_{SiOx} \\ -(x-L_{SiOx})\frac{eN_{CV}}{\varepsilon_1\varepsilon_0}(w-L_{SiOx}) + \\ +\frac{eN_{CV}}{2\varepsilon_2\varepsilon_0}(x-w)^2 + \Delta\varphi, L_{CL} < x < L_{SiOx} \\ -\frac{eN_{CV}}{\varepsilon_1\varepsilon_0}(w-L_{SiOx})(x-L_{SiOx}) \\ +\frac{eN_{CV}}{2\varepsilon_2\varepsilon_0}(L_{SiOx}-w)^2 + \frac{en_{CL}}{\varepsilon_1\varepsilon_0}(x-L_{CL}) \\ +\Delta\varphi, x < L_{CL} \end{cases} \quad (6)$$

Thus, the potential distribution was obtained for structures with one silicon clusters layer embedded in dielectric. The presence of silicon clusters layer leads to appearance of a summand $\frac{en_{CL}}{\varepsilon_1\varepsilon_0}(x-L_{CL})$ in a formula. It is the silicon clusters influence on potential distribution in the structure. After a similar calculations for structures with 2, 3, … n silicon clusters layers , it was noticed that the presence of an additional silicon clusters layer at a certain distance from the contact border leads to appearance of the same summands for each layer. Therefore, as a result of this calculation, the universal formula for n silicon clusters layers in dielectric was obtained:

Silicon clusters influence is determined by the presence of summand $\sum_{m=1}^{k}\frac{en_{CL_m}}{\varepsilon_1\varepsilon_0}(x-L_{CL_m})$ in a formula (7). Knowing the exact number of silicon clusters layers located in the dielectric, potential distribution for such structure can be calculated.

$$\varphi(x) = \begin{cases} -\frac{eN_{CV}}{2\varepsilon_2\varepsilon_0}(x-w)^2, x > L_{SiOx} \\ \frac{eN_{CV}}{2\varepsilon_2\varepsilon_0}(L_{SiOx}-w)^2 - (x-L_{SiOx})\times \\ \times\frac{eN_{CV}}{\varepsilon_1\varepsilon_0}(w-L_{SiOx}) + \Delta\varphi, L_{CL_1} < x < L_{SiOx} \\ \frac{eN_{CV}}{2\varepsilon_2\varepsilon_0}(L_{SiOx}-w)^2 - \frac{eN_{CV}}{\varepsilon_1\varepsilon_0}(w-L_{SiOx})\times \\ \times(x-L_{SiOx}) - \sum_{m=1}^{k}\frac{en_{CL_m}}{\varepsilon_1\varepsilon_0}(x-L_{CL_m}) + \\ +\Delta\varphi, L_{CL_{m+1}} < x < L_{CL_m} \end{cases} \quad (7)$$

It should be noted that this is only mathematical idealization of potential distribution and this formula is only approximately describes the potential distribution in the structure.

Fig.1 depicts potential distribution for the structure with the five silicon clusters layers located at equal distances from each other.

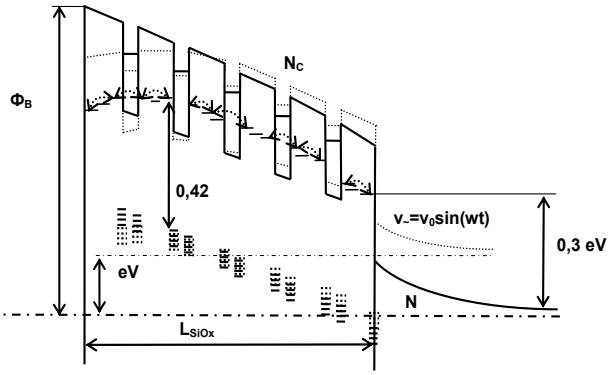

Fig.1. Potential distribution in the space charge region

Under high reverse biases applied to the contact, the Fermi level E_f would be located below the cluster energy level E_{CL}. That is why states in clusters will be free of charge, i.e. $n_{CL} = 0$. During the reducing of reverse bias applied to the contact, Fermi level E_f will be approaching to E_{CL}, that will lead to filling up of additional states in clusters, i.e. n_{CL} will be increasing in accordance with Fermi-Dirac statistic:

$$n_{CL_n}(V_{CL_n}) = N_{CL_n}\frac{1}{1+\exp(\frac{E_F - E_{CL_n} - eV_{CL_n}}{kT})}, \quad (8)$$

where is N_{CL_n} – effective concentration of silicon clusters for a certain layer embedded in a dielectric layer (it is considered for simplyfing, that at any one point can be only one electron); V_{CL} – is a part of voltage attached to the structure, that falls in the plane with n-th silicon clusters layer.

For the structure with two silicon clusters layers embedded in dielectric, voltage potential at a distance L_{CL_2} from contact border was found. This value can be found after substituting the $x = L_{CL_2}$ value in formula (7) for two silicon clusters layers:

$$\begin{aligned} &\varphi(L_{CL_2}) = \frac{eN_{CV}}{2\varepsilon_2\varepsilon_0}(L_{SiOx}-w)^2 - \frac{eN_{CV}}{\varepsilon_1\varepsilon_0}(w-L_{SiOx})\times \\ &\times(L_{CL_2}-L_{SiOx}) - \frac{en_{CL_1}}{\varepsilon_1\varepsilon_0}(L_{CL_2}-L_{CL_1}) - \frac{en_{CL}}{\varepsilon_1\varepsilon_0}(L_{CL_2}-L_{CL_2}) + \\ &+\Delta\varphi = \frac{eN_{CV}}{2\varepsilon_2\varepsilon_0}(L_{SiOx}-w)^2 - \frac{eN_{CV}}{\varepsilon_1\varepsilon_0}(w-L_{SiOx})(L_{CL_2}-L_{SiOx}) - \\ &-\frac{en_{CL_1}}{\varepsilon_1\varepsilon_0}(L_{CL_2}-L_{CL_1}) + \Delta\varphi \end{aligned} \quad (9)$$

As it can be seen, the first clusters layer existence and voltage changing on it, are affect voltage value in the plane with the second silicon clusters layer.

To find the voltage value that falls exactly in the palne of the clusters, it is necessary to find potential value at the point $x = L_{CL_2}$ under different applied biases. After this the difference of these potentials under $V = 0$ and $V \neq 0$ can be found, and this gives us necessary voltage value:

$$V_{CL_2} = \varphi^V(L_{CL_2}) - \varphi^0(L_{CL_2}), \quad (10)$$

Let's find the voltage, which is falls on all SCR. At the position $x = 0$ for formula (7) in the case of two silicon clusters layers, receive:

$$-\Phi_B + V = \frac{eN_{CV}}{2\varepsilon_2\varepsilon_0}(L_{SiOx} - w)^2 - \frac{eN_{CV}}{\varepsilon_1\varepsilon_0}(w - L_{SiOx}) \times \\ \times L_{SiOx} + \frac{en_{CL_1}}{\varepsilon_1\varepsilon_0}L_{CL_1} + \frac{en_{CL_2}}{\varepsilon_1\varepsilon_0}L_{CL_2} + \Delta\varphi \quad , \quad (11)$$

$$\phi(0) = -\Phi_B + V \quad (12)$$

In fact, during the capacitance-voltage characteristics measurement, voltage V is set as parameter. So, making the voltage V as a parameter in (11), on which the width of SCR is depends, the barrier capacity value C_{bulk} would be obtained. It is caused by changes of charged impurity amount in SCR (hereinafter – the volume barrier capacity):

$$C_{BULK} = \frac{\varepsilon_2\varepsilon_0}{w} \quad (13)$$

It should be also taken into account that in dependence (11) appears n_{CL}, and according to (8) it depends on the SCR width w. So, finally to get the equation that implicitly defines the dependence $w = w(V)$, we must substitute (8) in (12).

$$-\Phi_B + V = \frac{eN_{CV}}{2\varepsilon_2\varepsilon_0}(L_{SiOx} - w)^2 - \frac{eN_{CV}}{\varepsilon_1\varepsilon_0}(w - L_{SiOx})L_{SiOx} + \\ + \frac{eN_{CL_1}}{\varepsilon_1\varepsilon_0}L_{CL_1}\frac{1}{1+\exp(\frac{E_F - E_{CL} - eV_{CL_1}}{kT})} + \\ + \frac{eN_{CL_2}}{\varepsilon_1\varepsilon_0}L_{CL_2}\frac{1}{1+\exp(\frac{E_F - E_{CL} - eV_{CL_2}}{kT})} + \Delta\phi \quad (14)$$

$$(w - L_{SiOx})^2 - \frac{2\varepsilon_2\varepsilon_0}{eN_{CV}}(-\Phi_B + V) - \frac{2\varepsilon_2}{\varepsilon_1}(w - L_{SiOx})L_{SiOx} + \\ + \frac{2\varepsilon_2 N_{CL_1}}{\varepsilon_1 N_{CV}}L_{CL_1}\frac{1}{1+\exp(\frac{E_F - E_{CL_1} - eV_{CL_1}}{kT})} + \\ + \frac{2\varepsilon_2 N_{CL_2}}{\varepsilon_1 N_{CV}}L_{CL_2}\frac{1}{1+\exp(\frac{E_F - E_{CL_2} - eV_{CL_2}}{kT})} + \frac{2\varepsilon_2\varepsilon_0}{eN_{CV}}\Delta\phi = 0 \quad (15)$$

For the structure with n silicon clusters layers, dependence (15) will be determined as follows:

$$(w - L_{SiOx})^2 - \frac{2\varepsilon_2\varepsilon_0}{eN_{CV}}(-\Phi_B + V) - \frac{2\varepsilon_2}{\varepsilon_1}(w - L_{SiOx})L_{SiOx} + \\ + \frac{2\varepsilon_2\varepsilon_0}{eN_{CV}}\Delta\phi + \frac{2\varepsilon_2}{\varepsilon_1 N_{CV}}\sum_{m=1}^{k}\frac{N_{CL_m}L_{CL_m}}{1+\exp(\frac{E_F - E_{CL_m} - eV_{CL_m}}{kT})} = 0 \quad (16)$$

It is not possible to find an explicit dependence $w = w(V)$, in the general case analytically in elementary functions, but the algorithms of numerical solution of equation (16) are relatively easy to implement. It should be noted that the influence of additional charges (in silicon clusters) on volume barrier capacity can only be achieved at very high concentrations of silicon clusters, but it is impossible to explain NDC effect that experimentally observed, because for this effect it must be two identical values of SCR w in (16) for different applied voltages V.

The analysis of the (16), (8), (9) shows that changing of voltage applied to the contact will also leads to changing of charge in silicon clusters n_{CL}. This implies the existence of additional capacity, which is caused by the possibility of carriers capturing on the silicon clusters level, and which is differ from the main barrier capacity of the structure (hereinafter – the capacity caused by clusters). So, the mechanism of charge changing in semiconductor volume makes it possible to conclude that both capacities are connected in parallel. So, in order to calculate the capacitance-voltage characteristic of silicon diode structure with integrated Si – SiOx matrix, it is need to add to capacity C_{bulk} another capacity C_{dot}, which is caused by silicon clusters presence in dielectric and by definition of capacity will be equal to:

$$C_{CL} = e\frac{dn_{CL}}{dV} \quad (17)$$

The total capacity of contact:

$$C = C_{bulk} + C_{dot} . \quad (18)$$

Simulation results. The theoretical curve of capacitance-voltage dependence is represented in fig.2. It was obtained by the structure modeling with a thickness of 210 nm for the dielectric and with 7 silicon clusters layers for the bedding energy of quantum states equals to 0,4 eV. This energy was expelled from the certain energy level typical for the states in the grid of separate Si atoms inclusions through which hopping charge transportation is occurring through the entire structure.

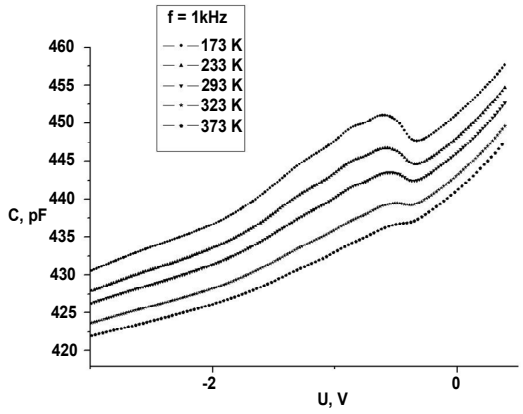

Fig.2. C-V-dependence theoretical series, calculated for different temperatures

As a result of the CVC simulation the C-V dependences have been calculated. All presented curves good qualitatively describe the appearance the area with negative differential capacitance component caused by interface states. It has been noted that this effect were essentially depended on the concentration of the interface states between nanoclusters and dielectric.

As it can be seen, NDC effect most clearly observed in the temperature range from 173 to 293 K. It is very important those effect is already clearly seen even at room temperature, and, hence, new semiconductor devices can be created based on these structures and which will work in normal environmental conditions.

Conclusion. On the basis of the calculations described in this work, it have been shown that creation of additional quantum states at the borders between silicon nanoclusters in dielectric should leads to additional electric charge accumulation, coordinate distribution of which depends essentially on external biases applied to the structure. This way, particularly, can be made influence on the part of capacitance-voltage characteristics, where area with negative differential capacitance is appearing. The paper also shows that this effect is significantly depends on temperature.

As time of quantum state refilling depends on test signal frequency, it can be predicted that capacitance-voltage characteristics of such structures can significantly changes if the frequency, at which differential capacity is measured, also have changed. The frequency dependence calculation of capacitance-voltage characteristics is a difficult self-consistent task, the solution of which requires the use of rather complicated numerical methods. However, knowing the dependence of a structure capacity from external bias for different test signal frequencies and temperatures, concentration and energy position of the quantum states can be determined.

1. Алёшкин В., Бекин Н., Буянова Б. Определение плотности квантовых состояний в квантовых ямах и ансамблях квантовых точек вольт-фарадным методом. // Физика и техника полупроводников, 1999. – Т. 33. 2. Богомолов В., Голубев В., Феоктистов Н., Получение регулярных трехмерных решеток кремниевых кластеров субмикронных размеров в матрице SiO_2. // ЖТФ, 1998. – Т. 24. 3. Bonafos C., Carrada M., Cherkashin N., Manipulation of two-dimensional arrays of Si nanocrystals embedded in thin SiO_2 layers by low energy ion implantation. // J. of Appl. Phys., 2004. – Vol. 95. 4. Chiquito A., Pusep Y., Mergulhao S. Capacitance-voltage profile in a structure with negative differential capacitance caused by the presense of InAS self-assembled quantum dots. // Phys. Rev., 2000. – Vol. 61. 5. Crupi I., Corso D., Ammendola G. Peculiar aspects of nanocrystal memory cells: data and extrapolations. // IEEE transaction on nanotechnology, 2003. – Vol.2. 6. Данько В., Индутный И., Лысенко В. Кинетика фазово-структурных преобразований в тонких пленках SiO_x в процессе быстрого термического отжига. // ФТП, 2005. – Т. 39. 7. Gudovskikh A., Kleider J. Characterization of a-Si:H/c-Si interface by admittance spectroscopy. // ФТП, 2005. – Т. 39. 8. Hu G., O'Connel R., He Y. Electronic conductivity of hydrogenated sislicon films. // J. of Appl. Phys., 1995. – Vol. 78. 9. Ilchenko V., Buianin A., Panarin K. Observation of the negative differential capacitance in Shottky diodes with InAs quantum dots near room temperature. // Appl. Phys. Lett., 2007. – Vol. 90. 10. Ільченко В., Панарін К., Буянін О. Моделювання частотних залежностей вольт-фарадних характеристик для контакту метал-напівпровідник з шаром квантових точок. // J. of Phys. Stud., 2008. – Т. 12. 11. Качурин Г., Володин В. Формирование кремниевых нанокристаллов в слоях SiO_2 при имплантации ионов Si с промежуточными отжигами. // Физ. и тех. полупроводников, 2005. – Т. 39. 12. Lin S., Ilchenko V., Buianin A. Frequency dependence of negative differential capacitance in Shottky diodes with InAs quantum dots. // Appl. Phys. Lett., 2008. – Vol. 93. 13. Нефедов Д., Яфаров Р. Влияние температуры на формирование кремниевых нанокристаллитов на некристаллических подложках в плазме СВЧ газового разряда. // ЖТФ, 2007. – Т. 34. 14. Oda S. Carge storage in silicon nanocrystals and device application. // Mater. Sci. Eng., 2003. – Vol. 101

Submitted on 12.03.2010

UDC 535.33

Ya. Horishny, stud., O. Kolesnyk, adv. eng.,
A. Knurenko, post grad. stud.

RESOLUTION IMPROVEMENT OF TIME-OF-FLIGHT LASER-IONIZATION MASS-SPECTROMETER

Сучасна мас-спектрометрія – один із найбільш точних та чутливих методів дослідження складу речовин. Лазерно-іонізаційна мас-спектрометрія (ЛІМС) не є новим інструментом прямого елементного аналізу. Але цей метод має деякі переваги в порівнянні з іншими мас-спектрометричними методами аналізу зразків. Зокрема, ЛІМС дозволяє аналізувати будь-які класи твердих речовин (провідники, напівпровідники, діелектрики, порошки) та складні комплексні зразки (біологічні, геологічні об'єкти, ґрунти). Це "чистий метод" у порівнянні з іншими іонізаційними методами. Використання ЛІМС дозволяє здійснювати пошаровий аналіз речовин. Ця робота присвячується опису покращення роздільної здатності часопролітного лазерно-іонізаційного мас-спектрометра. Результатом проведеної модернізації мас-спектрометра було істотне покращення роздільної здатності.

Ключові слова: мас-спектрометрія, роздільна здатність, лазерне джерело іонів.

Modern mass-spectrometry is a one of the most thin and sensitive methods of the substance analysis. Laser-ionization mass-spectrometry (LIMS) is not a new tool in direct-sampling elemental analysis. But this method has a few advantages in comparison with other mass-spectrometry methods of the analysis of samples. For example, LIMS allows to analyze any class of solids (conductors, semiconductors, dielectrics, powders) and complex samples (biological, geological objects and soils). It is the "clean" method in comparison with other methods of ionization. Use of LIMS allows analyze samples layer-by-layer. This work is devoted to description of resolution improvement time-of-flight laser-ionization mass-spectrometer. As a result of a fulfilled modernization of the mass-spectrometer the resolution significantly was improved.

Key words: mass spectrometry, resolution, laser ion source.

Introduction. Research in nuclear physics, nuclear engineering, nuclear energy and microelectronics, development of technological processes of particularly pure substances needed in various areas of science and industry, are impossible without application of universal, highly sensitive methods of substances analysis.

Characteristics of materials being developed and used nowadays [1] depend on the content of these impurities at the level of less than 10^{-4} - 10^{-6}%, therefore the basic requirements for modern methods of substances analysis is high relative and absolute sensitivity or low limits of detecting the presence of elements, the possibility of registering a wide range of elements as well as obtaining information about the chemical composition of substances in a relatively simple form, regardless of their physicochemical properties.

Modern mass spectrometry is one of the most subtle and sensitive methods of substance analysis. Recent decades are characterized by enormous advances in ion optics, electronics, vacuum technology, and application of new and highly sensitive devices for registering ionic currents. All of that determined the present state of mass-spectrometric method and its advanced position among a number of physical methods of investigation and analysis of substances [1].

The laser Time-of-Flight (T-o-F) mass spectrometry is one of the direct methods of substances analysis. This method has several advantages in comparison with others [2]. These include: the possibility of analysing any class of solids (conductors, semiconductors, dielectrics, powders), no need for any consumables, possibility of local and layer-by-layer analysis, the possibility of elemental analysis of complex samples such as biological and geological objects. The disadvantage of this method is the presence in the mass spectrum of ions with a multiple ionization. Repulsion of the electric charges of a one sign may distort the resulting spectrum.

The mass spectrometer that we work with, was built on an out-of-date technological base, thus its components are constantly subject to modernization due to lack of correspondence to modern requirements and standards. The configuration of the mass spectrometer included a signal preamplifier whose frequency characteristics have a considerable effect on the resolution of the device.

The aim of this work was just to replace the preamplifier. Under improvement of the frequency characteristics, the mass spectrometer resolution is expected to increase,

which implies the possibility of more accurate registration of the elemental composition of samples being investigated with the mass spectrometer.

The main parameters of the mass spectrometer system is its resolution and aperture [1]. The mass spectrometer resolution is determined by its ability to separate ions with different mass. This value is usually expressed in relative units: $R_m = \frac{m}{\triangle m}$, where $\triangle m = m_1 - m_2$ is the minimum difference between the masses of ions recorded separately; $m = \frac{1}{2} \times (m_1 + m_2)$ is the average mass of ions. Generally, the aperture is defined as the ratio of the number of ions that reached the detecting device to the total number of ions formed in the ion source. That is, actually, the mass spectrometer system aperture is characterized by the transmission coefficient of the ion beam through the analytic part of the mass spectrometer.

The simplest laser mass spectrometer is a linear Time-of-Flight mass spectrometer where the ions move in a straight line from the ion source to the detector (Fig.1). The resolution of this device was low ($R_m \approx 6$). In this scheme it can not be substantially increased because the laser ion source has a sufficiently large spread in ion energies (about 1000 eV). When samples of different thickness are exposed to laser irradiation, for a focal spot of small diameter (about 1 micron) the energy dispersion of the ions formed varies depending on the thickness of the irradiated sample. Thus, when thin films [1] whose thickness is less than $0,2$ microns are processed, the energy spread is less than 15 eV, for those having a thickness of $0,2-0,5$ microns – less than 50 eV, and for the thick monolithic samples it is equal to 1000 eV.

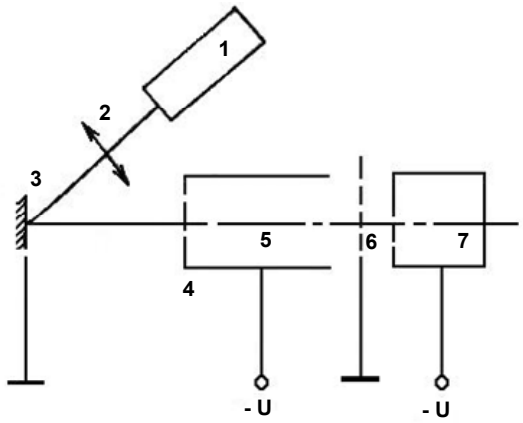

Fig.1. Schematic picture of the linear Time-of-Flight mass spectrometer with the laser ion source: 1 – laser with modulated Q factor; 2 – laser focusing system; 3 – investigated sample; 4 – accelerating electrode; 5 – drift space; 6 – decelerating electrode; 7 – electron multiplier

Experimental setup. The mass spectrometer is structurally assembled in a metal chamber (fig.2). The camera is pumped by means of a zeolite adsorption pump to the preliminary dilution $10^{-2}-10^{-3}$mmHg and a magnetodischarging pump (NORD-100) to achieve a working vacuum $(3-5)\times10^{-6}$mmHg. The value of working pressure is stipulated by the free path of ions length, which must exceed the drift distance for the device $(2m)$.

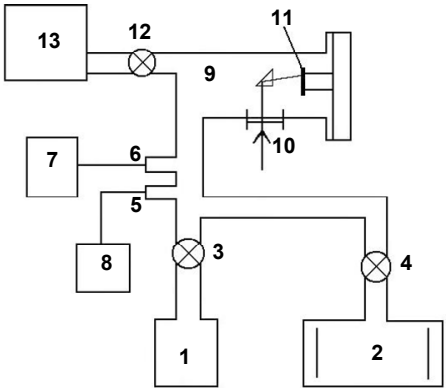

Fig.2. Schematic picture of the vacuum system for a laser-ionization mass spectrometer: 1 – zeolite pump; 2 – magnetodischarging pump; 3, 4 – vacuum valves; 5 – thermocouple sensor; 6 – ionization sensor; 7 – thermocouple vacuum; 8 – ionization vacuum gauge; 9 – working camera; 10 – flange of laser beam input; 11 – sample; 12 – slanting crane; 13 – mass analyzer

In the Figure 3, a schematic picture of the laser-ionization Time-of-Flight mass spectrometer is presented, which allows obtaining information about the local elemental structure of any material. A neodymium laser is used as a source of plasma(1). The laser operates on a modulated Q-factor of the radiation pulse length 8 ns, which provides the power density at the target of $q = 10^9 - 10^{10} \frac{Vt}{cm^2}$. After passing the optical focusing system (2) the laser beam falls on the target (3). A plasma clot formed in the sub-surface target area, enters the monochromator (4), at the output of which the packets of ions of different masses but with the same energy are received. After passing the drift tube (5) the ion packets arrive at the electron multipliers (6) of the recording system, which enhance the signal. At the outlet of the multiplier an amplifier (7) is connected, and then a digital oscilloscope connected to a computer (8) records the spectrum into the memory. The beginning of the digital oscilloscope scan is synchronized by the emergence of laser radiation through the impact on a special photocell.

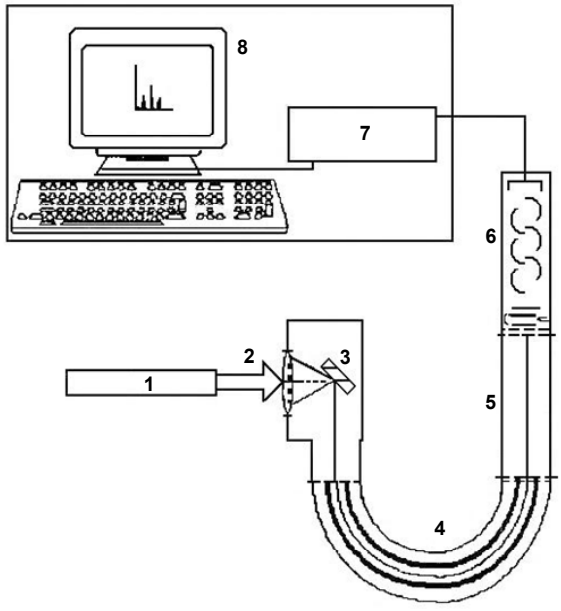

Fig. 3. Schematical picture of the Time-of-Flight mass spectrometer: 1 – laser; 2 – lens; 3 – target; 4 – ion beam trajectory in the monochromator; 5 – ion drift tube; 6 – electron multiplier; 7 – amplifier; 8 – registration system, which consists of digital oscilloscope and computer

Results and Discussion. The main object of the mass-spectrometer modernization was a resolution improvement. To improve the resolution the previous signal amplifier was changed. The transistor amplifier was taken instead of the old tube amplifier (fig.4). After changing the amplifier, in the result of the experimental tests spectrums with significant resolution improvement were obtained. The new amplifier allows to get much more precise information about elemental structure of solid samples.

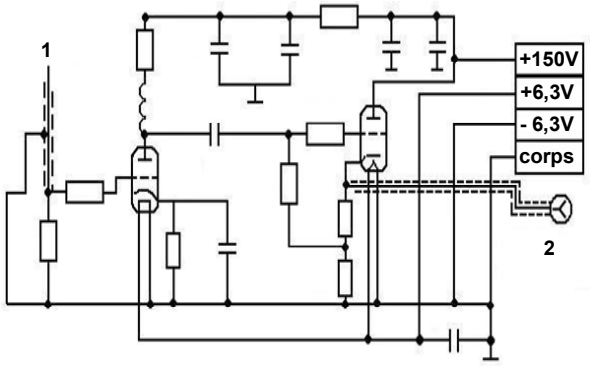

Fig. 4. Schematic electrical circuit of the tube amplifier: 1– multiplier output; 2 – output to the oscilloscope

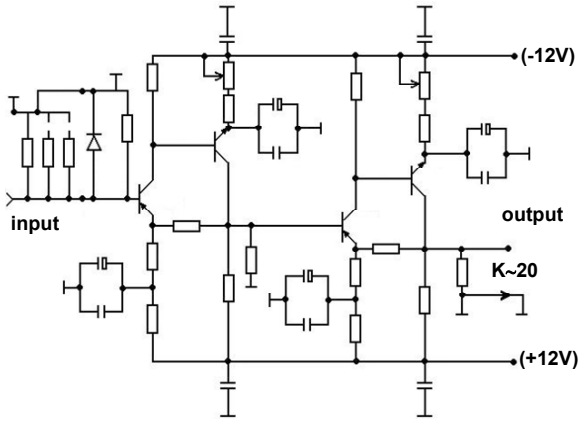

Fig. 5. Schematic electrical circuit of the transistor amplifier

The presented preamplifier (fig.5) was mounted into the mass spectrometer plant. After that the experimental Cu^+ spectrums measurements were carried out.

The experimental Cu^+ spectrums measurement (fig. 3) indicated the significant increase of mass-spectrometer resolution. For the comparison, the fig. 4 shows the Cu^+ spectrum obtained with the old tube amplifier. The calculated value of the mass-spectrometer resolution is $R_{m2} \sim 1071$.

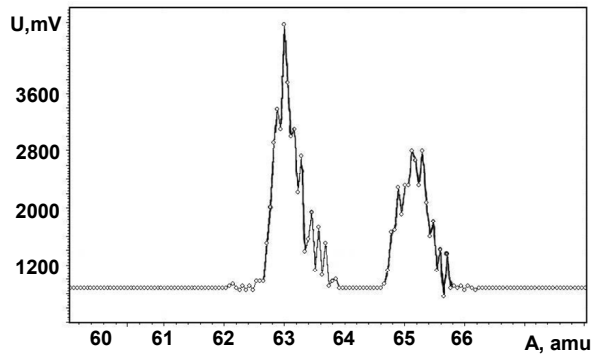

Fig. 6. The Cu^+ spectrum obtained with the transistor amplifier

For comparison, the fig.7 shows the Cu^+ spectrum obtained with the old tube amplifier. The calculated value of the mass-spectrometer resolution is $R_{m1} \sim 57$.

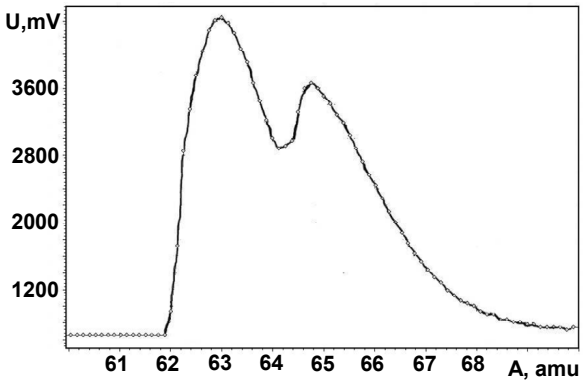

Fig. 7. The Cu^+ spectrum obtained with the tube amplifier

For the tube preamplifier there was calculated the value $R_{m1} \sim 57$. Resolution was calculated through the peak width at the level of 20% of the maximum height of the mass spectrometric peak.

The new spectrum illustrates that the masses of Cu_{63} and Cu_{65} are well separated. At the 64^{th} mass position a distinct failure is observed.

The new spectrum provided the possibility to see the spectrum growth and decline and observe different duration of the rising and descending edges. It can be explained the following way: emergence of plasma during evaporation happens very quickly, within the time of the laser pulse, and decline (dragged descending edge) is associated with scattering of plasma, which lasts much longer than emergence of a plasma clot [5]. In addition, we can see pulsations of received ions associated with fluctuations of the plasma clot.

These pulsations complicate decoding the spectrum. For large masses $(A > 150)$ the plasma frequency is commensurate with the frequency of receiving different masses, which does not let separate the isotopes of large masses accurately, thus one must change the frequency of plasma oscillations or arrival time of ions of large masses. For this purpose it is necessary to conduct additional research.

The resolution of T-o-F mass-spectrometer was improved by constructing a new transistor amplifier. Comparing the spectra obtained before and after changing the amplifier an estimation of the improved resolution R_m was made. The old tube amplifier had the resolution $R_{m1} \sim 57$, while after changing the amplifier the new value became $R_{m2} \sim 1071$. Therefore, the improved resolution of the mass-spectrometer was almost 19 times higher.

Replacement of the amplifier allows observing the movement of ion flows arising from fluctuations of a plasma clot. This raises the need for further work on studying of laser plasma in order to overcome this problem.

Conclusions. The resolution of T-o-F mass-spectrometer was improved by constructing a new transistor amplifier. Comparing the spectra obtained before and after changing the amplifier an estimation of the improved resolution R_m was made. The old tube amplifier had the resolution $R_{m1} \sim 57$. After changing the amplifier the new value became $R_{m2} \sim 1071$. Therefore, the improved resolution of the mass-spectrometer was almost 19 times higher.

After changing the amplifier, there appeared the possibility to observe the physics of the plasma generation and scattering processes in more details, since the better fre-

quency characteristics of the new amplifier on the panoramic spectra allow seeing clear ions pulsations which appear through the plasma clot oscillation and fronts of the increasing and decreasing of the mass-spectrometer peak.

1. Bykovsky Yu.A., Nevolin V.N. Laser mass-spectrometry. – M.: Energoatompublish., 1985. – 128 p. 2. Sysoev Alexander A. and Sysoev Alexey A.. Can laser-ionisation time-of-flight mass spectrometry be a promising alternative to laser ablation / inductively coupled plasma mass spectrometry and glow discharge mass spectrometry for the elemental analysis of solids? // Eur. J. Mass Spectrometry. – 2002, № 8. – P.213–232.

Submitted 15.01.10

UDC 537.622.4

V. Koronovskyy, Ph.D.

ENHANCEMENT OF THE ELECTROMAGNETO-OPTICAL EFFECT IN LEAD ZIRCONATE TITANATE/YTTRIUM IRON GARNET COMPOSITE STRUCTURE ON TRANSVERSE MAGNETIC FIELD

The electromagneto-optical effect as a magneto-electric response for lead zirconate titanate/yttrium iron garnet structure by applying an external longitudinal electric field and transverse magnetic field were registered by using optical polarimetry method. The electromagneto-optical characterization was carried out as a function of the variable electric field and static magnetic field. The investigated effect for such structure went up by a factor approximately of five than for separate yttrium iron garnet in such geometry of experiment.

Keywords: electromagneto-optical effect, electric field, magnetic field, optical polarimetry method.

Електромагнітооптичний ефект як магнітоелектричний відгук для структури, яка складається з цирконату титанату свинцю/залізоіттрієвого гранату, що розміщувалась в зовнішніх повздовжньому електричному та поперечному магнітному полях був зареєстрований з використанням методу оптичної поляриметрії. Електромагнітооптичний параметр вимірювався як функція змінного електричного поля та статичного магнітного поля. Досліджуваний ефект для вказаної структури зріс приблизно в п'ять разів у порівнянні з величиною ефекту для залізоіттрієвого гранату в подібній геометрії експерименту.

Ключові слова: електромагнітооптичний ефект, електричне поле, магнітне поле, оптична поляриметрія.

The magneto-electric (ME) effect (MEE) consists in induction of a magnetization by an electric field or polarization by a magnetic field and expresses the link between magnetic and electric properties in materials. Landau and Lifshitz showed that a linear MEE can occur in magnetically ordered crystals and later Dzyaloshinskii predicted the existence of the MEE in Cr_2O_3 crystals on the basis of theoretical analysis [3]. Astrov showed experimentally ME effect by measuring the electric field-induced magnetization and Rado measured the magnetic field-induced polarization [1; 10]. In the latter decades, the MEE (first ordered and higher ordered) has been found in numerous materials. An enormous interest in ME phenomena is observed because some magnetoelectrics and composite structures exhibit MEE which exceeds previous effects by many orders of magnitude [4].

The existence of a connection between the magnetic and electric parameters of a substance demands a study of all the possible mechanisms of influence an electric field has on the magnetic characteristics of such substances. The recent interest in ME materials is stimulated by their significant technological potential. A prominent example is the control of the ferromagnetic state by an electric field. This phenomenon could yield entirely new device concepts, such as electric field-controlled magnetic data storage. In a broader vision, ME effects include not only the coupling between the electric and magnetic polarizations, but also related phenomena such as an electrically-controlled exchange bias, and magnetocrystalline anisotropy, and the effect of ferroelectricity on spin transport. Among materials for such studying in which MEE induced by the electric or by the magnetic field were observed experimentally there are yttrium iron garnets (YIG) and composite structures based on YIG. Mercier measured this effect with the ac method and analysed the relation between the signal and the magnetization process on the electric field dependence of the cubic magnetic anisotropy constant. They did not observed the first order effect, probably because they did not apply E field during cooling. Recently, the first order MEE was observed below 125 K, in a crystal synthesized by the floating zone melting method, when the E field is applied during cooling. This is suggestion, that there is a phase transition at around 125 K. The relation between these two MEE with different order, however, has not been examined. However, this material showed the ME interaction of small value, insufficient for practical application.

In Ref. 6 the authors proposed a new direction in the development of ME materials – creation of composite structures i.e., magnetostrictive-piezoelectric layered structures. The idea of synthesizing a composites displaying a ME effect was first formulated by Tellegen, that is, more than a decade before the first observation of intrinsic ME behaviour in a single-phase compound [4]. A suspension of macroscopic particles that carry both electric and magnetic dipole moments was suggested, an idea that, however, proved impossible to realize because of a matter of principle. Later, have been grown up the first artificial ME materials by combining ferroelectric piezoelectric $BaTiO_3$ and ferromagnetic piezomagnetic $CoFe_2O_4$ in an eutectic composite by unidirectional solidification [4]. The advantages of composite structures – the physical properties of a composite are determined by the properties of the constituents as well as by the interaction between them. That helps to accomplish higher value of MEE compared to single phase materials. In some early experiments on composite structures the ME response exceeds the largest values observed on single-phase compounds by more than an order of magnitude. These results can be interesting for applied possibilities. Apparently the composite MEE is a mighty addition to the class of ME coupling phenomena. Many new parameters which can be tuned in order to optimize the ME response (such as the stoichiometry and microstructure of the composite) are at hand [4]. Composites of interest in the past were bulk samples of $NiFe_2O_4$ (NFO) or $CoFe_2O_4$ (CFO) with $BaTiO_3$ (BTO) and are generally synthesized by sintering the ferrite and $BaTiO_3$ powders [5].

Other big group of interesting composites is the multilayered nanostrustures – layered compositions (a thin films, a foil, a covering). These multicomponent structures consisting from alternating nanolayers from various materials, with thickness of layers less than 100 nanometers and quantity of layers to several thousand. As components of layers, in such systems, the wide range of materials can be used: metals and alloys, semi-conductor materials, and others. Because of features of a structure: an ultra-small thickness of the layers, possibilities of dense interface of

layers from various materials, a considerable quantity of layers, these nano-laminates are a unique class of materials which combine qualities of layered systems and specific properties of nano-objects. Because of it, many types of multilayered nano-structures show unique ME, mechanical, heat-physical, etc. properties and they represent interest for various practical application.

Thus, two basic mechanisms for the MEE have been established: (1) in single-phase ME materials electric field displaces ions from equilibrium positions which changes the magnetostatic and exchange interactions affecting the magnetization; (2) in ME composites, piezoelectric strain in the ferroelectric constituent of the multiferroic heterostructure induces changes in the magnetic properties of the ferromagnetic constituent due to magnetostriction.

In this paper we report the results of using optical methods for experimental investigations of ME properties in the mechanically connected structure with combining magnetostrictive and piezoelectric compounds. Apparently the investigated two-phase structure is a essential addition to the class of ME materials and author consider magneto-electric effect in an optical range as a new degree of freedom in designing ME devices.

The optical polarimetry method is one of the methods for investigation of the magneto-electric effects. This method deals with the registration of the changes of light polarization plane Faraday rotation under action of external electric field applied to the sample. This method allows to register and to visualise the optical phenomena in the materials, induced by electric and (or) magnetic fields. The appearance of such changes (under action of E-field) has been termed the electromagneto-optical effect (EMOE) [9].

Ours experimental setup consists of a high-sensitive laser polarimeter, described in [8]. The heart of the method is the registration of the electric-field-induced changes of the magneto-optical rotation (α_{EMO}) in investigated structure. The investigated structure was fabricated with stuck together YIG film (magnetostriction phase) and lead zirconate titanate (PZT) (piezoelectric phase). The theory predicts giant magneto-electric interactions in ferrite-PZT bilayers at frequencies corresponding to electromechanical resonance. A thin layer of an epoxy was used to bond magnetic phase to piezoelectric (a thickness of epoxy is considered very small). YIG film was deposited on the gallium gadolinium garnet substrates with a thickness of about $600\,\mu m$. Thickness of the film was $4\,\mu m$ range. The investigated sample was placed between the optically transparent electrodes which were used to apply the external electric field. A variable voltage, with the frequency $\omega = 1000\,Hz$ and static magnetic field could be applied to the composite structure. We proposed the model where electric field is applied to all structure, and not just for piezoelectric phase, as in similar experiments. It is an important moment because the EMOE was registered by us earlier in YIG films [7; 8], and in this case there is a searching of "amplifier" of EMOE in YIG films. A He-Ne laser with $\lambda = 0,63\,\mu m$ was used in our experiments. The measurements have been fulfilled on small areas of sample (a He-Ne laser probing $\varnothing < 2\,mm$). Experiments were carried out at room temperature in geometry $H \perp k$ (in transverse magnetic field) and $E \parallel k$ (in longitudinal electric field), where **H** – static magnetic field, **E** – variable electric field and k is a light wave vector.

Composite material on the basis of YIG film and lead zirconate titanate is a perspective way for decision of the serious problem: though YIG (single crystals and films) is one of the ME materials, nevertheless the small magnitude of the induced magnetization or polarization in YIG (for room temperature) is not sufficient for their wide technical applications. The amplitude of ME interaction for the composite is higher than for the separate compounds. Such structure possess all properties of piezoelectric and ferrite materials and, besides, ME properties [2].

Typical magnetic-field dependence of EMOE (the EMOE parametre α_{EMO} as a function of the static magnetic field when $H \perp k$) for investigated structure (YIG film/PZT plate) is presented in Fig. 1. The EMO effect is registered on the basic frequency of external electric field.

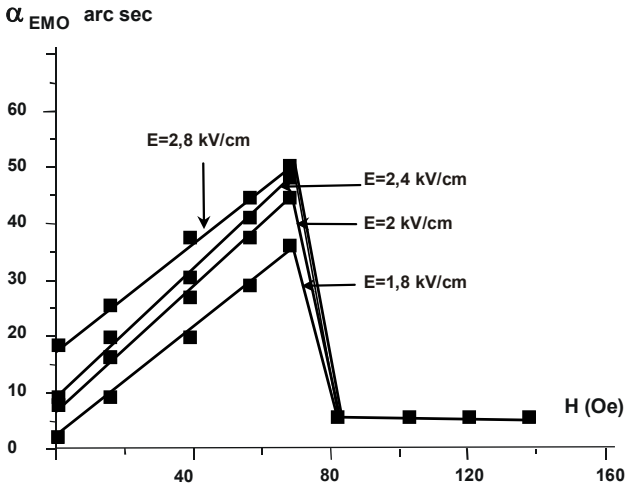

Fig. 1. The H-field dependence of the EMOE for composite structure measured in the transverse magnetic field

In Fig.2 typical E-field dependences of α_{EMO} (the EMOE as a function of the variable electric field when $E \parallel k$) are shown for fixed values of magnetic field: H_1=0 Oe, H_2=40 Oe, H_3=75 Oe and H_4=90 Oe. A linear dependence of the α_{EMO} shift on the electric field is evident from Fig. 2.

Comparing the presented dependences in Fig. 1 and Fig. 2 with results of the researches of EMO effect received earlier by us for YIG films in similar geometry of experiment, when $H \perp k$ (in transverse magnetic field) it is necessary to note basic differences in results:

1) The EMOE registered on the basic frequency of electric field.

2) The EMO effect in this investigated two-phase structure is registered by us also in absence of an external static magnetic field.

3) The EMO effect in maximum for YIG/ PZT structure is a factor approximately of five higher than for YIG films that registered in transverse magnetic field earlier [8].

The fact of registration of the EMOE for investigated structure at H=0 is an acknowledgement for our assumption about enhance properties of the PZT phase of the composite ME structure for EMO signal. It becomes clear from comparison the H-field or E-field dependences of the EMOE for YIG films and YIG/PZT structure. The EMOE was not registered by us earlier at H=0 for YIG at probing multidomain areas of the films [7;8].

In Fig.3 typical E-field dependences of α_{EMO} (EMOE as a function of the electric field when $E \parallel k$) are shown for fixed values of static magnetic field (H_1=0 Oe, H_2=80 Oe and H_3=110 Oe) in geometry of experiments: $\angle kH \approx 100^o$. It is possible to see from Fig. 3 that

EMOE signal value is depends on orientation of external magnetic field H concerning the direction of a normal vector n to the sample ($n \| k$). I.e. anisotropic properties of EMOE are shown.

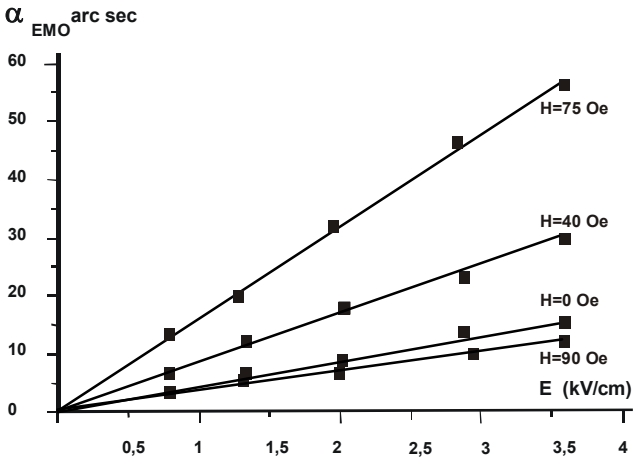

Fig. 2. The electric-field dependence of α_{EMO} measured in the transverse magnetic field

If to analyse presented on Figures 1-3 experimental results for PZT/YIG composite structure, we can to note following. In the composite structure (that already cannot be considered as a homogeneous material) consisting from mechanically stuck together piezoelectric and magnetostriction materials (PZT plate/YIG film), occurrence of the EMOE is connected with EMOE in YIG film and with result of mechanical interaction of ferrite and piezoelectric subsystems (when all investigated sample was placed between the electrodes, it is important). Displaying of the EMOE in epitaxial YIG films is caused by change in them magnetic anisotropy under the influence of electric field – the external electric field gives rise to small changes of the domain-wall positions (or their widths) in the YIG films [8]. In an applied electric field occurs deformation of piezoelectric phase because of piezoelectric effect. The deformation is transferred to the ferrite layer which is mechanically connected with piezoelectric phase and result in a changed magnetic condition (magnetic field) of ferrite because of piezomagnetic effect. Our technique is registering the "effective" EMOE parameter α_{EMO} as a total result of these two effects: the EMOE in the YIG film as result of changing of the magnetic anisotropy and the EMOE due to mechanical conjugation of YIG and PZT components. Thus, we experimentally shown that PZT plate/YIG film structure possess the effective electromagneto-optical effect which is as "product" of two effects (or two components of total effect): EMOE in single magnetic phase (YIG film) and EMOE due to magnetostriction/piezoeffect.

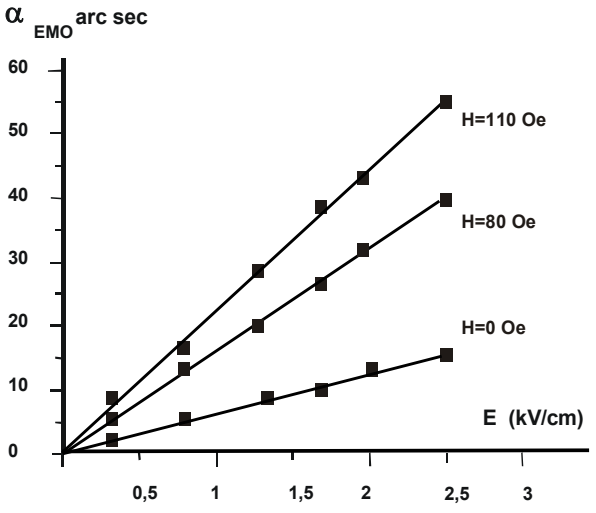

Fig. 3. The electric-field dependence of α_{EMO} measured in the transverse geometry when $\angle kH \approx 100^{o}$

Thus, the α_{EMO} parameter as a ME response for YIG film by applying an external electrical field to both PZT and YIG phases was registered for PZT/YIG composite structure in transverse geometry of experiment (in transverse magnetic field). Registered by us EMOE is first ordered in the electric field. The piezoelectric phase (PZT plate) in given structure carries out the enhance function for EMOE already induced by electric field in a YIG film. The EMOE value (α_{EMO}) for PZT plate/YIG film structure is a factor approximately of five higher than for YIG films (second ordered in the electric field EMOE) that registered by us earlier in transverse magnetic field and at room temperature. The coupling between ferrimagnetic (or ferromagnetic) and piezoelectric phases (and corresponding parameters) in thin-film composites (or heterostructures) is an exciting new frontier in nano-scale science. The underlying physical phenomenon controlling properties of such materials is the MEE.

1.Astrov D.N. The magnetoelectric effect in antiferromagnetics // Sov. Phys. – JETP. – 1960. – 11. – P. 708-709. 2. Bichurin M.I., Petrov V.M., Petrov R.V. and all. Magnetoelectric Sensor of Magnetic Field // Ferroelectrics. – 2002. – 280. – P. 96-101. 3. Dzyaloshinskii I.E. On the magnetoelectrical effects in antiferromagnets // Sov. Phys. – JETP. – 1959. – 10. – P. 33-35. 4. Fiebig M. Revival of the magnetoelectric effect // J. Phys. D: Appl. Phys. – 2005. – 3. – P. 8123-152. 5. J. Van den Boomgaard, Terrell D.R., Born R. A. An In Situ Grown Eutectic Magnetoelectric Composite Materials: Part I // J. Mater. Sci. – 1974. – 9. – P. 1124-1129. 6. Harshe G., Dougherty J.P., Newnham R.E. Theoretical modeling of 3–0/0–3 magnetoelectric composites // Int. J. Appl. Electromag. Mater. – 1993. – 4. – P. 92-98. 7. Kovalenko V.F., Koronovskyy V.E. The features of electromagneto-optical effect in ferrite-garnets films // Ukr Fiz Z. – 2002. – 47, 10. – P. 855-900. 8. Koronovskyy V. E., Ryabchenko S. M., and Kovalenko V. F. Electromagneto-optical effects on local areas of a ferrite-garnet film // Phys. Rev. B. – 2005. – 71. – P. 172402-172406. 9. Krichevtsov B.B., Pisarev R.V., Selitskij A.G. The electromagneto-optical effect in yttrium iron garnets $Y_3Fe_5O_{12}$ // JETP Lett. – 1985. – 41. – P. 317-319. 10. Rado G.T., Folen V. J. Anisotropy of the magnetoelectric effect in Cr_2O_3 // Phys. Rev. Lett. – 1961. – 6. – P. 141-147.

Submitted on 15.02.10

УДК 004.9

M. Morozova, assistant

DISTANCE LEARNING COURSES FOR INFORMATION AND MEASURING ENGINEERING

Розкрито поняття "Дистанційної освіти" як форми навчання, при якій студент та викладач є фізично віддаленими, а їх спілкування відбувається за допомогою інформаційно-комунікаційних технологій. Розглянуто дистанційні курси "Вимірювальні перетворювачі", "Методи та засоби вимірювань", розроблені в Національному технічному університеті України, та віртуальні лабораторії, створені за допомогою середовища LabVIEW компанії National Instruments.

Ключові слова: навчальний дистанційний курс, дистанційна освіта, вимірювальний перетворювач, сенсор, віртуальний інструмент.

The term "Distance learning" as a form of education process where, in fact, the student and the teacher are geographically separated via information-communication technology, is shown. The distance learning courses "Measuring converters", "Measuring methods and facilities", which were developed in the National Technical University of Ukraine, as well as virtual laboratories created with National Instruments' software LabVIEW, are considered in this article.

Keywords: distance learning course, distance education, measuring converter, sensor, virtual instrument.

Introduction. Engineering education consists of lectures, laboratory exercises, practical trainings, earning skills among with fundamental knowledge. All these aspects make engineering study more complex than studying economy, law or foreign languages, which in turn decreases interrest for these studying areas.

The creation of a new virtual technology in education using computer systems and methods of artificial intelligence is the powerful mean of modernization of engineering education process to the adequate requirements of today.

Distance learning has been recognized as one of the most successful and effective present-day forms of the countinuous professional education worldwide. It consists in receiving the educational services by learners through communication channels (E-mail, telecommunication lines, Internet).

A learner does not interrupt his/her practical activities, however, interacts with a teacher (mentor) on a regular basis via the selected communication channels: a learner is provided with literature, comments, recommendations, answers to the questions, responses to tests and laboratory works.

Types of distance education courses. Types fall into six major categories:

- Correspondence conducted through regular mail;
- Internet conducted either synchronously or asynchronously;
- Telecourse/Broadcast, in which content is delivered via radio or television;
- CD-ROM, in which the student interacts with computer content stored on a CD-ROM;
- PocketPC/Mobile Learning where the student accesses course content stored on a mobile device or through a wireless server;
- Integrated distance learning, the integration of live, in-group instruction or interaction with a distance learning curriculum.

Distance learning has traversed four to five "generations" of technology in its history [5]. These are print, audio/video broadcasting or teleconferencing, computer aided instruction, e-learning/online-learning, computer broadcasting/ webcasting etc. Yet the radio remains a very viable form, especially in the developing nations, because of its reach. The increasing popularity of mp3 players, PDAs and Smart Phone has provided an additional medium for the distribution of distance education (DE) content, and some professors now allow students to listen or even watch video of a course as a Podcast.

Distance learning in the National Technical University of Ukraine. From a great number of Ukrainian institutes of higher education one can mark out five nation-wide foundations, which occupy themselves with searches for unity of theoretical and practical aspects of DE. Ukrainian Distance Education Center (UDEC) of the National Technical University "KPI" (http://udec.ntu-kpi.kiev.ua) is among them.

UDEC was created on the 7th of June 2000 by the special order of Ministry of education and science of Ukraine as a structural subdivision of the National Technical University of Ukraine. It contains the following departments:

- department of informational technologies and technical provision;
- department of distance learning technologies;
- department of training-methodological provision;
- department of normative-legal provision;
- department of marketing and international projects.

UDEC provides:

- development of the concept of DE in Ukraine;
- working out of the juridical and legal basis for DE in Ukraine;
- development of the methodological basis for DE in Ukraine;
- development of distance courses on the basis of modern computer technologies;
- coordination of Ukrainian educational establishments in the field of DE;
- training, retraining and certification of specialists using modern computer systems of DE.

UDEC is equipped with a client-server computer system based on the double-processor servers with the operation Linux systems. It supports the modern international client-server systems of distace training on the basis of Lotus Notes Domino and Learning Space or on the basis Moodle software. Moodle can be installed on any computer that can run PHP, and can support an SQL type database (for example MySQL). It can be run on Windows and Mac operating systems and many flavors of linux (for example Red Hat or Debian GNU).

UDEC carries out DE using the technical potential of URAN (Ukrainian Research and Academic Network) and provides technical Internet and Intranet channels of access to Ukrainian educational and research organizations.

About distance learning course "Measuring converters". Presently, a measuring technique allows us to control about of two hundred different physical quantities. The most of them can be transformed in an electrical signal, which is comfortable for the exact measuring, transmission, amplification and mathematical treatment. Such kinds of measuring are performed by using measuring converters (sensors) developed on a basis of certain physical principle (piezoelectric, inductive, magnetoelastic, capacitive, etc.).

The distance learning course "Measuring converters" is executed within the framework of the Government Research Program "Information and communication technologies in education and science during 2006-2010 years" (Project

"Creation attesting courses' bank for distance education" and Pilot Project "Distance learning for bachelors, direction "Metrology and information measuring technologies").

The educational course "Measuring converters" was developed for study of construction principles, basic descriptions and application of main connection circuits with sensors of non-electrical quantities.

The following tasks were incorporated in the course:

- study of basic concepts and characteristics in area of measuring converters;
- study of basic methods and facilities for output intelligence signals;
- mastering the physical phenomena which are used for construction of measuring converters;
- obtaining skills of work with a measuring technique;
- getting experience on developing measuring converters.

Target audience consists of students of specialities "Metrology and measuring technique" and "Information and measuring systems", students of the technical specialities, related to measurings, specialists in area of measuring converters, specialists of other directions, related to development and use of facilities for measuring technique, intellectual measuring facilities, monitoring systems, technic diagnostics.

Program of discipline "Measuring converters" is related to the preliminary study of following disciplines: "Higher mathematics", "Physics", "Metrology", "General electrical engineering", "Probability and Statistics", "Theory of electrical signals and circuits", "Materials".

The course "Measuring converters" includes lectures, laboratory and practical trainings, calculation-graphic setup and results in semester paper (see fig. 1). Theoretical material of lectures is logically separated on three parts: introduction (consists of 7 lectures), basic level (consists of 13 lectures) and advanced level (consists of 10 lectures). It provides knowledge from primary to advanced problems on the discipline "Measuring converters". Advanced level of the course is counted on independent work of students with material.

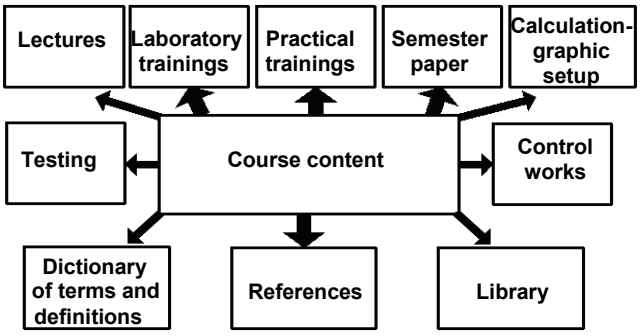

Fig. 1. Course content

Lectures are organized in ten interlinked modules:

Module 1. Introduction. Course content. Basic concepts and determinations.

Module 2. Basic descriptions of measuring converters.

Module 3. Methods and facilities for forming of output intelligence signals.

Module 4. Resistive measuring converters.

Module 5. Capacitive measuring converters. Transducers of charge.

Module 6. Thermocouples. Photo-electrical sensors. Electrochemical sensors.

Module 7. Electromagnetical measuring converters.

Module 8. Technology fundamentals.

Module 9. Front-rank technologies for measuring converters.

Module 10. Methods and facilities for measuring of non-electrical quantities.

Laboratory trainings are performed by virtual facilities (or virtual instruments) for measuring technique. Virtual instrument (VI) is a program in graphical programming language G. It models the appearance and function of a physical instrument [6].

VI consists of two LabVIEW windows: front panel (containing controls and indicators) and fragment of block diagram (containing terminals, connections and graphical code). The front panel is the user interface of the virtual instrument. It consists of controls and indicators, which are the interactive input and output terminals of the VI, respectively. Controls are knobs, push buttons, dials, and other input devices. Indicators are graphs, LEDs, and other displays.

Controls simulate instrument input devices and supply data to the block diagram of the VI. Indicators simulate instrument output devices and display data the block diagram acquires or generates.

The code is built using graphical representations of functions to control the front panel objects. The block diagram contains this graphical source code. Front panel objects appear as terminals on the block diagram. Additionally, the block diagram contains functions and structures from built-in LabVIEW VI libraries. Wires connect each of the nodes on the block diagram, including control and indicator terminals, functions, and structures.

From the aspect of distance learning, the most important issue of virtual instruments is the fact that they can be used to simulate physical phenomena – to generate signal that appears as it would appear if it had been acquired by real transducers. The same software is being used for real and virtual phenomena. That way virtual instrument becomes the part of virtual laboratory.

Laboratory trainings consist of 15 virtual laboratory setup. Themes of some laboratory trainings are presented below:

- Strain Gage sensors;
- Measuring temperature with an RTD or thermistors;
- Capacitive measuring converters;
- Sensors for measuring acceleration;
- Ultrasonic sensors;
- Sensors for measuring pressure;
- Thermocouples;
- Photo-electrical measuring converters.

The theoretical and practical studies are checked by testing and control works, which allow us to do verification after learning process is done. Practical trainings and semester paper are final parts of study process. They intended for resuming of theoretical knowledge, obtaining the skills for calculation elements of measuring converters, developing and calculations of connection circuits for measuring devices. Calculation-graphic setup allows us to resume the practical skills.

Themes of some practical trainings are resulted below:

- Thermocouples;
- Piezoelectrical measuring converters;
- Sensor for measuring deformation.

We also developed Dictionary of terms and definitions and have recommended references (see fig. 1).

A virtual laboratory for course "Measuring methods and facilities". Also, a virtual laboratory was developed for course "Measuring methods and facilities".

Virtual computer educational laboratories allow to circulate knowledge, experience and pedagogical ability of lecturer; carry out the continuous control under process of knowledge acquisition and, partly smooth out the sharpness of problems in logistical support of educational process just for now. New measuring technologies should be referenced to new technologies of teaching.

In general, a virtual educational laboratory includes theoretical module (electronic textbook or manual), module of laboratory practical work and module for quality verification of trainee's knowledge and their abilities. The other module that may be additionally implemented is electronic book of problems.

Electronic textbook provides necessary theoretical and methodical background for the self-dependent study of theoretical course. Laboratory practical work supplies with a training of practical abilities adequate to the professional requirements in selected specialization. In this training student has to operate with the model of the real objects and independently control the object under study for taking the required characteristics. The main purpose of the electronic block of knowledge verification is provision of the automated routine of knowledge testing that propose for student to estimate objectively the attained level of object after their study.

The instrumental environment LabVIEW satisfies the indicated principles for creation of virtual laboratory practical work. Their "virtual instruments" are able to work with the real objects and their mathematical models. The great importance for student training in technical education is given to laboratory works for study of characteristics of radio engineering objects. The creation of special work place for practical education requires good equipment and financial resources for their support. However, the idea of development their virtual analogue with using of LabVIEW becomes quite obvious and efficient for today. In a virtual laboratory external control instruments and control panel are visually represented adequately to their real analogue where different modes of operation are investigated by simulation or mathematical models.

Fig. 2 shows structure of virtual laboratory.

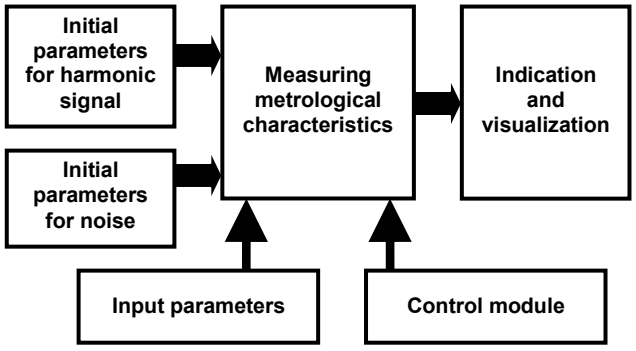

Fig. 2. Structure of virtual laboratory

A virtual laboratory was designed for study of measuring methods and structures of measuring facilities for their realization. It allows for student to form their metrological approach being based on master concepts of metrology, features of error analysis and initial descriptions of facilities for measuring technique. Fields of knowledge that forms the background are metrology, measuring facilities in radio engineering, theory of measuring errors, experimental informatics.

Every laboratory work is presented by theoretical basics and program executable that simulates work of laboratory stand. The theoretical basics contain background notes, schedule of work, methodical instructions for their implementation, requirements for report writing on work and control questions for self-examination.

The program of laboratory work contains list of experiments which are to be realized under studied object, characteristics which are to be taken on research object and values which are to be founded by processing of "experimental" data and then presented in a report.

Within the framework of virtual laboratory the following devices are developed through LabVIEW components: functional generator, oscillograph, measuring device of signal characteristic and spectrum analyzer based on decomposition of signal in the Fourier series.

Student should set up the values of initial parameters for harmonic signal (sample rate, number of samples, frequency, amplitude and initial phase of signals) and noise for determination of set metrological characteristics. The main measured metrological characteristics are the following: amplitude-frequency characteristic, phase-frequency characteristic, measuring errors of amplitude and signal phases. They are calculated per results of measuring for informative parameters of harmonic signal, i.e. amplitude and phase.

The user interface' description to laboratory work "Amplitude measuring for harmonic signal, using discrete Fourier transform" is resulted below. Task of laboratory work:

- amplitude measuring for harmonic signal;
- error's estimation at amplitude measuring, caused by time measuring limitation, absence of signal's synchronization, influence of initial phases of signals;
- estimation of amplitude correction's efficiency. Amplitude correction is calculated from formula:

$$\tilde{\mathbf{U}}_0 = g_{mm}\frac{x}{\sin x},$$

where $x = \pi\dfrac{Z}{1+Z}$; $Z = \dfrac{g_m}{g_{mm}}$; $g_{\max} = g_{mm}$ – maximal sample; g_m – neighbouring sample.

On an oscillogram the amplitude spectrums of harmonic signals are represented.

The user interface' description to laboratory work "Measuring of phases' difference for harmonic signal, using discrete Fourier transform" is resulted below. Task of laboratory work:

- measuring of phases' difference for harmonic signals;
- error's estimation for phases' difference, caused by time measuring limitation, absence of signal's synchronization, influence of initial phases of signals.

In a window of oscillogram the graphic dependence of measuring error for phases' difference of harmonic signals from number of periods, is represented.

Task of laboratory work "Amplitude measuring for harmonic signal with Gaussian noise, using discrete Fourier transform":

- amplitude measuring for harmonic signal with Gaussian noise;
- estimation of signal-to-noise ratio;
- estimation of measuring time for filtration coefficient;
- calculation of parameters for amplitude spectrum.

The signal-to-noise ratio (dB) for two harmonic signals is calculated from formula:

$$\Lambda = 10 * \lg\left[\left(\frac{U^2_{sign.garm} * N}{2\sigma^2_\xi}\right)\right] \Big/ 2,$$

where $U_{sign.garm}$ – amplitude peak in the spectrum of signals $x(t)$ and $y(t)$ on fundamental frequency; N – number of samples; σ^2_ξ – dispersion of noise.

Task of laboratory work "Measuring of phases' difference for harmonic signal with Gaussian noise, using discrete Fourier transform":

- measuring of phases' difference for harmonic signals with Gaussian noise;
- estimation of signal-to-noise ratio;

- error's estimation for phases' difference;
- estimation of measuring time for filtration coefficient.

Metrological characteristics settle accounts with the use of discrete Fourier transform and algorithms of correction for measuring errors. A principle of operation and functioning of automatized workstation for metrolog is in base of a virtual educational laboratory and results in Declarative patent of Ukraine on a useful model [1].

The following tasks were incorporated in virtual laboratory that is presented here:

- measurement of phase differences and amplitude of signals with/without a noise;
- error simulation of phase differences and amplitude of signals;
- determination of signal-noise ratio;
- determination of measuring time for providing of filtration coefficient after assigning a measuring precision of phase differences and amplitude of signals;
- modeling of correction algorithms for increasing of measuring precision of phase differences and amplitude of signals.

Nevertheless, the real time measuring of physical parameters is necessary to provide the detailed training for students and help them for better understanding of measuring procedures and their facilities. In general, the experimental laboratory equipment can be replaced by their virtual analog only in partial manner. It is not assumed here that the virtual models will replace the real equipment (measuring facilities) completely. However, they can be for the students as additional tools that will help them to study the facilities of measuring technique and their management facilities in order to use them for laboratory work or remote education.

Testing in distance education. Traditional accountability methods include reports on quality to federal, regional, or state agencies and accreditation bodies. The audience for systematic assessment of institutional quality lies outside the institution. Quality indicators generally are based on indirect measures of academic performance such as selectivity, academic expenditures, faculty-student ratios, and Carnegie classification. Because these measures do not adequately represent the net effects or value added from higher education, alternatives must be sought [3].

Full accountability is not limited to external audiences. Internal examination of effectiveness is important for institutional growth and development. Pascarella and Terenzini [4] found that educationally effective institutions are differentiated by

- student involvement in the academic and nonacademic systems;
- the nature and frequency of student contact with peers and faculty members;
- interdisciplinary or integrated curricula;
- pedagogies that facilitate learning engagement and application;
- campus environments that emphasize scholarship and provide opportunities for encounters with diverse individuals and ideas;
- environments that support exploration.

These factors are linked to student learning and can be measured in terms of engagement in learning activities and use of space. The assessment of the relationship between Learning Spaces and academic engagement aligns closely with accountability and can be included in the overall assessment plan for the institution.

Another way is using assignments from Open Source Course Management System – Moodle.

Moodle is a software package for producing Internet-based courses and web sites. It is a global development project designed to support a social constructionist framework of education. The assignment activity module allows teachers to collect work from students, review it and provide feedback including grades [2].

Students can submit any digital content (files), including, for example, word-processed documents, spreadsheets, images, audio and video clips. Assignments don't necessarily have to consist of file uploads. Alternatively, teachers can ask students to type directly into Moodle using an online text assignment. There is also an offline activity assignment which can be used to remind students of 'real-world' assignments they need to complete and to record grades in Moodle for activities that don't have an online component.

There are 4 types of assignments:

1. Upload a single file.
2. Advanced uploading of files – options include: multiple file submission, allowing students to type a message alongside their submission and returning a file as feedback.
3. Online text – students type directly into Moodle, teachers can provide inline feedback.
4. Offline Activity – teachers provide a description and due date for an assignment outside of Moodle. A grade and feedback can be recorded in Moodle.

It is possible to create iterative assignments – where the piece of work is graded by the teacher, re-edited by the student, re-graded and so on using either the single file or the online text in the assignment settings.

DE has long had trouble with testing. The delivery of testing materials is fairly straightforward, which makes sure it is available to the student and he or she can read it at their leisure. The problem arises when the student is required to complete assignments and testing. Online courses have had difficulty controlling cheating in quizzes, tests, or examinations because of the lack of teacher control. In a classroom situation a teacher can monitor students and visually uphold a level of integrity consistent with an institution's reputation. However, with DE the student can be removed from supervision completely. Some schools address integrity issues concerning testing by requiring students to take examinations in a controlled setting.

Assignments have adapted by becoming larger, longer, and more thorough so as to test for knowledge by forcing the student to research the subject and prove they have done the work. Quizzes are a popular form of testing knowledge and many courses go by the honor system regarding cheating. Even if the student is checking questions in the textbook or online, there may be an enforced time limit or the quiz may be worth so little in the overall mark that it becomes inconsequential. Exams and bigger tests may be harder to regulate.

Conclusion. Distance learning is an excellent tool to improve engineering education by providing flexibilty to students and teachers. That flexibility can be used to overcome the complexity of engineering study contrary to other fields of education. Not all disciplines are easy to be learned at the distance, since some require expensive laboratory equipment.

Virtual instruments are excellent solution, since they signifficantly decrease costs for laboratory equipment.

1.Automatized workstation for metrolog. – Declarative patent of Ukraine on a useful model, № 6161, MKP G01R35/00. Bull. № 4, 15.04.2005. 2. Cole J. Using Moodle: Teaching with the popular open source course management system. – O'Reilly Media, Inc., 2005. 3. Learning Spaces / Ed. by Diana G. Oblinger. – Boulder, 2006. 4. Pascarella E.T., Terenzini P.T. How college affects students: A third decade of research : In 2 vol. – S.F., 2005. – Vol. 2. 5. Taylor J.C. The fifth generation of distance education // Chinese Journal of Open Education Research. – 2003. – №3. – P. 25–27. 6. Zaimoviæ-Uzunoviæ N., Lemeš S., Petkoviæ D. Virtual instruments – a chance to teach engineering at a distance // 7 International Conference on Engineering Education: ICEE 2001, Oslo, Norway, 2001.

Submitted 29.10.09

UDC 621.315.592

S. Pavljuk, Ph. D., L. Ischuk, Ph. D.,
V. Kislitsyn, Ph. D., O. Oberemok, Ph. D.,
R. Soltys, stud.

EFFECT OF EXTERNAL ELECTRICAL FIELD ON THE NO STATIONARY ABNORMAL HEAT CONDUCTIVITY OF SEMICONDUCTOR DIODE

Проведено дослідження впливу прикладеного до промислового діода КД209 електричного поля на його нестаціонарну аномальну теплопровідність. Показано, що якщо тепловий потік співпадає з напрямком електричного поля, то теплопровідність збільшується, а навпаки – зменшується.

Ключові слова: тепловий потік, електричне поле, теплопровідність.

The investigation of the effect of electric field applied to serial diode KD 209 on the no stationary abnormal heat conductivity was studied. It was shown that the heat conductivity of semiconductor diode is increased, if the heat flow is coincide with the direction of electric field, and vise versa (if the electric field is applied in reverse direction) – the heat conductivity is decreased.

Key words: heat flow, electric field, heat conductivity.

Introduction. Semiconductor diode structure is well known as the heat emitting elements from the time of the past century end. The fact that the flow of electric current through semiconductor structures could heat them up to high temperature was used for soldering of copper filaments to the semiconductor structures by manufacturing of serial diodes KD105, KD 208, KD 209 and KD 211 (prototypes of diodes of 1N400 series) [1].

About ten years ago in Paton Welding Institute of Ukrainian Academy of Science were developed the pilot model of the micro soldering iron with the working tip made of the chip of semiconductor diode [3].

Semiconductor diffusion resistors made on the technological principle of "silicon with dielectric insulation" were used as the heat emitting elements, which are heated by electric current up to temperature needed for spraying of melted silicon [2].

The main feature of all of these examples of practical use is the need to provide conditions for uniformity of heat field in the semiconductor structures. If by chance, we fail to ensure this feature then in these structures could arise the very high temperature gradients followed by mechanical stresses and the destruction of these structures. Therefore, the investigations of heat propagation through multilayer diode structures were carried out and the results of this investigation were described in article [4]. The investigations show that in the diode structures we observe the phenomenon of no stationary abnormal heat conductivity. This means that the speed of heat propagation along the diode structure is dependent from orientation of the p-n structure correspondingly to the heat source. The speed of heat propagation is higher in the direction from *n*- region to *p*- region than in the reverse direction. This effect could be explained that according to [5] in semiconductors the heat conductivity χ in general case is represented in the form of:

$$\frac{\chi}{\sigma T} = \frac{\chi_L}{\sigma T} + \frac{2k^2}{e^2} + \left(4 + \frac{\Delta E}{kT}\right)^2 \frac{k^2 np \mu_e \mu_h}{e^2 \left(n\mu_e + p\mu_h\right)^2},$$

were σ – specific electric conductivity of semiconductor; k – Boltzmann's constant; e – electron's charge; ΔE – prohibited band width; n, p – electron and hole concentration; μ_n, μ_p – mobility of electrons and holes.

The heat conductivity of the diode structure consists not only of phonon conductivity (the first term of equation), but by some circumstances of the electron-hole couples (the third term of equation). If the carrier concentration are $n \approx p$ and $\Delta E >> kT$ then this term of equation could be very high. The contribution of the free carriers in the heat conductivity (the second term of equation) is low and therefore has to be neglected.

The electron-hole couples are aroused in the high resistant n-region of diode due to heat generation, and the width of prohibited band of silicon is higher than kT.

The results of the investigation made in [4] was obtained without external heat supply, because in the praxis the powerful semiconductor devices are heated up due to the heat emitted by the electric current flowing through the semiconductor structure. The influence of the electric current on the no stationary heat conductivity could be very substantial by running of switching or rectifying diodes, transistors and other semiconductor devices in the conditions of alternate voltage and electric current. That is why the object of this study was the investigation of influence of electric current flowing in direct and reverse direction relatively external heater on the no stationary heat conductivity of semiconductor diodes.

Experimental specimens. For this investigation were used semiconductor chips of silicon SEPh-40 with specific resistance of base region ρ = 40 Ohm·cm and donor concentration about 10^{14} cm^{-3} designed for manufacturing of diodes model KD209. The chips were of cylindrical form 0,18 mm diameter and thickness of 0,03 mm. On the one end of the chip were made up to 0,01 cm depth by means of boron diffusion $p+$-region with specific resistance ρ = 0,1 Ohm·cm and acceptor concentration about $10^{17}cm^{-3}$. On the other end of chip by means of phosphor diffusion were made $n+$-region adjoining to n- region of chip.

Experimental bench. The main component of experimental bench is pulse heating element on the top of which were placed the experimental module consisted of diode structure between two temperature compensators made from gold plated Covar alloy each of them having welded thermocouple.

The time of heating of diode structure was varying between 2…10 seconds. The temperature of thermo compensators was checked by means of amplifier and oscillograph with memory block. The dates of the two thermocouples are copied in the memory block of two oscillographs and in the memory of the oscillograph with differential amplifier also to register the temperature difference ΔT between thermocouples fixed on underside and upper side temperature compensators. The experimental module was placed the first time with the n -region and then with $p+$ -region to the heating element and in all these variants were fixed the value of temperatures of both sides of the diode structure contact areas.

With the help of the power unit the diode was loaded up with nominal direct current (0,3 A). In reverse direction to the diode was applied 30 V but the value of electric current was limited by the 100 Ohm resistor.

The measurement technique. The experimental module before beginning of experiments was subjected to preliminary heating for providing of some "pre joining" of all module components (the diode structure placed between the two thermo compensators). The need of this "pre joining" was to make the monolithic block of experimental module, which would not undergo to disassemble without destruction of silicon structure. With the help of this preparation were produced before the beginning of experiment the minimal and invariable heat resistance between butt-ends of p-and n-regions of diode structure and the fixed to them two thermo compensators. In this case were avoided all the negative factors which could alter the value of the heat resistance by changing of $p-n$ junction orientation relatively to the heating element.

The diode was subject to the direct or reverse electric field before the time of the heater switching.

The experimental results. The fig. 1 shows the characteristic temperature curve of the heating element. In fact, it represents the temperature value of thermocouple mounted on the surface of heating element, i.e. underneath of experimental module. The usual time of the experimental module heating up to 500 ^{o}C is about 8 seconds. After this time the temperature of the heating element and the experimental module were stabilized. The highest level of the temperature and the speed of its rising are varied by the electric power supplied to the heating element.

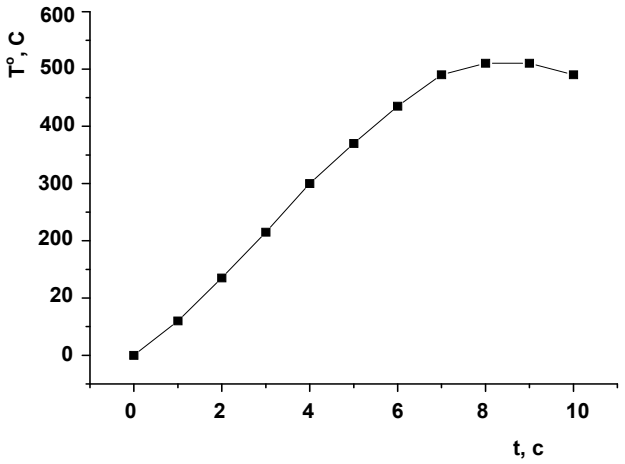

Fig. 1. Characteristic temperature curve of the heating element

The fig. 2 shows the temperature difference ΔT between the thermocouples fixed on the upper and lower thermo compensators of experimental module on the stage of heating. In the case of absence of external electric field the heat flows in direction from p- to n- region (see the temperature curve 1 by E = 0). In the case the diode loaded with direct current of I_d = 0,3A (the nominal direct current value of diode KD209) we see the decreasing of the temperature difference ΔT (the temperature curve 2, E ↑).

If the diode is subjected by reverse electric field the temperature difference ΔT is increased (the temperature curve 3, E ↓).

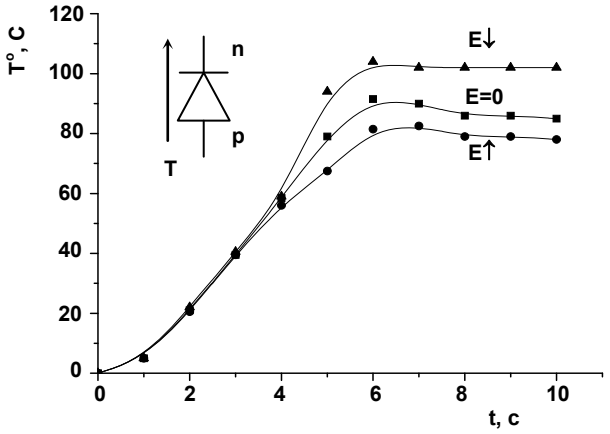

Fig. 2. Temperature difference ΔT between the thermocouples fixed on the upper and lower thermo compensators of experimental module on the stage of heating

The fig. 3 represents the same experimental results made by reversed orientation of diode structure placed on the heating element. In this case the heat flows in the direction from n- to p- region. By coincidence the directions of heat flow T and electric field E the temperature difference ΔT is decreased (see the temperature curve 2, E ↑), and by reversed electric current the temperature difference ΔT is increased (see the temperature curve 3, E ↓).

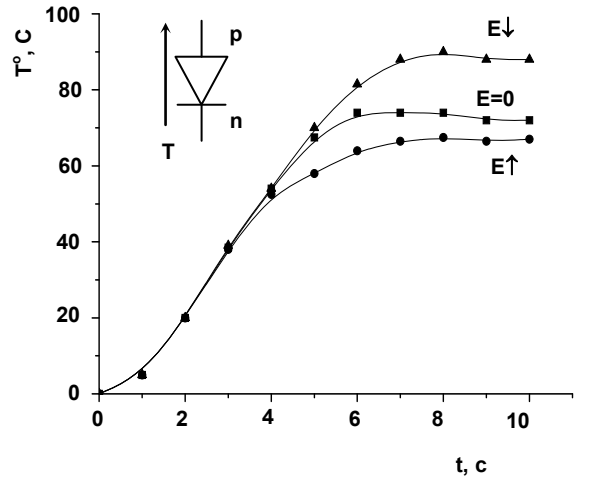

Fig. 3. Temperature difference ΔT between the thermocouples by reversed orientation of diode structure placed on the heating element

The fig. 4 represents the dependence of the direct drop voltage by loading of diode with the direct electric current 0,3 A. The rapid drop of U_{np} on the diagram shows that in 4 – 5 sec after beginning of heating there are some characteristic change of the diode structure occurred.

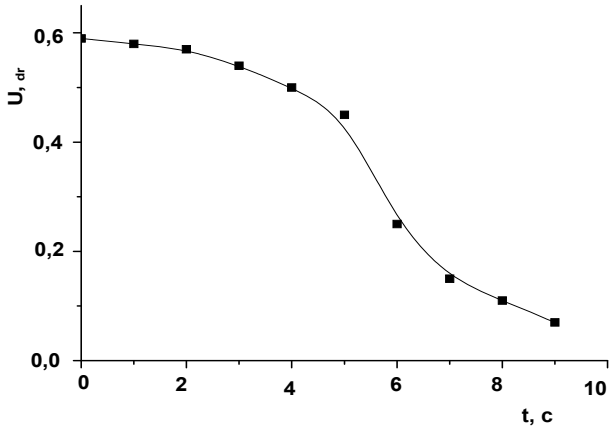

Fig. 4. Dependence of the direct drop voltage by loading of diode with the direct electric current 0,3 A

The fig. 5 represents the rapid rise of electric current through the diode in reverse direction.

By applying to the diode of reverse voltage U_{rev} = 30 V the current limited by resistor (100 Ohm) reaches up to 0.3 A in 4 – 5 sec after beginning of heating also.

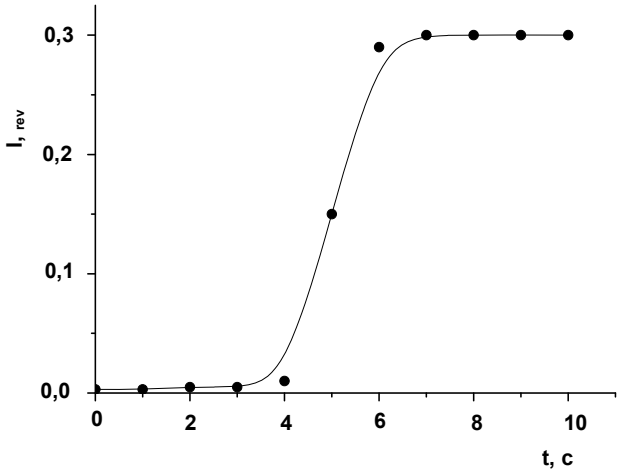

Fig. 5. Rapid rise of electric current through the diode in reverse direction

Discussion. The results obtained in this experiment can be explained in this way. If by pulse heating of diode the heat flow is directed from n- to p- region of diode structure the speed of heat propagation is higher than the speed of heat propagation by reverse orientation relatively to the heating element. The difference between the temperatures measured by underside and upper side thermocouples ΔT is less than it is measured by reversed orientation of the experimental module relatively to the heating element (see the graph. 1 on the fig 2, 3). The results coincide with the results obtained in article [4].

The external electric field promotes the current flowing across the diode structure. If the direction of this electric current coincides with the direction of heat field and the direction of the thermodiffusion, then in the result it increase the amount of heated carriers. This connected with the fact that electrons and holes injected from the $p-n$ junction are heated also and are carried away by the heat flow. They give its additional energy to the atom lattice in the process of recombination and in the same way they increase the velocity of heat propagation. This explanation is confirmed by the experimental data of dependence of temperature difference ΔT (see the graph 1 and 2 on the fig. 2 and 3).

When the direction of electric field does not coincides with the direction of heat flow there are decreasing of heat propagation velocity observed and ΔT is increased (compare the graph 1 and 3 on the fig. 2 and 3). It can be connected by the fact that electric field counteract to the diffusive heat flow.

There is a need to mark that influence of the electric field on the heat flow is observed only by high concentration of electron-hole couples. By the process of direct electric current flowing through the diode crystal there we have an equation for injected electron-hole couples calculation: $n = j/e(\mu_n + \mu_p)$ by $n = p = A_{\exp}(-\Delta E / kT)$ that gives value about 10^{16}см$^{-3}$. This concentration of injected electron-hole couples is very close to the value of thermogenerated couples (which are generated in silicon by the process of heating).

By the temperature of intrinsic electric conductivity (about 300 ^{o}C) there are the voltage drops on the diode (fig. 4) due to increased number of thermogenerated electron-hole couples. By reverse polarity of electric current relatively the $p-n$ junction it is notably the influence of electric current of value 0,3 A flowing in inverse direction on heating up to the temperature of intrinsic silicon conductivity (fig. 5). In accordance with the dependence shown on fig. 1 the temperature of intrinsic electric conductivity of diode structure is attained in 4 – 5 second after beginning of heat process. Exactly in this moment is observed the influence of electric field on heat conductivity.

Conclusions. The results of experiment show that by means of external electric field we can change the abnormal transient heat conductivity, to rise or to low it depending on the direction of electric field. It is shown that these influences of electric field on heat conductivity reveal its importance only after heating of high resistance region of diode up to temperature of intrinsic electrical conductivity.

1 Авт. свид. СССР №. 355696. Способ сборки полупроводниковых приборов. Россошинский А.А., Лебига В.А., Кислицын В.М., Альперович Е.А. – 1972. – Бюл. № 31. 2. Кушниренко В.В, . Нинидзе Г.К, Коноваленко Л.Д.,. Павлюк С.П. Исследование кремниевых диффузионных резисторов при протекании импульса тока большой плотности. //Технология и конструирование радиоэлектронной аппаратуры. 2005.– № 5 (59). – с. 23-26 3. Павлюк С.П., Кутлин Г.Н., Кислицын В.М., Россошинский А.А. Использование кремния в качестве полупроводниковых элементов микропаяльников. //"Автоматическая сварка". –1999. – с. 41-44. 4. Pavljuk S., Ishchuk L., Kislitsyn V.. Thermal conduction anisotropy of the diode structures. Вісник КУ, серія "Радіофізика та електроніка". 2009. – Вип. 12. – с. 33-35. 5. Смит Р. Полупроводники. – М.– 1982

Submitted 18.01.10

UDC 539.951

P. Parashchenko, stud., I. Anisimov, Doct. Sci.

ON THE POSSIBILITY TO USE TRANSITION RADIATION OF ELECTRON BUNCH WITH TRIANGULAR DENSITY PROFILE FOR DIAGNOSIS OF INHOMOGENEOUS PLASMA

Розглядається можливість діагностики плазмової неоднорідності за перехідним випромінюванням електронного згустку з трикутним профілем концентрації густини струму. Розрахунок виконано в наближенні заданого струму, оскільки для такого згустку вплив збуджених ним кільватерних хвиль на його динаміку є незначним. Підтверджена можливість застосування запропонованого методу діагностики неоднорідної плазми та визначені межі його застосовності.

Ключові слова: неоднорідна плазма, електронний згусток, перехідне випромінювання, кільватерні хвилі.

The possibility of plasma inhomogeneities' diagnostics via transition radiation of the electron bunch with initially triangular profile of the current density was considered. The calculations were performed in the given current approximation, because deformation of such a bunch with excited wake waves was negligible. The possibility of application this method of diagnostics of inhomogeneous plasma was confirmed and the range of its applicability was specified.

Key words: inhomogeneous plasma, electron bunch, transition radiation, wake waves.

1. Introduction. Method of inhomogeneous plasma diagnostic via transition radiation has been proposed in [1]. Although so far it has not been confirmed experimentally, theoretical calculations and computer simulations for detailed research were carried out. Particularly, the possibility of diagnostics of the plasma inhomogeneities via HF (non-resonant) transition radiation of modulated electron beam [1], short electron bunch [2-3] and the resonant transition radiation of this bunch [4] was studied. The possibility to use electron bunches is not desirable, because during the bunch motion in plasma moves to the excitation of wake waves, perturbing the motion of electron bunch and consequently its initial density profile [5]. Long enough initially bunch begins to decay on microbunches. Therefore, the calculation of transition radiation fields of such a system becomes too complex, and the solution of the inverse problem is impossible. The radiation of short bunch can be used, but it's extremely low. So registration of the radiation field becomes substantially more complicated.

The bunch with initially triangular profile of the current density [6] is considering in our work. Simulation results [8] confirm that such a bunch with the sloping rising edge and steep falling edge excites wake waves mainly with its falling edge. So deformation of such a bunch will be significantly less than for the bunch with initially rectangular density profile. Therefore, the calculation for triangular bunch can be carried out in the given current approximation.

2. Description of the physical model. Cold isotropic plasma is considered, its density depends only on z coordinate, and $n(z \to \pm\infty) \to 0$. Axially symmetrical radially restricted electron bunch with a given current density moves along the plasma density gradient with the velocity v_0:

$$j(r, z, t) = qn(z,t)v\Phi(r), \qquad (1)$$

where q is the bunch charge, $\Phi(r)$ is the function that characterizes the current density distribution in the bunch cross-section $(\Phi(r \to \infty) \to 0)$, $n(z,t)$ is the triangular density profile along z axis:

$$n(z,t) = \begin{cases} n_0(1-\frac{\xi}{L}), & 0 < \xi < L, \\ 0, & \xi \le 0, \xi \ge L, \end{cases} \qquad \xi = z - vt. \qquad (2)$$

Calculations are performed in the given current approximation. High frequency (non-resonant) component will be found out, because solution of since the inverse problem for this case is much simpler.

3. Analytical calculation. Magnetic field excited with the current (1) in plasma satisfies the wave equation:

$$\frac{\partial}{\partial r}\left[\frac{1}{r}\frac{\partial}{\partial r}\left(rH_\varphi^0\right)\right] + \frac{\partial^2 H_\varphi^0}{\partial z^2} - \frac{1}{\varepsilon(z)}\frac{\partial \varepsilon(z)}{\partial z}\frac{\partial H_\varphi^0}{\partial z} + k_0^2\varepsilon(z)H_\varphi^0 = \frac{4\pi}{c}\frac{\partial j}{\partial r}, \qquad (3)$$

$$\varepsilon(z) = 1 - \frac{4\pi n(z)e^2}{m\omega(\omega + i\nu)}. \qquad (4)$$

Let us substitute to (3) the solution in the form of Fourier integral:

$$H_\varphi^0(r,z) = \int_{-\infty}^{\infty} H_\varphi(r,z)\exp(i\omega t)d\omega, \qquad (5)$$

$$j(z,t) = \int_{-\infty}^{\infty} j(z,\kappa)\exp(i\omega t)d\omega, \qquad \kappa = \omega/v. \qquad (6)$$

For the chosen form of bunch

$$j(z,\kappa) = -\frac{qn_0}{2\pi}n(\kappa)\exp(-i\kappa z), \qquad (7)$$

$$n(\kappa) = \frac{1}{\kappa^2 L}\left[1 + i\kappa L - \exp(i\kappa L)\right]. \qquad (8)$$

After substituting (5) – (6) to (3) one can obtain the equation for high-frequency component of magnetic field:

$$\frac{\partial}{\partial r}\left[\frac{1}{r}\frac{\partial}{\partial r}\left(rH_\varphi\right)\right] + \frac{\partial^2 H_\varphi}{\partial z^2} - \frac{1}{\varepsilon(z)}\frac{\partial \varepsilon(z)}{\partial z}\frac{\partial H_\varphi}{\partial z} + k_0^2\varepsilon(z)H_\varphi = \frac{4\pi}{c}j(z,\kappa)\frac{\partial}{\partial r}\left[\Phi(r)\right]. \qquad (9)$$

Solution of this equation can be presented as the Fourier – Bessel integral by radius:

$$H_\varphi(r,z) = \int_0^{\infty} h_\varphi(k_r,z)J_1(k_r r)k_r dk_r, \qquad (10)$$

Substituting (10) to (9) one can get the equation for h_φ:

$$\frac{d^2 h_\varphi}{dz^2} - \frac{1}{\varepsilon}\frac{d\varepsilon}{dz}\frac{dh_\varphi}{dz} + \left(\varepsilon k_0^2 - k_r^2\right)h_\varphi = \frac{2qv}{c}n(\kappa)k_r\Phi(k_r)\exp(-i\kappa z), \qquad (11)$$

$$\Phi(k_r) = \int_0^{\infty}\Phi(r)J_0(k_r r)rdr. \qquad (12)$$

Suppose that the radiation frequency ω is high enough to satisfy the condition:

$$|\Delta(z)| << 1, \qquad \Delta(z) = 1 - \varepsilon(z). \qquad (13)$$

Then equation (11) can be solved using the successive approximation over the small parameter Δ:

$$h_\varphi = h^{(0)} + h^{(1)} + \ldots \qquad (14)$$

Equations of zero and first approximations have a form, respectively:

$$\frac{d^2h^{(0)}}{dz^2}+k_z^2h^{(0)}=\frac{2qv}{c}n(\kappa)k_r\Phi(k_r)\exp(-i\kappa z),\qquad k_z^2=k_0^2-k_r^2; \tag{15}$$

$$\frac{d^2h^{(1)}}{dz^2}+k_z^2h^{(1)}=\left(k_0^2\Delta+i\kappa\frac{d\Delta}{dz}\right)h^{(0)}. \tag{16}$$

The solution of (15) that describes the field of electron bunch without plasma has the form:

$$h^{(0)}=\frac{2qvn(\kappa)k_r\Phi(k_r)}{c\left(k_z^2-\kappa^2\right)}\exp(-i\kappa z). \tag{17}$$

Scattering of the field (17) on the plasma inhomogeneities forms the transition radiation. The solution of equation (16) corresponding to the lack of electromagnetic waves falling on the plasma inhomogeneity has the form [7]:

$$h^{(1)}=f_+\int_{-\infty}^{z}\frac{f_-F}{W}dz+f_-\int_{z}^{+\infty}\frac{f_+F}{W}dz, \tag{18}$$

where $f_\pm=\exp(\mp ik_z z)$ are solutions of (16) without the right part, corresponding to electromagnetic waves running to right and to the left along z axis, $W=-i2k_z$ is their Wronskian, F is the right part of (16). Amplitude of forward and backward radiation, respectively, can be written as:

$$h_m^{(1)}(z\to\pm\infty)=\int_{-\infty}^{+\infty}\frac{f_\pm F}{W}dz. \tag{19}$$

Function $\Delta(z)$ should be presented as Fourier integral to calculate integral (19):

$$\Delta(z)=\int_{-\infty}^{+\infty}\Delta(K)\exp(iKz)dK. \tag{20}$$

One can obtain after substituting (20) to (19) and changing the order of integration:

$$h_m^{(1)}(z\to\pm\infty)=2\pi iqvn(\kappa)k_r\Phi(k_r)\times \times\frac{\Delta(\kappa\mp k_z)\left(k_0^2-\kappa^2\pm k_z\kappa\right)}{ck_z\left(k_z^2-\kappa^2\right)}. \tag{21}$$

Solution (21) should be substituted to (10). For $k_r>k_0$ solutions describe surface waves with amplitude decreasing exponentially with $|z|$ increase. Therefore, integration for the radiation in the far zone should be carried out in the interval $0\le k_r\le k_0$.

It is suitable to turn from variable k_r to variable Θ defined from relations

$$k_z=k_0\cos\Theta,z\to+\infty;\qquad k_z=-k_0\cos\Theta,z\to-\infty. \tag{22}$$

It is also suitable to use the spherical coordinate system: $r=R\sin\Theta$, $z=R\cos\Theta$. Combining integrals for forward and backward radiation one can get:

$$H_\varphi(R,\theta)=\frac{i2\pi k_0^2qvn(\kappa)}{c}\int_0^\pi\frac{J_1(k_0R\sin\theta\sin\Theta)}{\left(k_0^2\cos^2\Theta-\kappa^2\right)}\times \times\Delta(\kappa-k_0\cos\Theta)\sin^2\Theta\left(k_0^2-\kappa^2+\kappa k_0\cos\Theta\right)\times \times\Phi(k_0\sin\Theta)\exp(-ik_0R\cos\theta\cos\Theta)d\Theta. \tag{23}$$

The far radiation zone corresponds to the case $R\to\infty$. Then integral (23) can be calculated using the stationary phase method. Replacing the Bessel functions with their asymptotics one can get:

$$H_\varphi(R,\theta)=\frac{2\pi k_0^2qvn(\kappa)\Delta(\kappa-k_0\cos\theta)}{c\left(\kappa^2-k_0^2\cos^2\theta\right)}\times \times\Phi(k_0\sin\theta)\left(k_0^2-\kappa^2+\kappa k_0\cos\theta\right)\sin\theta\frac{\exp[-ik_0R]}{k_0R}, \tag{24}$$

where $0\le\theta\le\pi$, and $n(\kappa)$ is given by (8).

4. Discussion. Analysis of the HF magnetic field H_ϕ (24) in the far radiation zone shows that spatial spectrum of plasma inhomogeneities in the range of K from $\kappa-k_0$ to $\kappa+k_0$ can be obtained from the measurements of radiation field in the range of θ from 0 to π.

For non-relativistic bunches $\kappa=\omega/v$, $k_0=\omega/c$, and $\kappa>>k_0$, because $c>>v$, so such a range will be relatively narrow and will not give the sufficient information about the function $\varepsilon(z)$. However, for the relativistic bunch one can obtain $\kappa\approx k_0$, so the function $\Delta(K)$ can be found out in the range from 0 to $2k_0$. If the characteristic size l of the inhomogeneity $\varepsilon(z)$ is significantly less than the vacuum wavelength of the transition radiation,

$$\lambda=\frac{2\pi}{k_0}\le l, \tag{25}$$

the plasma density profile can be found from the spectrum $\Delta(K)$.

In the experiment the studied radiation must not be very small. It follows from (24) that this condition is always violated when $\Theta\to0$ and $\Theta\to\pi$. For relativistic beam ($\beta=v/c\le0.62$) there is another zero of function $H_\varphi(\theta)$ appears when $\theta=\arccos(\beta^{-1}-\beta)$. It should also be aware that the radiation of the ultra-relativistic bunch is focused in the range of θ near 0 and π and gives very limited information about $\varepsilon(z)$. Thus, moderately relativistic bunches ($v/c\approx0.9$) are the most convenient for the plasma inhomogeneities' diagnostics.

For $\Theta\to0$ always $\Phi(k_0\sin\theta)\to1$. This function vanishes for $\sin\theta\ge4/k_0a$, where a is the bunch radius. Therefore, bunches with the radius of the order of the radiated waves' length are preferable.

The normalized spectral function (8) is plotted on Fig. 1. Half-width of the spectrum range is $\Delta\kappa\approx3.4/L$, where L is the bunch length. Diagnosis of plasma inhomogeneity $\Delta(K)$ is possible only if the spectral width of the function $\Delta\kappa$ exceeds the width of function $\Delta(\kappa-k_0\cos\theta)$ that is approximately $2\pi/l$, where l is the characteristic length of the plasma inhomogeneity. This condition can be presented in a form:

$$l>>L. \tag{26}$$

Therefore, selecting the appropriate length of bunch, one can always satisfy the condition (26).

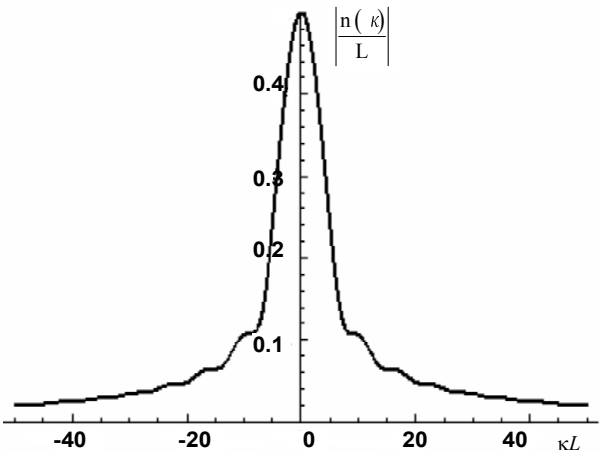

Fig. 1. Normalized spectral function n(κ)

The charged bunch moving in plasma excites a wake waves, so the minimum deformation of the initial current density profile takes place for the next condition:

$$L > \lambda_{kilv.} = \frac{2\pi v}{\omega_p}, \qquad (27)$$

where for relativistic bunches $v \approx c$. Combining conditions (26)-(27), one can get:

$$l >> L > \lambda_{kilv}. \qquad (28)$$

Therefore, the diagnostics of plasma inhomogeneities via transition radiation in the analyzed case is possible only under the condition (29).

5. Conclusions. One can obtain the spatial spectrum of $\varepsilon(z)$ in the range of wave numbers from $\kappa - k_0$ to $\kappa + k_0$ from the measurements of the high-frequency (non-resonant) transition radiation excited by the charged bunch with initially triangular profile moving in the inhomogeneous plasma. The frequency of transition radiation should exceed significantly the Langmuir frequency. The bunch should be moderately relativistic, and its radius must be less than the wavelength of the transition radiation. The bunch length must be large in the scale of the wake wave length and much less than the characteristic length of the plasma inhomogeneities.

1. Anisimov I.O. Transition radiation of modulated electron beam as a method of plasma formations diagnostic. // Ukr. Fiz. Zhurn. Vol.41. № 9. 1996. (In Ukrainian). 2. Anisimov I.O., Lyubich K.I. Transition radiation of charged bunch as a method of plasma formations diagnostic. // Ukr. Fiz. Zhurn. Vol.42. № 8. 1997. (In Ukrainian). 3. Anisimov I.O., Blazhko I.A. Computer simulation of plasma formations diagnostics via transition radiation of modulated electron beam. // Kyiv University Bulletin. Physics and Mathematics. Vol.3. 1999. 4. Anisimov I.O., Lyubich K.I. Plasma-object diagnostics via resonant transitional radiation from an electron bunch. // Journal of Plasma Physics. Vol.66. Part 3. 2001. 5. Anisimov I.O., Tolochkevich Yu.M. Dynamics of One-dimensional Electron Bunch with the Initially Rectangular Density Profile Injected Into Homogeneous Plasma. // Ukr. Journ. of Phys. 2009, Vol.54, No5. 6. Joshi Ch., Katsouleas T. Plasma Accelerators at the Energy Frontier and on Tabletops. // Physics Today, 2003, Vol.56, No6. 7. Rogashkova A.I. Electromagnetic radiation of non-relativistic electron beam in an inhomogeneous isotropic waveguide. // Zhurn. Tekhn. Fiz. 1976. Vol.46.№12. 8. Tolochkevych Yu.M., Anisimov I.O. Wake waves excitation by electron bunch with initially triangular density profile. // Proceedings of the IV International Conference "Electronics and Applied Physics". October, 23-25 , 2008, Kyiv, Ukraine.

Submitted 26.10.09

UDC 535

D. Parhomenko, post grad. stud.,
S. Kolenov, PhD, E. Smirnov, PhD

2D PHOTONIC CRYSTALS PROPERTIES AS AFFECTED BY DEFORMATIONS

В даній статті досліджено властивості двовимірного фотонного кристалу з квадратною фотонною граткою під впливом механічних деформацій. Авторами використано метод розкладу за плоскими хвилями (PWE) для аналізу фотонних заборонених зон. Обраховано ефективний коефіцієнт заломлення деформованого фотонного кристалу для різних типів деформацій та співвідношення пружних властивостей матеріалів що утворюють цей фотонний кристал. Дано визначення фотонного фотопружнього ефекту. Чисельним моделюванням показано можливість обчислення зміни показника заломлення при складних деформаціях як лінійної комбінації простих деформацій в структурах з квадратною граткою. Отримано виродження фотонних мод при періодичних деформаціях.

Ключові слова: фотонний кристал, зона структура, фотопружність, деформація.

2D silicon-based square lattice photonic crystals properties under the influence of mechanical deformations are considered in this paper. The PWE (Plane Wave Expansion) method was used by the authors for photonic bandgap analysis. Effective refraction of deformed photonic crystal was calculated for different deformations and materials' elastic properties. The photonic photoelastic effect was defined. The possibility to calculate refraction variations separately and to add them algebraically in case of complex (periodicity and interfaces) deformations was shown by the numerical modeling for square lattice photonic crystals. Mode degeneration was observed for periodical deformations.

Key Words: photonic crystal, bandgap, photoelasticity, deformation.

Introduction. Last times photonic bandgap materials have attracted increasing interests of photophysics and optoelectronics communities due to the possibility of controlling light propagation through the materials [4, 6, 10]. More recently, a growing number of research papers have specifically reported the tunability of bandgap in photonic crystals. For example, various techniques of bandgap tuning have been demonstrated by applying an electric field [11], temperature [13, 14], and a magnetic field [9], as well as by infiltrating liquid crystals. In addition, mechanical strain has also been examined as an alternative for band-structure modifications and, possibly, for tuning the bandgaps in photonic crystals as desired [5]. Also acoustooptic effect in photonic crystal is predicted [1, 7, 8, 12]. In this paper, we investigate the modification of dispersion properties for light waves in photonic crystals and effective refraction evolution undergoing mechanical deformation. Static deformations and acoustic wave model for periodic deformations were considered.

Theoretical model. Consider the 2D square photonic crystal structure consisting of a silicon matrix and cylindrical air rods. Schematically this structure is represented in Fig.1(a). Calculations were provided for the fields with wave vector in the *x-y* plane. The eigenmodes are classified into two categories according to their polarization for this case, that are: the ***E*** polarization for which the electric field is perpendicular to the *x-y* plane and the ***H*** polarization for which the magnetic field is perpendicular to the *x-y* plane. Figure 1(b) shows the 2D first Brillouin zone of the square lattice. The first Brillouin zone is defined as the intersection of all half-spaces containing the origin. By definition, all the values for **k** which lie outside this zone can be

reached from within the zone using the translations of the vectors **G**. Therefore, these values are redundant. In other terms, it suffices to consider the variation of **k** within the Brillouin zone for representing the entire set of the dispersion curves of the photonic crystal. The range over which **k** is considered can be further reduced by using the symmetries of the crystal [10], as is illustrated in Fig. 1(b) the irreducible Brillouin zone for square photonic lattice has triangle *ΓXM* shape.

The investigation model was defined as a 2D photonic crystal formed in a silicon matrix with $\varepsilon = 11{,}56$ and composed of circular air $\varepsilon = 1$ cylinders with filling factor $f = 0{,}5$. The dispersion properties for light waves in photonic crystal were calculated by means of plane-wave expansion method (PWE, [2]).

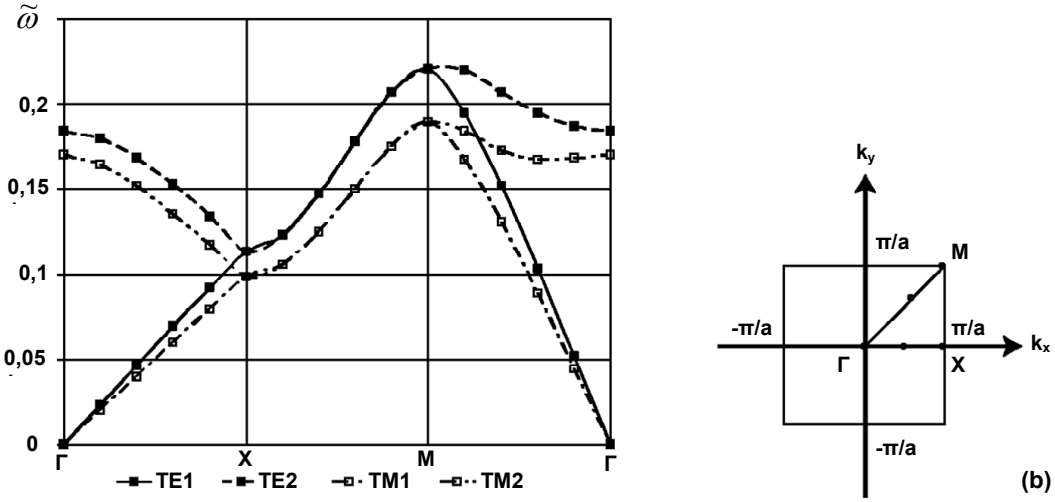

Fig.1. (a) 2D square lattice photonic crystal composed of circular cylinders; (b) First Brillouin zone of the this lattice

Static deformations. We are discussing three cases of static structure deformation: deformation of interfaces between inclusions and matrix without lattice periodicity variations; lattice deformation without changing interfaces between inclusions and matrix; complex deformation – variations of lattice periodicity and interfaces between inclusions and matrix.

All calculations were provided in normalized coordinates. Normalized frequencies are defined as:

$$\tilde{\omega} = \frac{\omega a}{2\pi c}$$

And normalized wave vectors are defined as:

$$\tilde{k} = \frac{ka}{2\pi}$$

Let's consider the first case: deformation of interfaces between inclusions and matrix without lattice periodicity variations (Fig.2).

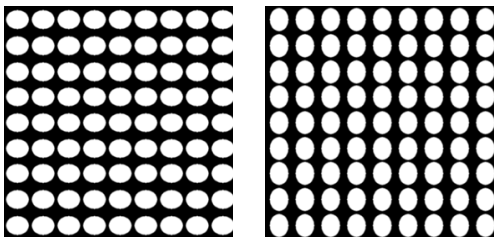

Fig.2. Rods deformation model

Deformed photonic crystal has induced anisotropy: different properties along axis *x* and *y*. To take in account this fact we should consider irreducible Brillouin zone as a square. Here we consider triangle irreducible Brillouin zone, but separate for the two cases: stretching and compressive deformation. This is the same to expand irreducible Brillouin zone to square.

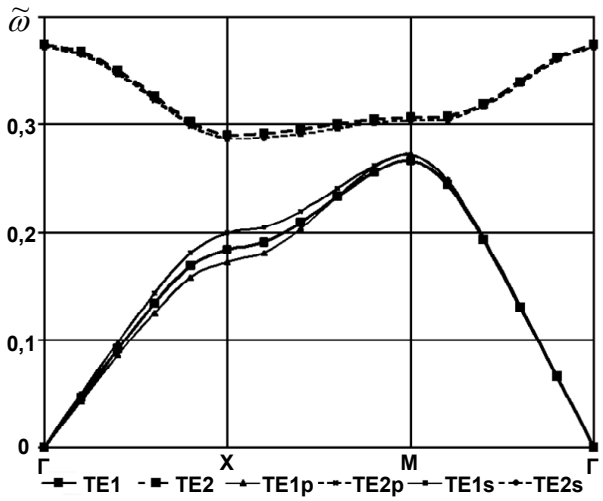

Fig. 3. TE dispersion curves for rods deformation

Calculated in this way the 2D photonic band structure for TE modes is illustrated in Fig.3. The indexes *s* and *p* denote stretching and compressive deformation. It is possible to observe in the graphs that the most influential deformation effect on the TE1 mode is in direction *X*. For the TE2 mode deformation does not have a significant influence on the photonic crystal properties.

Similar calculations for the TM modes are shown in Fig.4. For TM1 mode as for TE1 the deformation effect on the photonic structure properties is observed in the *X* direction but it is not so big. In contrast to TE2 mode for TM2 mode the deformation effect on the photonic structure properties is significant along the full *XM* section and has a maximum in point *M*.

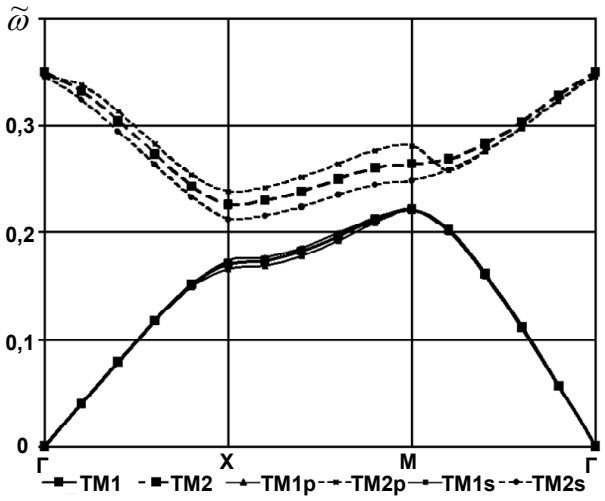

Fig.4. TM dispersion curves (rods deformation)

Let's define effective refractions for the TE and TM modes such as it is usually defined for a homogenous medium:

$$n_{TE,TM} = \frac{k_{TE,TM} c}{\omega\left(k_{TE,TM}\right)}$$

Photonic crystal dispersion curve $\omega\left(k_{TE,TM}\right)$ is calculated numerically. Effective refraction for this structure depends on the light wavelength and on the incident beam angle. There also exists a significant dependence from the filling factor of photonic crystal. Let's fix a wave vector in the photonic crystal (both: by value and by direction) and consider what the changes are for the different modes' eigenfrequencies under the deformation influence in the current structure. In this way we implicitly obtain curve for the reciprocal effective refraction:

$$\omega\left(\frac{1}{n_{TE,TM}}\right) = \frac{1}{n_{TE,TM}} k_{TE,TM} c$$

Or in normalized frequency and wave vector definition:

$$\tilde{\omega}\left(\frac{1}{n_{TE,TM}}\right) = \frac{1}{n_{TE,TM}} \tilde{k}_{TE,TM}$$

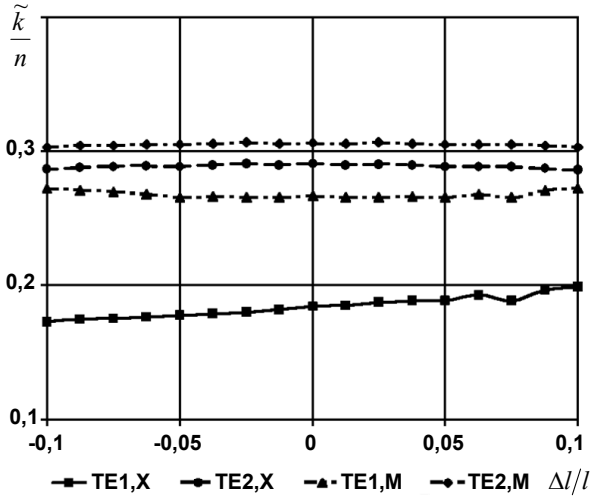

Fig.5. TE reciprocal refraction vs. rods deformation

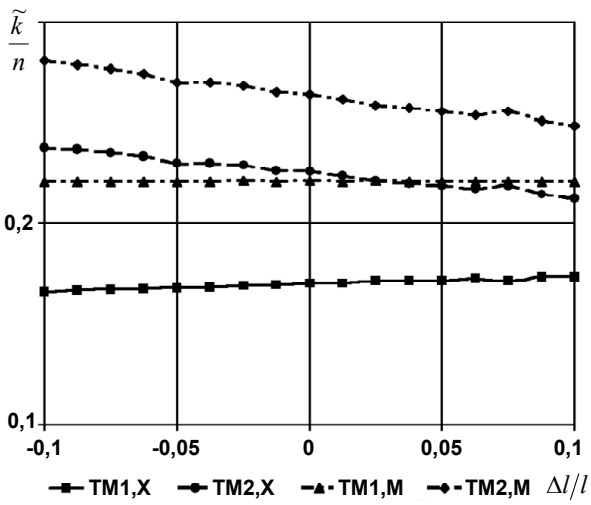

Fig.6. TM reciprocal refraction vs. rods deformation

The reciprocal effective refraction for the TE modes is shown in Fig.5. We illustrate here curves for the two fixed wave vector directions in phonic crystal: *X* direction (marked by *X*, wave vector *ΓX*) and *M* direction (marked by *M*, wave vector *ΓM*). The choice of these directions was based on the results obtained from Fig.3 and Fig.4. As it is possible to observe, in these directions the behavior of the system is the maximum affected by the influence of elastic deformations. Along axis *x* the relative deformation is presented. The sign means stretching or compressive deformation. Along axis *y* we specially represent reciprocal effective refraction multiplied by normalized wave vector to separate the curves on the graph. To take a reciprocal effective refraction value you should divide the *y* value by the normalized wave vector magnitude (e.g. for the *X* direction $\tilde{k} = 0{,}5$ and for the *M* direction $\tilde{k} = 0{,}707$ in the first Brillouin zone).

As was noted above, the most significant photonic photoelastic effect is observed for the TE1 mode in the X direction.

For TM modes the most significant photonic photoelastic effect is observed in the second Brillouin zone (mode TM2) for both directions (see Fig.6).

The second case: lattice deformation without changing interfaces between inclusions and matrix (Fig.7). Physically this model is possible if the mechanical properties of matrix and inclusion are different e.g. elasticity of inclusion is much more that elasticity of matrix.

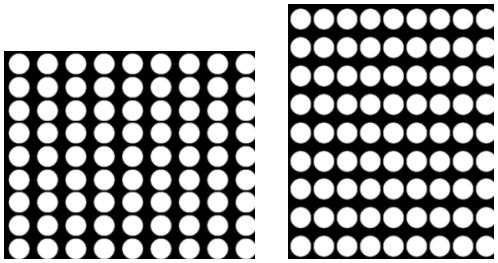

Fig.7. Lattice deformation model

The photonic band structure for the TE modes is illustrated in Fig.8. As opposed to the previous case the photonic photoelastic effect is significant for the both TE modes, but also is not valuable in the *M* direction.

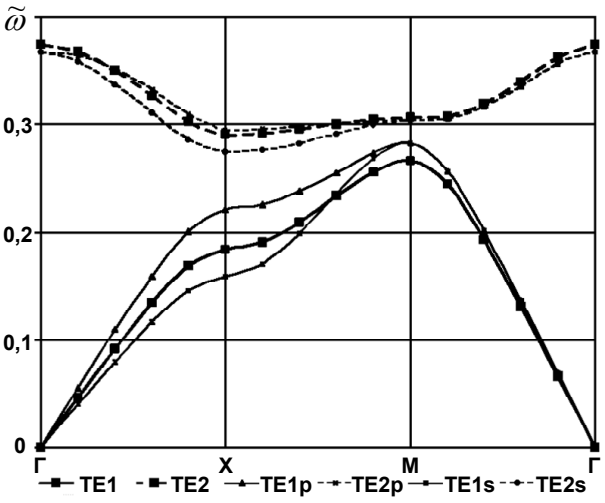

Fig.8. TE dispersion curves for cell deformation

The same calculations for the TM modes are shown in the Fig.8. For TM1 mode as for TE1 the deformation influence on the photonic structure properties observed in the *X* direction is more significant than in the previous case. In contrast, for TM2 mode the influence on the photonic structure is significant only in the *M* direction.

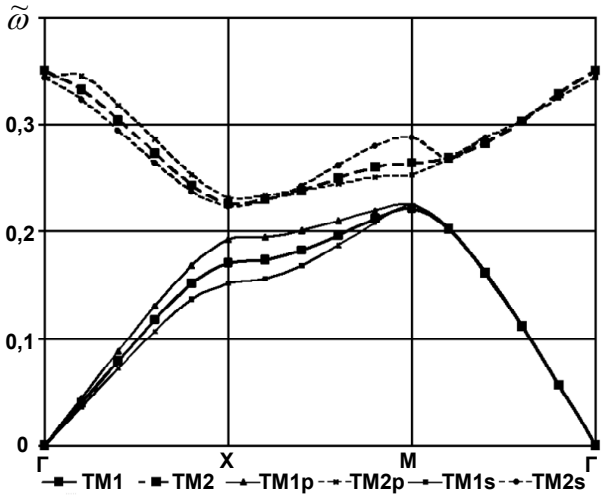

Fig.9. TM dispersion curves for cell deformation

The reciprocal effective refraction for the TE modes is shown in Fig.9. Note that for TE1 mode reciprocal effective refraction in the *X* direction is decreasing in contrast to the previous case.

TM modes have the most significant photonic photoelastic effect in the *X* direction for the TM1 mode and in the *M* direction for the TM2 mode (Fig.11). The reciprocal effective refraction curves slopes are also in opposition to the previous case.

And the last, complex deformation case – variations of lattice periodicity and interfaces between inclusions and matrix. This type of static deformation is the most natural. It could be observed for every photonic structure if the elasticity of the inclusion has the same order as the elasticity of the matrix.

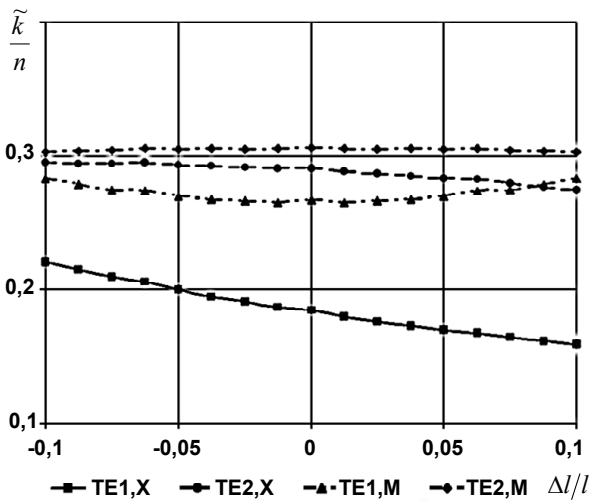

Fig.10. TE reciprocal refraction vs. cell deformation

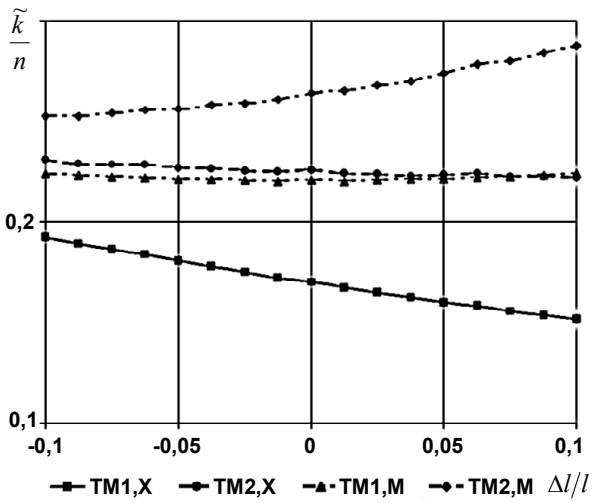

Fig.11. TM reciprocal refraction vs. cell deformation

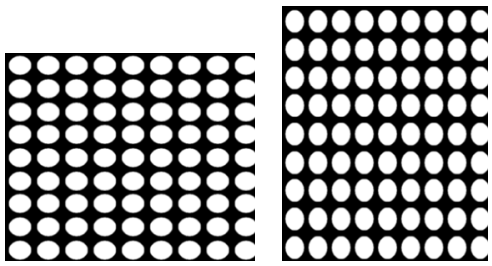

Fig.12. Complex deformation model

The photonic band structure for the TE modes is illustrated in Fig.13. It looks as average of the two previous cases. The photonic photoelastic effect is significant for both TE modes, but not valuable in the *M* direction.

Calculations for the TM modes are shown in Fig.14. The photonic TM modes' photoelastic behavior under complex deformation is similar to the dispersive curves of the TE modes. We obtained the same significant photonic photoelastic effect for both TM modes, but it is also not big in the *M* direction.

The reciprocal effective refraction for the TE modes is shown in Fig.15. The slope of reciprocal effective refraction curve is not zero only for both TE modes in the *X* direction.

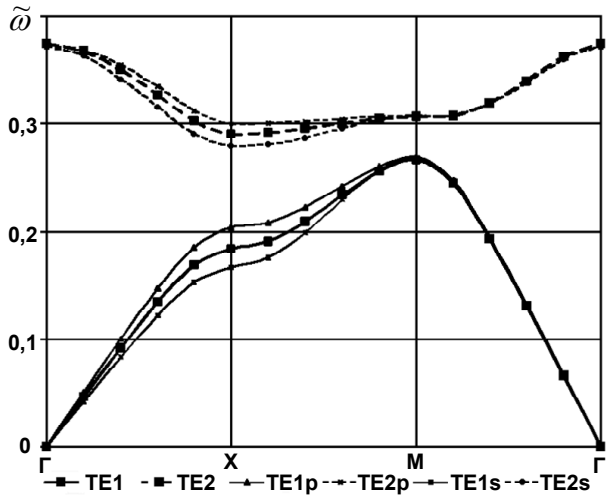

Fig.13. TE dispersion curves for complex deformation

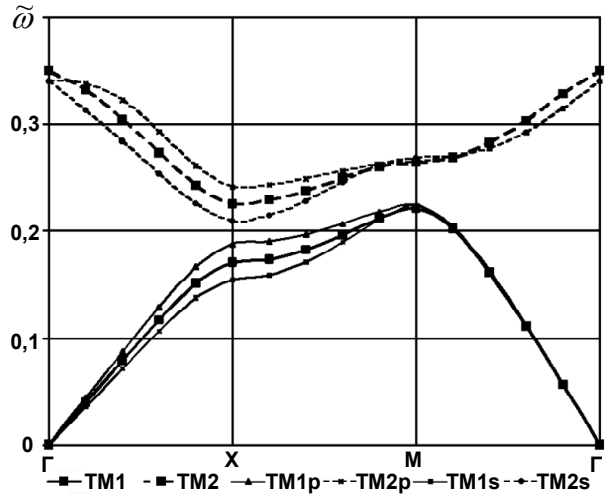

Fig.14. TM dispersion curves for complex deformation

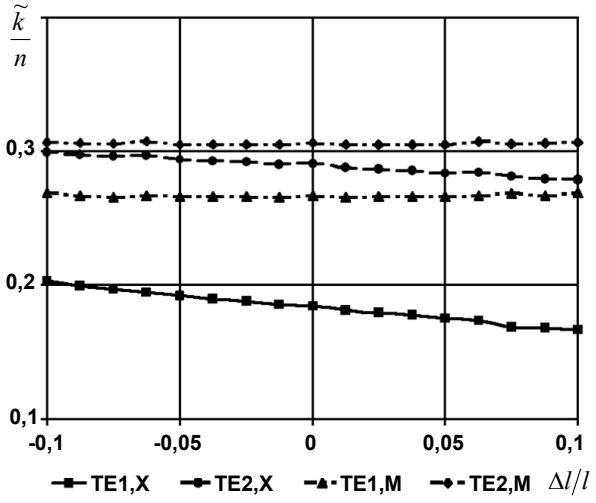

Fig.15. TE reciprocal refraction vs. complex deformation

Fig.16 illustrates the reciprocal effective refraction for the TM modes. The slopes of reciprocal effective refraction curves are not zero only for TM1 and TM2 modes in the *X* direction and equal.

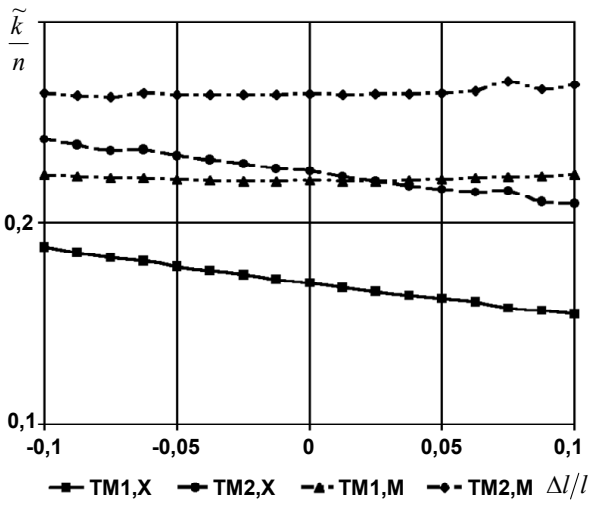

Fig.16. TM reciprocal refraction vs. complex deformation

Let's now analyze the results obtained for all cases of static deformation together. For this purpose we need to calculate the variation of the reciprocal effective refraction $\Delta\frac{1}{n}$ as the effect of deformations. The curves of $\Delta\frac{1}{n}$ dependences for the TM modes are shown in Fig.17.

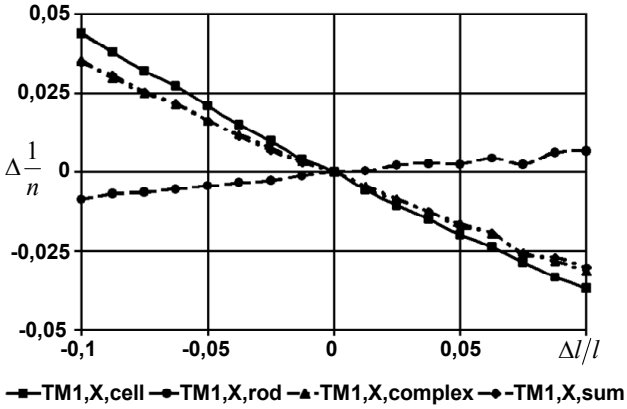

Fig.17. Photoelastic effect analysis for TM1 mode

The indexes denote *cell*, *rod* and *complex* deformation. Besides that, the curve represented on the graph with the index *sum* was obtained in the following way:

$$\Delta\frac{1}{n}(sum) = \Delta\frac{1}{n}(cell) + \Delta\frac{1}{n}(rod)$$

The interesting fact is that this curve gives the same dependence of reciprocal effective refraction variation as the curve obtained directly by complex deformation calculations.

As a result, it is possible to discuss different static deformations separately for the complex structures. To obtain common dependences it is enough to add algebraically partial deformation cases. For the other modes and directions the dependences are similar.

Periodical deformations. Consider the following photonic crystal deformation model. In an undisturbed state the photonic crystal is an isotropic structure in the *xy* plane. The photonic lattice step is *a*. Let's disturb this photonic structure by the bulk plane acoustic wave. The shortest wavelength of interest to us is $\lambda = 2a$. Schematically deformation is shown in Fig.18. In this model the wave is not moving and the wave's minimum and maximum are strongly centered at the rods.

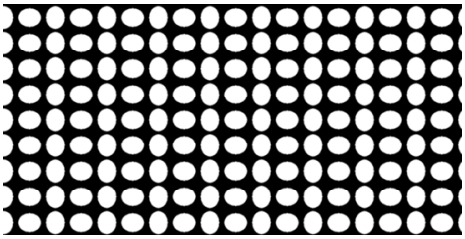

Fig.18. Periodical deformation model, λ=2a

The dispersion curves for this case are shown in the Fig.19. The mode degeneration is visible even for the very small perturbations (approx. 10^{-4}).

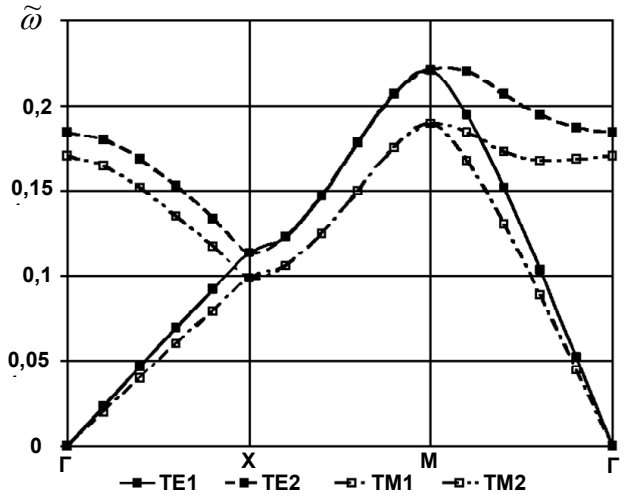

Fig.19. Dispersion curves, λ=2a

The next interesting case is when $\lambda = 4a$. Schematically such deformation is shown in Fig.20.

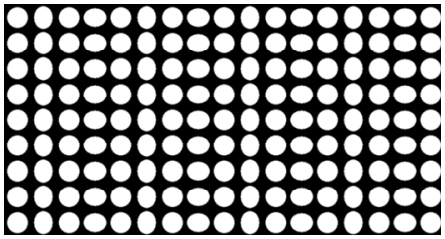

Fig.20. Periodical deformation model, λ=4a

The dispersion curves are shown in the Fig.21. The mode degeneration is sharper for this case.

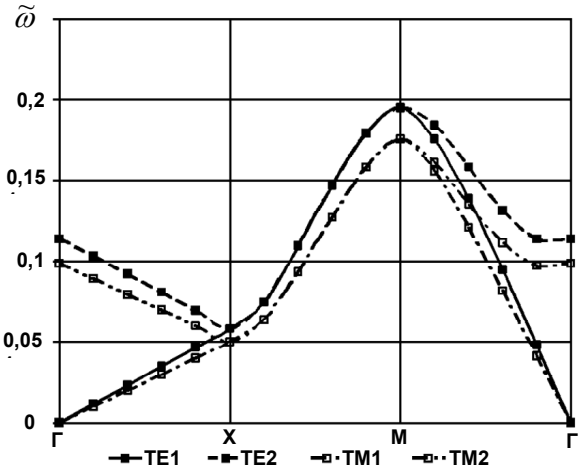

Fig.21. Dispersion curves, λ=4a

The field distributions are shown in Fig.22. The pictures obtained show that the TE1 and TE2 (or TM1 and TM2) modes differ in phase only.

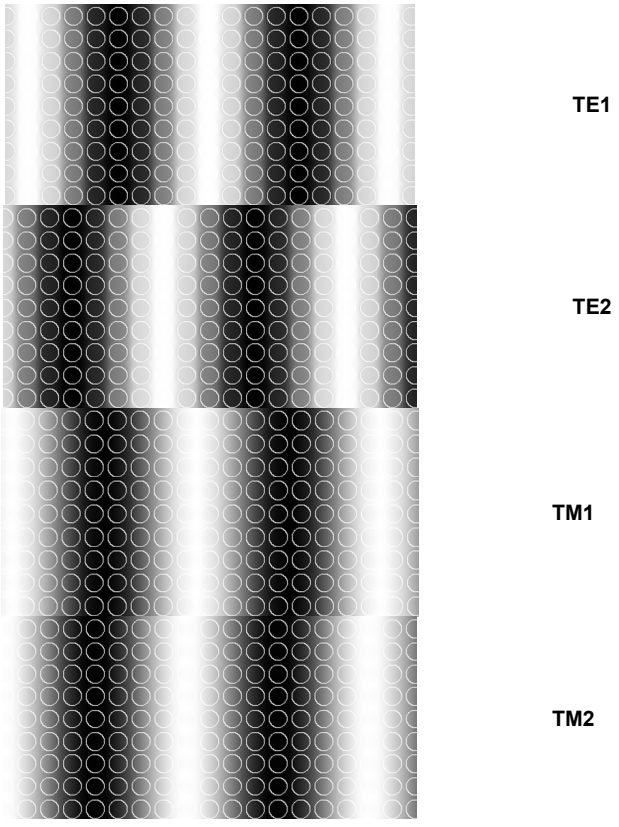

Fig.22. Field distribution for the degenerated modes

So even by the very small power acoustic wave with the multiple to photonic lattice step wavelength it is possible to destroy photonic bandgap structure at all. This phenomenon is widely used now in 1D photonic structures for light propagation control in fiber networks (so called add-drop filters) [3]. Here we have shown the same effect in a 2D square lattice photonic crystal.

Conclusions. We have computed the band structures of 2D square photonic crystals of silicon matrix and cylindrical air columns. We discussed three different cases of static deformations and calculated each of their contribution to the common deformation interaction with the photonic structure. The reciprocal effective refraction $\Delta 1/n$ of the deformed photonic crystal was calculated. We obtained that the refraction modification is strongly influenced by changes in lattice periodicity and by the deformation induced distortion of interfaces between inclusions and matrix. We defined photonic photoelastic effect. The possibility to calculate refraction variations separately and to add them algebraically in case of complex (periodicity and interfaces) deformations was shown by the numerical modeling for square lattice photonic crystals. Periodical deformations were considered in case of lattice and perturbation wave multiplicity only ($\lambda = n \cdot a$, n – multiplicity factor). For periodical deformations the mode degeneration was observed. Our results are expected to serve as practical guidance for tuning photonic properties (e.g. photonic photoelastic effect or bandgap structure) by applying mechanical strain.

1. Balakshy V. I., Parygin V. N., and Chirkov L. E. Physical Principles of Acousto-Optics – Radio and Communication, Moscow, 1985. 2. Danner Aaron J. An introduction to the plane wave expansion method for calculating photonic crystal band diagrams // University of Illinois at Urbana-Champaign, Last edited on June 4, 2005. 3. Díez A., Delgado-Pinar M., Mora J., Cruz J. L. and Andrés M. V. Dynamic Fiber-Optic Add–Drop Multiplexer Using Bragg Gratings and Acousto-Optic-Induced Coupling // IEEE PHOTONICS TECHNOLOGY LETTERS – 2003. – 15. 4. Joannopoulos John D. Photonic Crystals: Molding the Flow of Light. – Princeton University Press, 2008. 5. Jun Sukky and Cho Young-Sam Deformation-induced bandgap tuning of 2D silicon-based photonic crystals // OPTICS EXPRESS – 2003. – 11. 6. Lourtioz Jean-Michel Photonic Crystals. Towards Nanoscale Photonic Devices. – Springer, 2008. 7. Magdich L. N. and Molchanov V. Ya., Acousto-Optic Devices and Their Applications – Gordon and Breach, New York, 1989. 8. Pyatakova Z. A. Acoustooptic Bragg Diffraction in 2-Dimensional Photonic Crystals // M.V. Lomonosov Moscow State University, Physics Department. 9. Saado Y., Golosovsky M., Davidov D., and Frenkel A. Tunable photonic band gap in self-assembled clusters of floating magnetic particles // Phys. Rev. B – 2002. – 66. 10. Sakoda K. Optical Properties of Photonic Crystals. – Springer, 2001. 11. Shimoda Y., Ozaki M., and Yoshino K. Electric field tuning of a stop band in a reflection spectrum of synthetic opal infiltrated with nematic liquid crystal // Appl. Phys. Lett. – 2001. – 79. 12. Yariv A.and Yeh P. Optical Waves in Crystals – John Wiley & Sons, 1984. 13. Yoshino K., Shimoda Y., Kawagishi Y., Nakayama K., and Ozaki M. Temperature tuning of the stop band in transmission spectra of liquid-crystal infiltrated synthetic opal as tunable photonic crystal // Appl. Phys. Lett. – 1999. – 75. 14. Zhou J., Sun C.Q., Pita K., Lam Y.L., Zhou Y., Ng S.L., Kam C.H., Li L.T., and Gui Z.L. Thermally tuning of the photonic band gap of SiO2 colloid-crystal infilled with ferroelectric BaTiO3 // Appl. Phys. Lett. – 2001. – 78.

Submitted 19.06.09

UDC 537.6/.8

O. Prokopenko, Ph.D., R. Verba, M.Stud.

INFLUENCE OF SIGNAL TIME DELAY ON MAGNETIZATION DYNAMICS OF TWO COUPLED SPIN-TORQUE NANO-OSCILLATORS

The possibility of existence of synchronous magnetization auto-oscillations in an array of interacting spin-torque nanooscillators (STNO) is considered. The influence of signal time delay on the synchronization of coupled STNOs is investigated. The semi-analytical method for evaluation of synchronous generation characteristics has been developed in the case of substantially non-isochronous auto-oscillators. The dependencies of phase-locking bandwidth on system parameters were obtained and analyzed in the case of two coupled STNOs.

Key words: spin-torque nano-oscillator, signal time delay, phase-locking bandwidth, non-isochronous spin-wave auto-oscillator.

Розглянута можливість встановлення режиму синхронних автоколивань намагніченості у системі взаємодіючих магнітних наноконтактів (МНК). Досліджено вплив величини часу запізнення сигналу на синхронізацію МНК. Розроблений напіваналітичний метод розрахунку параметрів синхронної генерації для сильно неізохронних автогенераторів. Для моделі двох взаємодіючих МНК отримані залежності ширини смуги синхронізації від параметрів системи.

Ключові слова: магнітний наноконтакт, час запізнення сигналу, смуга синхронізації, неізохроонний спін-хвильовий автогенератор.

Introduction. One of the perspective tendencies of micro- and nanoelectronics evolution is the spin-wave nanoelectronics [4–7; 10; 12–17; 19–22]. Nowadays the element base of this branch is being quickly developed. Most of presently used spin-wave devises are created using thin ferromagnetic films (for instance, yttrium-iron garnet films [3; 21]) and intended for the realization of nonlinear interaction between two or more microwave signals [3; 11; 21; 27; 35]. But today there are no generators and amplifiers of spin waves with acceptable scale and parameters for the electronics of future [23; 28]. This problem can be solved by using the spin-torque nano-oscillators and/or the systems based on them [4–7; 12; 15–17; 19; 22–23].

It was theoretically predicted by J.C. Slonczewski [32–33] and L. Berger [10] and then experimentally observed by many authors [15–17; 34] that direct current traversing the layered magnetic structure can excite a microwave magnetization precession in the structure. This structure, known as a spin-torque nano-oscillator (STNO), typically consists of several magnetic layers divided by a thin non-magnetic dielectric or metal spacers (Fig. 1). One of the layers is a thick "fixed" layer (bottom layer in Fig. 1). In this layer the magnetization vector $\mathbf{M}_{FXL}$ has only single (fixed) direction defined by an external magnetic field $\mathbf{H}_{ext}$, applied to the structure, geometry of the structure, magnetic anisotropy, etc. The other magnetic layers known as "free" layers are thinner. In the following, for the simplicity, we consider a three-layer STNO with only one "free" layer (top layer in Fig. 1). In "free" layer the magnetization vector $\mathbf{M}_0$ has no fixed direction for the applied external magnetic field $\mathbf{H}_{ext}$.

In such structure direct bias electron current I_{dc} passing through it from the "fixed" layer to the "free" layer will become a spin-polarized current. We can imagine this spin-polarized current as a stream of charged particles (electrons) with the spins directed close to the direction of the magnetization vector $\mathbf{M}_{FXL}$ in a "fixed" layer of the structure. Due to this specialty the spin-polarized current can transfer the spin-torque in a "free" magnetic layer that results to the excitation of a microwave magnetization precession in the layer. If the amplitude I_{dc} of direct bias current exceeds the current threshold I_{th}, the spin transfer torque force, caused by direct current, in the "free" layer of

a STNO can compensate the natural positive magnetic damping in this layer. In this case STNO successfully works as a microwave spin-wave auto-oscillator [29–31].

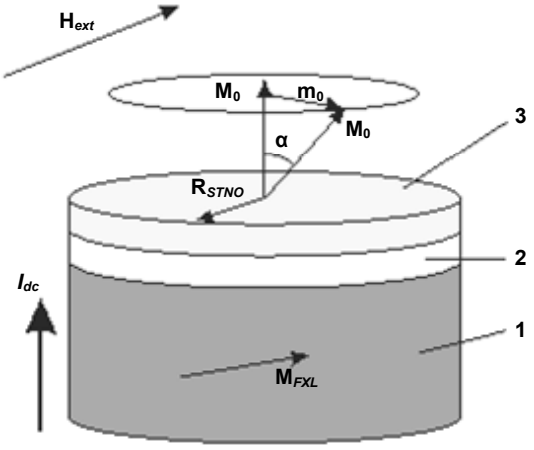

Fig. 1. The simplest model of spin-torque nano-oscillator (STNO) consists of three layers: "fixed" magnetic layer (1), thin non-magnetic spacer (2) and thin "free" magnetic layer (3). $\mathbf{M}_{FXL}$ is the magnetization vector in the "fixed" magnetic layer (1), defined by an external magnetic field $\mathbf{H}_{ext}$, geometry of the structure, etc. $\mathbf{M}_0$ is the magnetization vector in the "free" magnetic layer (3). If direct current I_{dc} passing the structure from "fixed" to "free" layer a microwave precession of magnetization with the magnetization vector $\mathbf{M}_0$ is excited; α is the precession angle and $\mathbf{m}_0$ is the excited microwave component of magnetization vector

The typical eigen frequency of STNO is 1 – 50 GHz [13–16], but there is theoretical prediction that it can be increased up to 200 GHz [14; 24–26]. Therefore the application of such devices is most convenient in the microwave band. The major advantages of the STNOs are its small sizes (the typical radius R of the structure is 10 – 200 nm, height of the structure h is 10 – 50 nm), compatibility of STNO fabrication technology with the standard micro- and nanoelectronics fabrication technology, the possibility of generation frequency tuning in a wide range [14–17; 25–26]. But the power of generated oscillation in a STNO is very low due to the very small oscillator sizes. The microwave power emitted from a typical STNO is 1 – 10 pW [15–17]. This power is too low for the major of microwave applications; the sufficient microwave power level for such applications is approximately 1 μW. Therefore the arrays of STNOs must be used for creation of various typical microwave devices on the analogy of creation of microwave devices with Josephson junctions [18].

The generation frequency of STNO is given by an expression [30]

$$\omega = \omega_0 + N\left(1 - \frac{\Gamma}{\sigma I_{dc}}\right), \qquad (1)$$

where N is the coefficient of nonlinear frequency shift, Γ is the natural positive damping, σ is the spin-polarized efficiency (the coefficient of spin-wave excitation efficiency), ω_0 is the characteristic eigen frequency:

$$\omega_0 = \sqrt{\left(\omega_H + \omega_M \alpha_{ex} k^2\right)} \times$$
$$\times \sqrt{\left(\omega_H + \omega_M \alpha_{ex} k^2 + \omega_M \cos^2\theta\right)}. \qquad (2)$$

There θ is the out-of-plane magnetization angle (angle between an external magnetic field $\mathbf{H}_{ext}$ and the plane of "free" magnetic layer), α_{ex} is the square of the exchange length. The wave number of the first excited spin-wave mode (the mode with the lowest excitation threshold current I_{th}) is $k \approx 1{,}2/R$, where R is the radius of STNO [28]. Thus, the generation frequency depends on the geometry of STNO. The existing its fabrication technology has high enough geometrical and electrophysical parameters spread [15–17; 23; 25–26], so each STNO would have intrinsic generation frequency, in general case, not equal to the frequency of another in the oscillators array. Thus, there is a problem of existence of quasi-harmonic generation in the STNO array on the assumption of existence of its parameters spread. The generation frequency spread for the STNOs with typical parameters in array [28–30] is about

$$\frac{\triangle\omega}{<\omega>} \sim \frac{\alpha_{ex}}{R^2}\frac{\triangle R}{<R>} \sim 5 \div 15\%. \qquad (3)$$

The synchronization state of two coupled STNOs was observed experimentally [15]. But the experimental way to find the optimal parameters, required for the creation of spin-wave auto-oscillators, is ineffective due to the difficulties of samples fabrication. The synchronization phenomenon was investigated in details in the case of weakly coupled isochronous auto-oscillators [9, 20]. The case of two substantially non-isochronous STNOs is analyzed in the paper [28–31] in the frame of the model with zero signal time delay. In this case the obtained normalized phase-locking bandwidth (PLBW) is $\triangle\omega/\omega < 1\%$ that is not enough for the practical applications. Because of this circumstance this paper is devoted to the investigations of signal time delay influence on the mutual phase-locking (PL) of two coupled STNOs.

Numerical simulation of the dynamics in the system of two coupled STNOs. The microwave dynamics of magnetization in STNO can be described by the equation [28–31]:

$$\frac{db}{dt} + i\left(\omega_0 + N|b|^2\right)b + \Gamma b - \sigma I_{dc}\left(1 - |b|^2\right)b = \Lambda, \qquad (4)$$

where b is normalized circular component of magnetization, that is perpendicular to the equilibrium magnetization vector, Λ is the normalized external signal. In our case Λ is the signal of second oscillator that is coupled to the first one. The coupling between the STNOs, realized by the interaction of spin waves, excited by the one oscillator with the second one, plays the dominant role, as it was shown in paper [29]. In this case the normalized external signal can be written in the form:

$$\Lambda = \sum_{k \neq j} \Omega_{jk} e^{i\beta_{jk}} b_k, \qquad (5)$$

where Ω_{jk} is the coupling frequency for j-th and k-th oscillators, $\beta_{jn} = -k_n a_{jn}$ is the phase coefficient that allow us to take into account the signal time delay (the finite velocity of coupling signal propagation), a_{jn} is the distance between the centers of j-th and n-th oscillators, and k_n is the wave number of spin wave, excited by the n-th oscillator. In the most typical case the coupling frequency is given by an expression [29]:

$$\Omega_{jk} = \frac{\Gamma}{\sqrt{2k_k a_{jk}}} \exp\left(-\frac{\Gamma a_{jk}}{v_{gr}}\right), \qquad (6)$$

where v_{gr} is the group velocity of spin waves.

One can see that the coupling amplitude is quickly decreased with increasing of distance a_{jk}, therefore the influence of the oscillator neighbors (other STNOs) plays the dominant role. In that case the adequate and simplest model is the model of two coupled oscillators [28]. We shall use this model further.

The chosen model allows us to pass from the problem with random coefficients to the problem with determined coefficients. In this case PLBW is the area of possible eigen frequency of one STNO while the PL regime exist for the any fixed frequency of other oscillator. For simplicity we shall consider further the case of almost identical STNOs. Thus, the coupling coefficients, dc currents and spin-wave excitation efficiency are equal for two oscillators. This simplification can be made because the existence of technological parameters spread in this case will not lead to the significant changes of the system dynamics [36]. In order to further simplify the problem let the phase coefficients be equal, because the stationary states are invariant relative to substitution $\beta'_{12}+\beta'_{21}=\beta_{12}+\beta_{21}$ (see. Ex. (7)). Thus, the system of equations can be presented in the final form:

$$\frac{db_1}{dt}+\mathrm{i}\left(\omega_{01}+N\left|b_1\right|^2\right)b_1+\Gamma b_1-\sigma I_{dc}\left(1-\left|b_1\right|^2\right)b_1=\Omega e^{i\beta}b_2,$$

$$\frac{db_2}{dt}+\mathrm{i}\left(\omega_{02}+N\left|b_2\right|^2\right)b_2+\Gamma b_2-\sigma I_{dc}\left(1-\left|b_2\right|^2\right)b_2=$$

$$=\Omega e^{i\beta}b_1. \qquad (7)$$

There is no precise analytical solution of system (7). Therefore we have made the numerical analysis of system (7) for the case of STNOs with small deviation of eigen frequencies: $\left|\omega_{01}-\omega_{02}\right|/N=5\%$. The dependency of generation frequencies of two coupled STNOs on the normalized phase shift β/π is shown in Fig. 2. The generation frequencies were found as the frequencies that correspond to the amplitude maxima, obtained after the Fourier transformation of numerical solution of system (7). One can see that the main frequencies in the signal spectra for two coupled oscillators are equal for some range of phase shifts β.

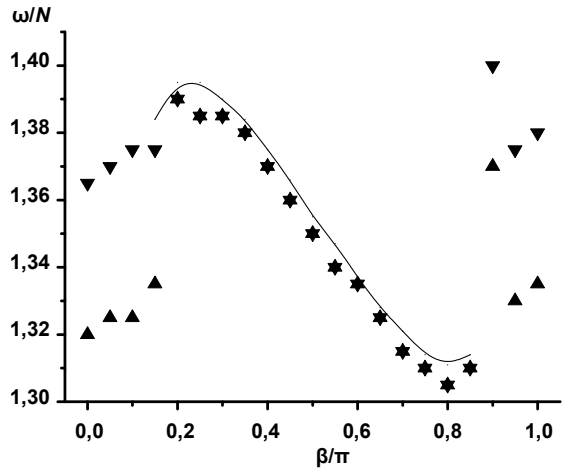

Fig. 2. The dependency of generation frequencies of two coupled spin-torque nano-oscillators (STNOs) on the normalized phase shift β/π. The points are the numerical solution of system (7). The symbol ▲ correspond to the frequency of one STNO and the symbol ▼ correspond to the frequency of the other oscillator. The normalized eigen frequency of first oscillator is $\omega_{01}/N=1$ and the normalized eigen frequency of second oscillator is $\omega_{02}/N=1{,}05$ Solid line is the curve of generation frequency for the synchronous regime (analytical solution). $\Omega=0{,}1\Gamma$, $N/\Gamma=100$, $\sigma I_{dc}/\Gamma=1{,}5$

However, the agreement of generation frequencies is not necessarily correspond to the synchronous generation in the nonlinear systems of several oscillators. In this case the possibility of oscillator signals interference must be checked [1–2; 15; 20]. In our case this should lead to the estimation of visibility function:

$$V(\tau)=\lim_{T\gg 1/\omega}\frac{1}{T}\int_0^T\left|\frac{b_1(t)}{B_1}+\frac{b_2(t+\tau)}{B_2}\right|^2 dt, \qquad (8)$$

where B_j is the amplitude of j-th solution. The integral (8) must be taken for the time area with stationary regime of operations. The visibility function (8) is changed in the range $[0;4]$ for the synchronous oscillations. The range of possible visibility function values is shrunk with the decrease of the level of oscillations synchronism. The quantitative parameter of oscillations synchronism may be chosen as the duration s of synchronous generation pulses [2; 20]. Using this approach we can evaluate the approximate value of visibility function in the case $s\to 0$ (non-synchronous generation): $V(\tau)\xrightarrow[s\to 0]{}2\notin f(\tau)$. Checking the obtained numerical solution of the system (7) using the described method of visibility function, we made sure that the PL is occur for the range of phase shift $\beta\in[0.2\pi;0.85\pi]$ (see Fig. 2). For the corresponded range of signal time delay (i.e. distances between the oscillators for the fixed v_{gr}) the synchronous generation of two coupled STNOs occurs.

Analytical theory. One of the most important characteristics valuable for real practical applications of phase-locked oscillators are the form of PL curve and the PLBW. The numerical investigation of these characteristics is cumbersome and complicated enough task. But in many cases there is no need to know these parameters precisely. Taking this into account we developed a simple approximate theory which allows us to determine these parameters with high enough precision.

By varying the out-of-plane magnetization angle the properties of STNOs substantially changes: from the case of isochronous oscillator to the case of strongly non-isochronous oscillator [5]. In the case of one-way influence PLBW increases with increasing of the nonlinear frequency shift coefficient N [5]. Therefore it is reasonable to consider the system with very large value of this coefficient. The maximal value of N is comparable to the values of eigen frequencies, so we can suppose further:

$$N\sim\omega_0\gg\Gamma>\Omega. \qquad (9)$$

Let's consider the general case of the system of M linear coupled non-isochronous oscillators. It is described by the system of equations:

$$\frac{db_j}{dt}+i\omega_j\left(\left|b_j\right|^2\right)b_j+\Gamma_{eff,j}\left(\left|b_j\right|^2\right)b_j=\sum_{k\neq j}\Omega_{jk}e^{i\beta_{jk}}b_k, \qquad (10)$$

where Γ_{eff} is the total effective damping, that in case of STNO consists from the natural positive damping and from the effective negative damping created by spin-polarized current. There is no general solution of such system. Therefore we shall solve the system using "inverse algorithm". We substitute the "optimal known solution" to the system (10). In our case this solution is the harmonic synchronous oscillations:

$$b_j(t)=B_j e^{-i(\omega t+\psi_j)}. \qquad (11)$$

By substitution of Ex. (11) to Ex. (10) we can determine the amplitudes and phases. If obtained phases are real and amplitudes are real and positive then the found solution characterize some stationary state. This state must also be

stable with respect to the small perturbation. Only in this case it exists long enough to be detected on the experiment. If there are no solutions that satisfy all the criteria then there is no synchronous generation in the system of two coupled oscillators.

Thus, after substituting Ex. (11) to the system (10) we have obtained:

$$\Gamma_{eff,j} B_j = \sum_{k \neq j} \Omega_{jk} B_k \cos(\psi_{jk} + \beta_{jk}), \qquad (12a)$$

$$\left[\omega - \omega_j\right] B_j = -\sum_{k \neq j} \Omega_{jk} B_k \sin(\psi_{jk} + \beta_{jk}), \qquad (12b)$$

where $\psi_{jk} = \psi_j - \psi_k$. If conditions (9) are fulfilled, the left part of Ex. (12b) is substantially greater than the right one, both parts of the Ex. (12a) has the same order of magnitude. It is natural to solve the system (12) by the method of successive approximations. The zero-level approximation is chosen as the amplitude B_{0j}, satisfying the equation $\omega - \omega_j\left(B_{0j}^2\right) = 0$. Writing the solution in the form $B_j = B_{0j} + \xi_j$, at the next level of approximation we obtained:

$$\Gamma_{eff,j}(B_{0j}^2) B_{0j} = \sum_{k \neq j} \Omega_{jk} B_{0k} \cos(\psi_{jk} + \beta_{jk}), \qquad (13a)$$

$$2N_j B_{0j} \xi_j = \sum_{k \neq j} \Omega_{jk} B_{0k} \sin(\psi_{jk} + \beta_{jk}), \qquad (13b)$$

where introduced $d\omega_j / d\left(B_j^2\right)\Big|_{B_{0j}} = N_j$. As one can see, the input system (12) divides into two subsystems. The first subsystem (13a) defines the generation frequency (B_{0j} indirectly depends on this frequency) and phase shift between the oscillators. The second subsystem (13b) defines the amplitude corrections. These corrections are small in the case of Ex. (9) fulfillment, so we shall neglect them.

Thus, the input system of M nonlinear complex differential equations is transformed to the system of M real algebraic equations. Using Ex. (10) it is possible to obtain the system of $2M-1$ equations defines the perturbation dynamics of the solution:

$$\frac{d}{dt}\begin{pmatrix} \delta\xi_j \\ \delta\psi_{jk} \end{pmatrix} = \mathbf{M}\begin{pmatrix} \delta\xi_j \\ \delta\psi_{jk} \end{pmatrix}. \qquad (14)$$

The stability analysis of the solution was performed using analysis of characteristic matrix **M** by Raus-Gurvits' criteria [1; 8].

In general case this approach is valid if the following conditions are fulfilled:

$$\omega_j\left(b_j^{'}\right) - \omega_j(0) \gg \Omega, \ \omega_j\left(b_j^{'}\right) \gg \Gamma, \qquad (15)$$

where $b_j^{'}$ is the generation amplitude of a lone oscillator (conditions (9) are the partial case of conditions (15)).

Main results and discussion. The Ex. (13a) allows us to write the equation for the generation frequency:

$$A_1^2 + A_2^2 - 2A_1A_2\cos(2\beta) = \sin^2(2\beta), \qquad (16)$$

where $A_j = \dfrac{\Gamma_{eff,j} B_{0j}}{\Omega_{jk} B_{0k}} = \dfrac{\left(\Gamma - \sigma I_j\left[1 - \dfrac{\omega - \omega_j}{N}\right]\right)\sqrt{\omega - \omega_{0j}}}{\Omega_{jk}\sqrt{\omega - \omega_{0k}}}$.

In fact, the Eq. (16) is the polynomial equation of fourth order; there are known analytical solutions for this equation.

The normalized frequency curve, estimated by using the solution of Eq. (16) is shown in Fig. 2 (solid line). The insignificant difference between the analytical solution and numerical data can be explained by neglecting of first order correction for the frequency (this correction is proportional to ΩB_0).

The dependence of half PLBW (the maximal difference $\left|\omega_{01} - \omega_{02}\right|$ when the synchronous regime exists) on phase shift β is shown in Fig. 3. All parameters of the oscillators except the eigen frequencies are the same, and the PLBW is practically independent on average frequency, therefore the PLBW curve is the symmetric curve. In the case $N \gg \Omega, \Gamma$ the PLBW is proportional to the coefficient of nonlinear frequency shift N. This coefficient is the commensurable to the generation frequency, so for finite non-zero phase shifts β it is possible to achieve the synchronous generation in the system with high spread of eigen frequencies (5 – 10%). Thus, the performed analysis have shown a possibility of creation of practical spin-wave generators constructions with several (at least two) STNOs.

The maximal value of phase-locking bandwidth is observed at phase shift $\beta = \pi/2 + \pi n$, where $n \in \mathbb{Z}$. This result is substantially different than in the case of isochronous oscillators [9] (the optimal phase shift for the isochronous oscillators is $\beta = \pi n$). This difference can be explained by the different mechanisms of synchronization.

The influence of one isochronous oscillator on the frequency of another isochronous oscillator can be written in the form (see. Eq. (12b)):

$$\Delta\omega_{int} = -\Omega_{jk} B_k \sin(\psi_{jk} + \beta). \qquad (17)$$

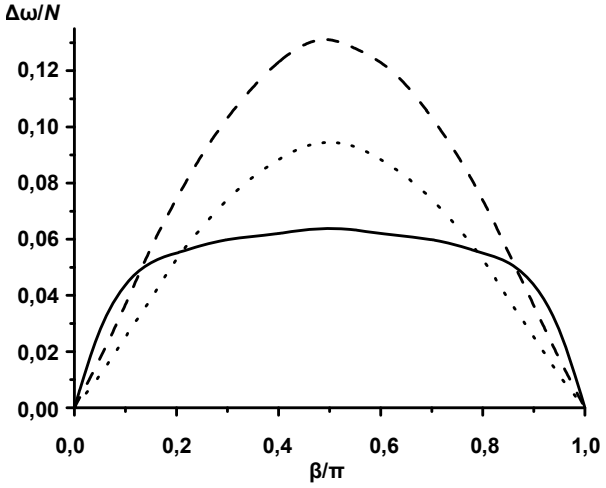

Fig. 3 The dependence of half phase-locking bandwidth on the normalized phase shift β/π for different currents I_{dc}. Solid line – $\sigma I_{dc}/\Gamma = 1{,}1$, dashed line – $\sigma I_{dc}/\Gamma = 1{,}5$, dotted line – $\sigma I_{dc}/\Gamma = 2$. $\Omega = 0.1\Gamma$, $N/\Gamma = 100$, $\omega_{01}/N = 1$

The optimal case for two STNOs with almost equal amplitudes of generated signal and symmetric coupling is the case of symmetrical resonance detuning of the oscillators. It means that the synchronized state of first oscillator with the coupling signal generated by the second oscillator fade at some distance between the oscillators. This distance is the same for the first and second oscillators. Thus, the influence of the oscillator with higher eigen frequency must lead to the increase of eigen frequency (that is initially lower) of neighboring oscillator and vice versa; the absolute values of eigen frequency shift must be almost equal. As one can see from Ex. (17), these conditions are fulfilled if $\beta = \pi n$, because $\psi_{jk} = -\psi_{kj}$.

But for non-isochronous oscillators there is other possible way to change the generation frequency of other oscillators. The frequency of non-isochronous oscillator depends on its amplitude. Therefore, the indirect influence

can exist. If one of two coupled STNOs change the oscillation amplitude of other STNO it also leads to the change of frequency of other STNO. This indirect influence can be approximately evaluated as (see Ex. (12)):

$$\Delta\omega_{int} \sim \frac{2NB_j\Omega_{jk}B_k}{\Gamma_{eff,j}}\cos(\psi_{jk}+\beta). \qquad (18)$$

The changes of angular frequency of generated signal in this case are substantially greater than in the case of isochronous oscillator and realized optimally at $\beta = \pi/2 + \pi n$. In order to examine the first or second possible mechanism of frequency shift takes place, the amplitudes of signals generated by the STNOs were determined. Using these amplitude values the resonance frequencies were estimated using equation of non-isochronism (Fig. 4).

One can see that the resonance frequencies of two coupled STNOs are very close each to another in the regime of synchronous generation. Thus, in the case of non-isochronous STNOs the phase-locking regime occurs due to the indirect influence (via amplitude) of one oscillator on the other oscillator. This influence leads to the change of oscillation amplitudes and then to the change of resonance frequencies of the oscillators.

The linear dependence of half PLBW on N can be easily explained by Ex. (18). This linear dependence exists until two synchronization mechanisms lead to the same effect, i.e. while $N > \Gamma$. Due to Ex. (17), (18) the PLBW must also linear depend on coupling coefficient Ω; this conclusion was confirmed by the results of numerical estimations. The dependence of PLBW on dc current is non-monotonic and has a maximum at $\sigma I_{dc}/\Gamma = 1{,}2 \div 1{,}3$ (see. Fig. 3). It can be explained by the concurrence of two mechanisms. From one point of view the amplitude of oscillations of neighboring STNO increases (due to the interaction between the oscillators) while the pumping dc current I_{dc} passed through other STNO increases. This leads to the expansion of PLBW. From other point of view the increase of pumping dc current I_{dc} leads to the increase of microwave power emitted by the oscillator and therefore to the shrink of PLBW for two coupled STNOs [5].

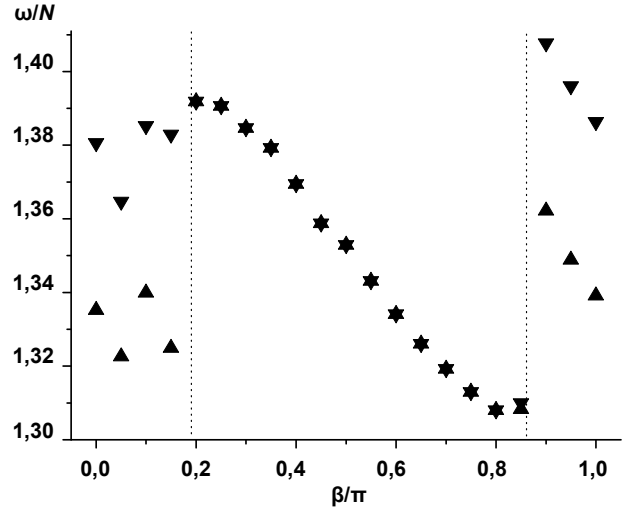

Fig. 4 The dependence of normalized resonance frequencies of two coupled STNOs on the normalized phase shift. The symbols ▲ and ▼ correspond to the resonance frequencies (obtained by numerical estimation) of one and other oscillator, respectively. Dash lines divide the figure area on the three areas and the second area is the area where the mutual phase synchronization of the STNOs exists. For the description of all parameters of analyzed system see Fig. 2

Conclusion. The magnetization dynamics of two coupled spin-torque nano-oscillators substantially depends on the time delay of coupling signal. The synchronized state of two oscillators exists for some range of possible phase shift, i.e. for some range of time delays. While the optimal phase shift for isochronous oscillators is $\beta = \pi n$, the optimal phase shift for two coupled STNOs is $\beta = \pi/2 + \pi n$, where $n \in \mathbb{Z}$. The general mechanism of phase-locking in the system of two coupled STNOs is based on the change of oscillation amplitude of one oscillator by the other one, that due to the non-isochronism of the oscillators leads to the change of oscillator frequencies and vice versa.

This work was supported by grant M/175-2007 of Ministry of Education and Science of Ukraine.

1. Анісімов І.О. Коливання та хвилі. – К., 2003. 2. Анищенко В.С., Астахов В.В., Вадивасова Т.Е., Стрелкова Г.И. Синхронизация регулярных, хаотических и стохастических колебаний. – М., 2008. 3. Гуревич А.Г., Мелков Г.А. Магнитные колебания и волны. – М., 1994. 4. Мелков Г., Прокопенко О. Умови надвисокочастотної синхронізації для магнітних наноконтактів, розташованих у шарі магнітовпорядкованої речовини // Вісник Київського національного університету імені Тараса Шевченка. Серія: радіофізика та електроніка. – 2007. – № 10. 5. Прокопенко О.В., Верба Р.В., Борисенко М.О. Вузькосмуговий режим вимушеної фазової синхронізації магнітних наноконтактів // Вісник Київського національного університету імені Тараса Шевченка. Серія: фізико-математичні науки. – 2008. – № 3. 6. Прокопенко А.В., Мелков Г.А. Угловая зависимость порогового тока генерации в магнитном наноконтакте // Сборник тезисов VIII Международного украинско-российского семинара "Нанофизика и Наноэлектроника", Киев, Украина, 2007. 7. Прокопенко О.В., Мелков Г.А. Нелінійні властивості систем з магнітними наноконтактами // Тези конференції "Наноrозмірні системи: будова-властивості-технології" (НАНСИС 2007), Київ, Україна, 2007. 8. Рабинович М.И., Трубецков Д.И. Введение в теорию колебаний и волн: Учебное пособие. – М., 1984. 9. Романовский Ю.М., Степанова Н.В., Чернавский Д.С. Математическая биофизика. – М., 1984. 10. Berger L. Emission of spin waves by a magnetic multilayer traversed by a current // Physical Review B. – 1996. – Vol. 54. 11. Chumak A.V., Serga A.A., Hillebrands B., Melkov G.A., Tiberkevich V., Slavin A.N. Parametrically stimulated recovery of a microwave signal using standing spin-wave modes of a magnetic film // Physical Review B. – 2009. – Vol. 79. 12. Gerhart G., Bankowski H., Tiberkevich V., Slavin A., Melkov G. Angular dependence of the microwave generation threshold in a nanoscale spin-torque oscillator // Physical Review B. – 2007. – Vol. 76. 13. Heide C. Spin Currents in Magnetic Films // Physical Review Letters. – 2001. – Vol. 87. 14. Hoefer M.A., Ablowitz M.J., Ilan B., Pufall M.R., Silva T.J. Theory of Magnetodynamics Induced by Spin Torque in Perpendicularly Magnetized Thin Films // Physical Review Letters. – 2005. – Vol. 95. 15. Kaka S., Pufall M.R., Rippard W.H., Silva T.J., Russek S.E., Katine J.A. Mutual phase-locking of microwave spin torque nano-oscillators // Nature. – 2005. – Vol. 437. 16. Kiselev S.I., Sankey J.C., Krivorotov I.N., Emley N.C., Schoelkopf R.J., Buhrman R.A., Ralph D.C. Microwave oscillations of a nanomagnet driven by a spin polarized current // Nature. – 2003. – Vol. 425. 17. Krivorotov I.N., Emley N.C., Sankey J.C., Kiselev S.I., Ralph D.C., Buhrman R.A. Time-domain measurements of nanomagnet dynamics driven by spin-transfer torques // Science. – 2005. – Vol. 307. 18. Likharev K.K. Dynamics of Josephson Junctions and Circuits. – N.-Y., 1986. 19. Nanoelectronics, nanophotonics, and nanomagnetics // Report of the National Nanotechnology Initiative Workshop, 2004, web-link: *www.nano.gov/NNI_EPM.pdf. 20.* Pikovsky A., Rosenblum M., Kurths J. Synchronization: a universal concept in nonlinear sciences. – Cambridge, 2007. 21. Prinz G.A. Magnetoelectronics // Science. – 1998. – Vol. 282. 22. Prokopenko O., Tyberkevych V., Slavin A. Mutual phase-locking of two spin-torque oscillators: Influence of time delay of a coupling signal // Proceedings of the Europe International Magnetics Conference (Intermag 2008), Madrid, Spain, 2008. 23. Ralph D.C., Stiles M.D. Spin Transfer Torques // Journal of Magnetism and Magnetic Materials. – 2008. – Vol. 320. 24. Rezende S.M., de Aguiar F.M., Azevedo A. Spin-Wave Theory for the Dynamics Induced by Direct Currents in Magnetic Multilayers // Physical Review Letters. – 2005. – Vol. 94. 25. Rippard W.H., Pufall M.R., Silva T.J. Quantitative studies of spin-momentum-transfer-induced excitations in Co/Cu multilayer films using point-contact spectroscopy // Applied Physics Letters. – 2003. –Vol. 82, № 8. 26. Rippard W.H., Pufall M.R., Kaka S., Russek S.E., Silva T.J., Direct current induced dynamics in $Co_{90}Fe_{10}$ = $Ni_{80}Fe_{20}$ point contacts // Physical Review Letters. – 2004. – Vol. 92. 27. Schafer S., Chumak A.V., Serga A.A., Melkov G.A., Hillebrands B. Microwave spectral analysis by means of non-resonant parametric recovery of spin-waves signals in a thin magnetic film // Applied Physics Letters. – 2008. – Vol. 92. 28. Slavin A.N., Kabos P. Aproximate Theory of Microwave Generation in a Current-Driven Magnetic Nanocontact Magnetized in an Arbitrary Direction // IEEE Transaction on Magnetics. – 2005. – Vol. 41. 29. Slavin A.N., Tiberkevich V.S. Theory of mutual phase-locking of spin torque nano-oscillators // Physical Review B. – 2006. – Vol. 74. 30. Slavin A.N., Tiberkevich V.S. Nonlinear self-phase-locking effect in an array of current-driven magnetic nanocontacts // Physical Review B. – 2005. – Vol. 72. 31. Slavin A., Tiberkevich V. Nonlinear Auto-Oscillator

Theory of Microwave Generation by Spin-Polarized Current // IEEE Transaction on Magnetics. – 2009. – Vol. 45. 32. Slonczewski J.C. Conductance and exchange coupling of two feromagnets separated by a tunneling barrier // Physical Review B. – 1989. – Vol. 39, № 10. 33. Slonczewski J.C. Current-driven excitation of magnetic multilayers // Journal of Magnetism and Magnetic Materials. – 1996. – Vol. 159. 34. Tsoi M., Jansen A.G.M., Bass J., Chiang W.-C., Seck M., Tsoi V., Wider P. Excitation of a Magnetic Multilayer by an Electric Current // Physical Review Letters. – 1998. – Vol. 80. 35. Vasyuchka V.I., Melkov G.A., Moiseienko V.A., Prokopenko A.V., Slavin A.N. Correlation receiver of below-noise pulsed signals based on parametric interactions of spin waves in magnetic films // Journal of Magnetism and Magnetic Materials. – 2009. – Vol. 321, I. 20. 36. Verba R.V, Prokopenko O.V. Magnetization's dynamics of two coupled spin-torque nanooscillators // Proceedings of the V International Conference "Electronics and Applied Physics", Kyiv, Ukraine, 2009.

Submitted on 20.01.10

UDC 535.51

S. Savenkov, Ph.D., E. Oberemok, Ph.D.,
V. Nikonov, post grad. stud.

MUELLER MATRICES FOR LINEAR AND CIRCULAR DEGENERATE ANISOTROPY

The optical elements with linear and circular degenerate anisotropies have been examined in this article. The matrix model of these objects has been presented. The aspects of solving inverse problem on the basis of incomplete Muller matrices questions have been discussed. Examples of incomplete structures of Muller matrices are presented; they give full characterization of the optical elements which are characterized by linear and circular degenerate anisotropy.

Keywords: Mueller matrix, degenerate anisotropy, inverse problem.

В статті розглянуто загальну матричну модель для оптичних об'єктів з лінійною або круговою виродженою анізотропією. Наведено особливості розв'язку оберненої задачі на основі неповних матриць Мюллера. Представлено приклади неповних матриць Мюллера які повністю характеризують оптичні елементи з круговою або лінійною виродженою анізотропією.

Ключові слова: матриця Мюллера, вироджена анізотропія, обернена задача.

Introduction. The case of degenerate anisotropy is the case when eigenpolarizations and eigenvalues of medium coincide with each other. In most cases, the practically realizable examples of degenerate elements are based on ideal polarizers [2, 5] and are, hence, singular. However, as it has been recently pointed out in [3] a degenerate element can be nonsingular. Generalized matrix model of the medium characterized by degenerate anisotropy was derived in [4] Main goal of the present paper is to derive Mueller matrices for the media characterized by linear and circular degenerate anisotropy.

In general non-depolarizing optical element can be described by Jones matrices formalism:

$$\mathbf{T} = \begin{pmatrix} t_{11} & t_{12} \\ t_{21} & t_{22} \end{pmatrix} \tag{1}$$

and corresponding Muller matrices formalism

$$\mathbf{M} = \begin{pmatrix} m_{11} & m_{12} & m_{13} & m_{14} \\ m_{21} & m_{22} & m_{23} & m_{24} \\ m_{31} & m_{32} & m_{33} & m_{34} \\ m_{41} & m_{42} & m_{43} & m_{44} \end{pmatrix} \tag{2}$$

Correspondence between these formalisms for non-depolarizing optical element can be presented by Parke matrix equation:

$$\mathbf{M} = \mathbf{A} \times (\mathbf{T} \otimes \mathbf{T}^*) \times \mathbf{A}^{-1} \tag{3}$$

This equation results in definite inner structure of deterministic Mueller matrix. The knowledge of this structure allows defining the values of anisotropy parameters of medium basing on incomplete Mueller matrix. But, it is important to note, that the structure of incomplete Mueller matrix for solving of inverse problem varies considerably depending on type of anisotropy inherent to studied medium.

For the complete characterization of a medium it is convenient to use eigenvectors and eigenvalues of its Jones matrix. In general case arbitrary non-depolarizing medium possesses elliptical non-orthogonal eigenvectors. In the literature the conditions of orthogonality and degeneracy of eigenpolarizations were considered, see for example [4] and references herein. However, the conditions, under which a medium is characterized by degenerate linear or circular anisotropy, are not considered yet. In present paper the main goal is to derive explicit forms of Mueller matrices of media, which are characterized by degenerate anisotropy and have circular or linear eigenpolarizations.

General Jones matrices for linear and circular degenerate anisotropy. Analysis of the conditions on eigenpolarizations to be linear or circular for a medium with degenerate anisotropy will be carried out further in scope of the Jones matrix formalism.

All possible polarizations of light can be represented vie linear complex plane:

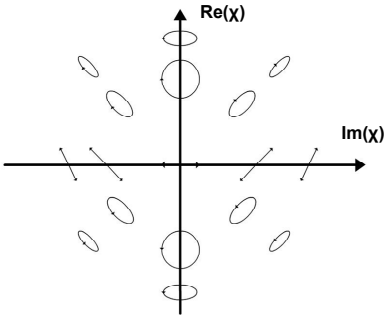

Fig.1. Possible states of light polarization. It can be seen that circular left and right polarizations are presented by two points located on imaginary axis. All linear polarizations are located on real axis. All other points on complex plane correspond to elliptical polarizations

Therefore, it is convenient to consider the Jones vectors using complex variable χ in the form**:**

$$\mathbf{E} = \begin{pmatrix} 1 \\ \chi \end{pmatrix} \tag{4}$$

Then, given the Jones matrix Eq.(1), eigenvalues and eigenpolarizations can be found in the following way:

$$\lambda_{1,2} = \frac{1}{2}\left(t_{22} - t_{11} \pm \sqrt{(t_{22}^2 - t_{11}^2) + 4t_{21}t_{12}}\right) \tag{5}$$

$$\chi_{1,2} = \frac{1}{2}\frac{t_{22} - t_{11} \pm \sqrt{(t_{22} - t_{11})^2 + 4t_{12}t_{21}}}{t_{21}} \tag{6}$$

From Eqs.(5) and (6) the degeneracy condition has the next form:

$$(t_{22}^2 - t_{11}^2) + 4t_{21}t_{12} = 0\,. \tag{7}$$

So, in terms of complex variables χ the conditions on eigenpolarizations to be coincident are:

$$\mathrm{Im}(\chi) = 0\,, \tag{8}$$

$$\chi = \pm i\,. \tag{9}$$

For a medium with degenerate linear anisotropy, it will be convenient to consider the case when linear eigenpolarizations coincide with horizontal axes of laboratory coordinate system. Then for χ we have:

$$\chi = 0 \tag{10}$$

This choice of laboratory coordinate system does evidently not restrict the generality of consideration but simplifies considerably further mathematical calculations. Using Eqs.(5)-(10) for the Jones matrix describing circular degenerate anisotropy we have:

$$\mathbf{T}_{\text{deg}}^{Cir} = \begin{pmatrix} t_{11} & t_{12} \\ t_{12} & t_{11} - 2it_{12} \end{pmatrix} \tag{11}$$

and for linear degenerate anisotropy.

$$\mathbf{T}_{\text{deg}}^{Lin} = \begin{pmatrix} t_{11} & t_{12} \\ 0 & t_{11} \end{pmatrix} \tag{12}$$

So, the generalized Jones matrices for the cases of circular and linear degenerate anisotropy have been derived.

Generalized Mueller matrix for circular degenerate anisotropy. Using the Parke matrix equation and representing the elements of Jones matrix in the form:

$$t_{ij} = a_{ij} e^{\Delta_{ij}} \tag{13}$$

then, from Eq.(11) an explicit form of Muller matrix for circular degenerate anisotropy is the following:

$$\mathbf{M}_{\text{deg}}^{Cir} = \begin{pmatrix} 3a_{12}^2 + a_{11}^2 \mp 2a_{11}a_{12}\sin(\Delta_{12}) & \pm(2a_{12}^2 - 2a_{12}a_{11}\sin(\Delta_{12})) \\ -2a_{12}^2 \pm 2a_{12}a_{11}\sin(\Delta_{12}) & a_{12}^2 + a_{11}^2 \mp 2a_{11}a_{12}\sin(\Delta_{12}) \\ 0 & -2\cos(\Delta_{12})a_{11}a_{12} \\ \pm(2a_{12}^2 - 2a_{12}a_{11}\sin(\Delta_{12})) & \mp 2a_{12}^2 \end{pmatrix}$$

$$\begin{pmatrix} 0 & \pm(2a_{12}^2 - 2a_{11}a_{12}\sin(\Delta_{12})) \\ 2\cos(\Delta_{12})a_{11}a_{12} & \mp 2a_{12}^2 \\ -a_{12}^2 + a_{11}^2 \mp 2a_{11}a_{12}\sin(\Delta_{12}) & \mp 2\cos(\Delta_{12})a_{11}a_{12} \\ \pm 2\cos(\Delta_{12})a_{11}a_{12} & -a_{12}^2 + a_{11}^2 \mp 2a_{11}a_{12}\sin(\Delta_{12}) \end{pmatrix} \tag{14}$$

Generalized Muller matrix for linear degenerate anisotropy. Internal structures of the Mueller matrices of linear and circular degenerate anisotropy. Using the mathematics analogous to that of previous paragraph, for the Muller matrix of degenerate linear anisotropy we have:

$$\mathbf{M}_{\text{deg}}^{Lin} = \begin{pmatrix} a_{11}^2 + \frac{a_{12}^2}{2} & -\frac{a_{12}^2}{2} & a_{11}a_{12}\cos(\Delta_{12}) & a_{11}a_{12}\sin(\Delta_{12}) \\ -\frac{a_{12}^2}{2} & a_{11}^2 - \frac{a_{12}^2}{2} & a_{11}a_{12}\cos(\Delta_{12}) & -a_{11}a_{12}\sin(\Delta_{12}) \\ a_{11}a_{12}\cos(\Delta_{12}) & -a_{11}a_{12}\cos(\Delta_{12}) & a_{11}^2 & 0 \\ -a_{11}a_{12}\sin(\Delta_{12}) & a_{11}a_{12}\sin(\Delta_{12}) & 0 & a_{11}^2 \end{pmatrix} \tag{15}$$

From the explicit forms of generalized Mueller matrices Eq.(14) and Eq.(15) it can be shown than both of them can be presented in the next block form:

$$\mathbf{M} = \begin{pmatrix} m_{11} & \mathbf{p}_1^T \\ \mathbf{p}_2 & \mathbf{m} \end{pmatrix} \tag{16}$$

where m_{11}-scalar values, $\mathbf{p}_1$ and $\mathbf{p}_2$ are vectors of dimension 3×1. The matrix $\mathbf{m}$ of dimension 3×3 is antisymmetric, i.e., $m_{ij} = -m_{ji}$ when $i \neq j$. In non degenerate case generalized Mueller matrices of pure type of anisotropy characterized by symmetrical matrices $\mathbf{m}$, exclude case of circular phase anisotropy, when $\mathbf{m}$ has antisymmetrical form. This fact can be used for characterized of object which has corresponding Mueller matrix.

Analyzing the internal structure of the matrix Eq.(14), it could be seen, that the matrix Eq.(14) can be completely recovered knowing only elements which form the fourth column, i.e. :

$$\mathbf{M}_{\text{deg}}^{Cir} = \begin{pmatrix} * & * & * & m_{14} \\ * & * & * & m_{24} \\ * & * & * & m_{34} \\ * & * & * & m_{44} \end{pmatrix} \tag{17}$$

The elements forming the Incomplete Mueller matrix of the form Eq,(17) can be independently measured by dynamic polarimeter.

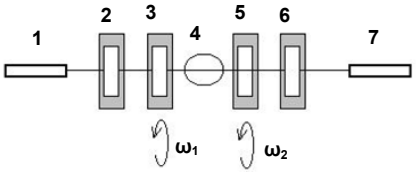

Fig.2 Scheme of dynamic Mueller polarimetr

Dynamic polarimeter consists of 1-light source, 2-polarizer, 3,5 – birefringent plates which rotate continuously with frequency ω_1 and ω_2 respectively, 6-analizer, 7-detector.

Elements of the Mueller matrix which can be measured independently can be presented in the form of next pictogram [6]:

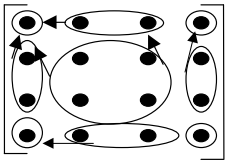

Fig.3 The structure of characteristic matrix of dynamic Mueller polarimeter

If we use incomplete structure Eq.(17), then the elements have been measured independently and number of measured elements is minimal Fig.2. This means that the values of m_{i4} in Eq.(14) will be determined with measurement errors which are lesser than for complete Mueller matrix.

From Eq.(15) structures of incomplete Mueller matrices, which completely characterized degenerate linear anisotropy, have forms:

$$\mathbf{M}_{\text{deg}}^{Lin} = \begin{pmatrix} m_{11} & m_{12} & m_{13} & m_{14} \\ * & * & * & * \\ * & * & * & * \\ * & * & * & * \end{pmatrix} \quad (18)$$

or,

$$\mathbf{M}_{\text{deg}}^{Lin} = \begin{pmatrix} m_{11} & * & * & * \\ m_{21} & * & * & * \\ m_{23} & * & * & * \\ m_{24} & * & * & * \end{pmatrix} \quad (19)$$

For the measurement of structure of incomplete Mueller matrix Eq.(18) can be used time-sequential measurement strategy in four input polarizations mode [2]. In receiving channel only total intensity (first parameter of the Stokes vector) of output light is measured. Corresponding mathematics can be presented in the following way:

$$\sum_{k=1}^{4} m_{1k} S_k^{(i)} = I_i \quad (20)$$

where $S_k^{(i)}$ – *k -th* components of *i -th* Stokes vector of incident light; I_i is total intensity of output light for *i -th* Stokes vector of incident light. Main feature of this polarimeter is absent of any polarization elements in receiving channel. This simplifies considerably the scheme of polarimeter.

In the case of measurement of incomplete Mueller matrix Eq.(19) it needs to use the complete Stokes polarimeter in receiving channel of Mueller polarimeter. Using such Mueller-polarimeter the matrix elements of structure Eq.(19) can be independently measured using time-sequential measurement strategy with completely depolarizing light [2].

$$\sum_{k=1}^{4} m_{k1} S_{k,(input)}^{(i)} = S_{k(output)}^{(i)} \quad (21)$$

In practice, as a rule, in the Mueller-polarimeter polarized source of light is used. In this case, in scope of time-sequential measurement strategy, we can use two input polarizations method [2]. This method enables to measure the next incomplete structure:

$$\mathbf{M}_{\text{deg}}^{Lin} = \begin{pmatrix} m_{11} & m_{12} & * & * \\ m_{21} & m_{22} & * & * \\ m_{31} & m_{32} & * & * \\ m_{41} & m_{42} & * & * \end{pmatrix} \quad (22)$$

Structure of incomplete Mueller matrix Eq.(22) contains the elements which forms the incomplete matrix Eq.(19), and can be used for complete characterization of object with linear degenerate anisotropy.

Thus, above results can be applied in practice for experimental characterization of object with linear degenerate anisotropy using the existing polarimeters.

Conclusions. Mueller matrix models of objects and with linear Eq.(15) and circular Eq.(14) degenerate anisotropy have been derived. In the frames of analysis of internal structures of derived Muller matrices the possible measurement schemes has been proposed. These measurement schemes enable to decrease the number of required measurements and, hence, minimize the time of measurement.

1 Berry M., Dennis M. Black polarization sandwiches are square roots of zero // J.Opt.A. – 2004. – Vol. 6. 2 Savenkov S. Optimization and structuring of the instrument matrix for polarimetric measurements // Opt. Eng. – 2002. – Vol. 41. 3 Sudha, Gopala Rao A. Polarization elements: a group-theoretical study // J.Opt. Soc. Am.A. – 2001. – Vol. 18. 4 Savenkov S., Sydoruk O., Muttiah R. Eigenanalysis of dichroic, birefringent, and degenerate polarization elements: a Jones-calculus study // Appl.Optics. – 2007. – Vol. 46. 5 Tudor T. Generalized observables in polarization optics. // J. Phys. A.- 2003. – Vol. 36. 6 Савенков С., Юштин К. Оптимизация динамического поляриметра для измерения неполных матриц Мюллера // Радиотехника.- 2002. – № 124.

Submitted on 19.06.09

UDC 535.51

S. Savenkov, Ph. D., S. Osovskyy, stud.

DEPOLARISING PROPERTIES OF ANISOTROPIC MEDIA IN INVESTIGATION OF MULLER MATRIX NUMBER OF DEGREES OF FREEDOM CONTEXT

Представлено історичні, фізичні та математичні аспекти дослідження деполяризуючих властивостей анізотропних середовищ. Досліджено типи матричних моделей анізотропних середовищ. Показано різні матричні моделі деполяризаторів. Запропоновано матричну модель для "чистого" деполяризатора. Обговорено питання узагальненої матричної моделі деполяризуючого середовища та кількості її ступеней вільності.

Ключові слова: анізотропне середовище, матрична модель, деполяризація, деполяризатор.

Historical, physical and mathematical aspects of problem of depolarizing properties of anisotropic media investigation have been presented. Types of anisotropic media matrix models have been examined. Different matrix models of depolarizers have been shown. Has been suggested a non-contradictory matrix model of "pure" depolarizer. Question about general matrix model of depolarizing media and number of its degrees of freedom has been discussed.

Key words: anisotropic media, matrix model, depolarization, depolarizer.

Introduction. One of the most important problems in contemporary theoretical polarimetry is to determine connection between Muller matrix elements of anisotropic media and its pure (deterministic) anisotropic properties. First attempts were made by Jones already in his second paper [4], devoted to polarimetry, in 1941. Bohren and Huffman wrote in 1983 [2], that Muller matrix, as function of observation angel, brings so mush information, that answer about present problem did not even stand. Nowadays, present issue got a peak of actuality.

Classification of the matrix models of anisotropic objects. There are two general classes of anisotropic objects. The first one is the class of objects, which do not influence on the degree of polarization of light, and is called deterministic or nondepolarizing. This class covers whole linear crystal optics. The second class is called depolarizing, and includes objects, which are changing the degree of polarization of propagating through them light.

If we say from physical point of vision, that we need to ascertain connection of Muller matrix elements with anisotropic properties, mathematically it means to build the

matrix model of anisotropic media. Two general approaches to build the matrix models of media are known: multiplicative and additive.

Multiplicative model, Fig.1a, assumes a graduated propagation of light through layers of anisotropic object. This model is typical for continuous media approximation [6]. Due to this model, Muller matrix of object is being presented as a product of matrixes ("building blocks"), each describing elementary fundamental anisotropic property:

$$\mathbf{M} = \prod_{i=0}^{N-1} \mathbf{M}_{N-i} \tag{1}$$

Additive model, Fig.1b, assumes interaction of propagating polarized light separately with each particle of anisotropic object and summation results of these interactions:

$$\mathbf{M} = \sum_{i=1}^{N} \mathbf{M}_i \tag{2}$$

Such model is typical for discrete media approximation [5].

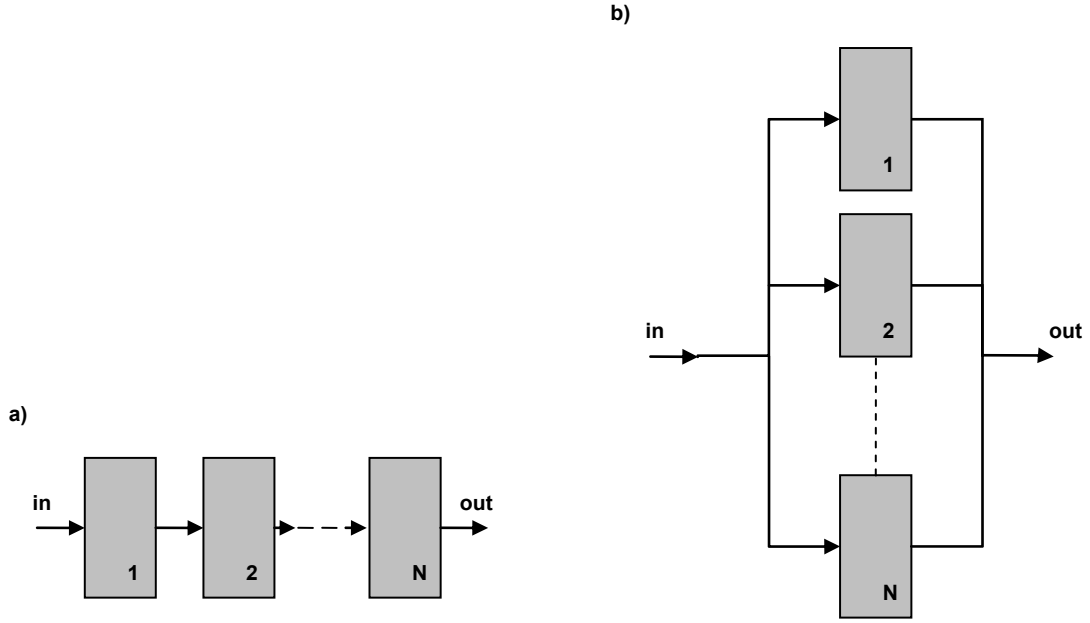

Fig.1. Schematic representation of different approaches to build of matrix model of anisotropic media

In framework of multiplicative matrix model had been built the model of nondepolarising anisotropic media [9]. It is called generalized equivalence theorem:

$$\mathbf{M}^{Gen} = \mathbf{M}^{CP}\,\mathbf{M}^{LP}\,\mathbf{M}^{CA}\,\mathbf{M}^{LA}\,. \tag{3}$$

As we see, the roles of "building blocks" play matrixes of circular phase, linear phase, circular amplitude and linear amplitude anisotropies [1, 3]:

$$\mathbf{M}^{LP} = \begin{pmatrix} 1 & 0 & 0 & 0 \\ 0 & \cos^2(2\alpha)+\sin^2(2\alpha)\cos(\delta) & \cos(2\alpha)\sin(2\alpha)\big(1-\cos(\delta)\big) & -\sin(2\alpha)\sin(\delta) \\ 0 & \cos(2\alpha)\sin(2\alpha)\big(1-\cos(\delta)\big) & \sin^2(2\alpha)+\cos^2(2\alpha)\cos(\delta) & \cos(2\alpha)\sin(\delta) \\ 0 & \sin(2\alpha)\sin(\delta) & -\cos(2\alpha)\sin(\delta) & \cos(\delta) \end{pmatrix} \tag{4.a}$$

$$\mathbf{M}^{LA} = \begin{pmatrix} 1+P & (1-P)\cos(2\theta) & (1-P)\sin(2\theta) & 0 \\ (1-P)\cos(2\theta) & \cos^2(2\theta)(1+P)+2\sin^2(2\theta)\sqrt{P} & \cos(2\theta)\sin(2\theta)(1-\sqrt{P})^2 & 0 \\ (1-P)\sin(2\theta) & \cos(2\theta)\sin(2\theta)(1-\sqrt{P})^2 & \sin^2(2\theta)(1+P)+2\cos^2(2\theta)\sqrt{P} & 0 \\ 0 & 0 & 0 & 2\sqrt{P} \end{pmatrix} \tag{4.b}$$

$$\mathbf{M}^{CA} = \begin{pmatrix} 1+R^2 & 0 & 0 & 2R \\ 0 & 1-R^2 & 0 & 0 \\ 0 & 0 & 1-R^2 & 0 \\ 2R & 0 & 0 & 1+R^2 \end{pmatrix} \quad (4.c)$$

$$\mathbf{M}^{CP} = \begin{pmatrix} 1 & 0 & 0 & 0 \\ 0 & \cos(2\phi) & \sin(2\phi) & 0 \\ 0 & -\sin(2\phi) & \cos(2\phi) & 0 \\ 0 & 0 & 0 & 1 \end{pmatrix} \quad (4.d)$$

Depolarizer matrix models. It is much more complicated to decompose a depolarizing class object's Muller matrix. In the literature there is no coordinated definition of depolarization phenomenon [11], so let consider, that depolarization is the process of decreasing of polarization degree of light while propagating through depolarizing media. Discriminated two types of depolarization: isotropic and anisotropic. Isotropic depolarization property is when the influence on polarization degree does not depend on polarization state of propagating light, and anisotropic depolarization property is when the influence on polarization degree does depend on polarization state of propagating light.

To build the adequate matrix model of depolarizing class objects we need to have "building block", responsible to depolarizing properties. In the literature are proposed some forms of depolarizer matrixes:

a) Isotropic depolarisers [10]:

– ideal depolarizer:

$$\mathbf{M}^{id} = \begin{pmatrix} 1 & 0 & 0 & 0 \\ 0 & 0 & 0 & 0 \\ 0 & 0 & 0 & 0 \\ 0 & 0 & 0 & 0 \end{pmatrix}, \quad (5.a)$$

– in fact isotropic depolarizer:

$$\mathbf{M}^{di} = \begin{pmatrix} 1 & 0 & 0 & 0 \\ 0 & d & 0 & 0 \\ 0 & 0 & d & 0 \\ 0 & 0 & 0 & d \end{pmatrix}, \quad (5.b)$$

b) Anisotropic depolarizers:

– diagonal model [8, 10]:

$$\mathbf{M}^{dm} = \begin{pmatrix} 1 & 0 & 0 & 0 \\ 0 & d_1 & 0 & 0 \\ 0 & 0 & d_2 & 0 \\ 0 & 0 & 0 & d_3 \end{pmatrix}, \quad (5.c)$$

– Lu – Chipman model [7]:

$$\mathbf{M}^{LC} = \begin{pmatrix} 1 & 0 & 0 & 0 \\ P_1 & m_{22} & m_{23} & m_{24} \\ P_2 & m_{23} & m_{33} & m_{34} \\ P_3 & m_{24} & m_{34} & m_{44} \end{pmatrix}, \quad (5.d)$$

– Williams model [12]:

$$\mathbf{M}^{MW} = \begin{pmatrix} 1 & A_1 & A_2 & A_3 \\ 0 & m_{22} & 0 & 0 \\ 0 & 0 & m_{33} & 0 \\ 0 & 0 & 0 & m_{44} \end{pmatrix}. \quad (5.e)$$

In our opinion, like each (4.a), (4.b), (4.c), (4.d) characterize one of anisotropic mechanisms, which are not interchangeable, matrix model of anisotropic depolarizer has to have the same property, then it can play role of "building block" and can be used in Muller matrix factorization. But it is easy to check, that (5.c), (5.d) and (5.e) describe objects, which are not only change the degree of polarization of the light, but also change the polarization state of light. We propose original Muller matrix model of "pure" depolarizer, which doesn't have such disadvantage:

$$\mathbf{M}^{AD} = \begin{pmatrix} m_{11} & m_{12} & m_{13} & m_{14} \\ 0 & m_{22} & 0 & 0 \\ 0 & 0 & m_{22} & 0 \\ 0 & 0 & 0 & m_{22} \end{pmatrix}. \quad (6)$$

Discussion and conclusions. While the form of depolarizing Muller matrix is determined, we can try to use it into factorization of an arbitrary Muller matrix. As known, in general case an arbitrary Muller matrix has sixteen independent elements, so it is considered, that it has sixteen degrees of freedom, which describe one of anisotropic mechanism, such as linear dichroism and birefringence and circular dichroism and birefringence, transformation of input depolarized light and depolarization. Accomplishing the generalized factorization one always has to remember, that number of degrees of freedom must stay unchangeable. This strict requirement results in some complications and some possibilities. On one hand, when we have set of separated matrices, each one describing pure anisotropic property and having an isotropic factor, the sum of degrees of freedom has a certain value. But when we have product of these matrices, it has one general isotropic factor, which factorization parts can be associated with matrices in a different ways. So, in this case one can calculate a sum of degrees of freedom in different ways. For different methods of factorization different ways of determination the Muller matrix of anisotropic depolarizer are matched. As much as possible general form of factorization, which is concerning by different authors is next [8]:

$$\mathbf{M} = \mathbf{M}^{Gen1}\mathbf{M}^{D}\mathbf{M}^{Gen2}, \quad (7)$$

where $\mathbf{M}^{Gen1}$ and $\mathbf{M}^{Gen2}$ arbitrary nondepolarizing matrixes, $\mathbf{M}^{D}$ – matrix of depolarizer of the form Eq.(5.c). By virtue of generalized equivalence theorem [9], if matrix of depolarization can be decomposed, deterministic part of it associates with $\mathbf{M}^{Gen1}$ or $\mathbf{M}^{Gen2}$, and the number of degrees of freedom decreases.

On the other hand, if some decomposition of arbitrary Mueller matrix, which consists all anisotropic mechanisms, would be suggested, and number of degrees of freedom turns out decreased, it would give us a reason to raise a question about consistency of statement, that all sixteen elements of an arbitrary Muller matrix are independent, and, maybe, it is needed to revise the very foundations of matrix model of anisotropic properties of media.

1.Azzam, R.M. and Bashara N.M.Ellipsometry and polarized light. – New York., 1977 2. Bohren C.F. and Huffman E.R. Absorption and scattering of light of light by small particles. – New York., 1983 3. Brosseau Ch. Fundamentals of polarized light. A statistical optics approach. – New York., 1998. 4. Hurwitz H., Jones C.R. A New calculus for the treatment of optical systems ii. Proof of three general equivalence theorems. – J. Opt. Soc. Am. – 1941. – 31. 5. Kim K., Mandel L. and Wolf E.: Relationship between jones and mueller matrices for random media. – J. Opt. Soc. Am. – 1987. – A, 4. 6. Landau L.D., Lifshitz E.M. and Pitaevskii L.P. Electrodynamics of continuous media. – Oxford., 1984 7. Lu S.-Y., and Chipman R.A. Homogeneous and inhomogeneous jones matrices. – J. Opt. Soc. Am. – 1994. – A, 11. 8. Ossikovski R. Analysis of depolarizing Mueller matrices through a symmetric decomposition. – J. Opt. Soc. Am. – 2009. – Vol. 26, No. 5. 9. Savenkov S.N., Marienko V.V., Oberemok E.A., and Sydoruk O.I. Generalized Matrix equivalence theorem for polarization theory. – Phys. Rev. – 2006. – E, 74, 056607. 10. Shindo Y.: Applications of polarized modulator technique in polymer science. – Opt. Eng. – 1995. 11. Shurcliff W.A. Polarized light-production and use. – Harvard., 1962 12. Williams M. Depolarization and cross polarization in ellipsometry of rough surfaces. – Appl. Optics. – 1986. – 25.

Submitted on 19.06.09.

UDC 533.9.082.5:533.924

R. Semenyshyn, stud., V. Boretskij, post grad. stud.,
I. Babich, Ph. D., A. Veklich, Ph. D.

ELECTRON DENSITY OF ELECTRIC ARC PLASMA IN SILVER VAPOURS

В роботі наведені результати вимірювання радіального розподілу електронної концентрації в плазмі електродугового розряду між срібними електродами та композиційними електродами на основі срібла (Ag-CuO). Проаналізована доцільність використання для діагностики плазми кількох спектральних ліній, розширених під впливом домінуючого квадратичного ефекту Штарка. Одержані результати порівнюються із значенням електронної концентрації у дузі між мідними електродами.

Ключові слова: електрична дуга, плазма, електронна концентрація, ефект Штарка.

In this paper the results of radial distribution of electron density in electric arc discharge plasma between silver electrodes and composition electrodes on the base of silver (Ag-CuO) are discussed. The suitability in application of some spectral lines, which are broadened by dominating quadratic Stark effect, for the plasma diagnostics is analyzed. The obtained results are compared with electron density in discharge between copper electrodes.

Keywords: electric arc, plasma, electron density, Stark effect.

Introduction. The wide application of electric arc plasma causes the significant interest in investigations of physical processes in these objects. But measurements of parameters of such plasma are the problem of great importance. Nevertheless, such kind studies of electric arc plasma will facilitate a more effectively discharge performance and more optimally development of electrode compositions as well [3, 7, 8].

It is well known that the basic physical parameters of investigated discharges (temperature or electron density) can be measured from the width of spectral lines which are emitted by plasma. This paper deals with the investigations of electric arc discharge plasma between composite Ag-CuO and silver electrodes. Namely, the main aim of this study is a spatial measurement of electron density in arc column from contours width of spectral lines. Additional task is the selection of such lines to the appropriate plasma diagnostics.

Experimental set-up. Our investigations were carried out on the experimental set-up which is shown in Fig.1.

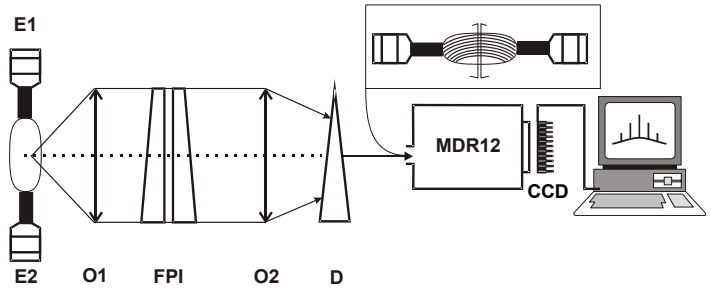

Fig. 1. MDR-12 – device of preliminary monochromatization, D – Dovet prism, O1, O2 – lenses, E1, E2 – electrodes of the arc, FPI – Fabry-Perot interferometer, CCD – linear image sensor

The free burning electric arc was ignited in air between the end surfaces of the non-cooled electrodes. The diameter of the rod electrodes was of 6 mm. The arc discharge gap was of 8 mm and the arc current was of 30 A.

Because of the discharge spatial and temporal instability the method of the single tomographic recording of the spectral line emission was used. A 3000-pixel CCD linear image sensor (B/W) Sony ILX526A accomplished fast scanning of spatial distributions of radiation intensity. Thus the recording of the radial distributions of nonstationary arc radiation intensity in arbitrary spatial sections simultaneously can be performed. The ISA interface slot of IBM PC in a control and data acquisitions is used.

In a combination with a Fabry-Perot interferometer (FPI) the spectrometer provides simultaneous registration of spatial and spectral distribution of radiation intensities. Thus, the spectrometer allows measuring contours of spectral lines in different spatial points of plasma volume [9].

We suppose that electric arc discharge plasma has axial symmetry. It means that radial distributions of each parameter of electric arc plasma (electron density, temperature and emitting atoms) are characterized by such symmetry. Previously the graphical program interface, which is based on such approach, was developed to provide the treatment of experimental obtained interferograms [9]. As a result in a case of dominating quadratic Stark effect of spectral line broadening it can be possible to measure radial profiles of electron density in a column of arc discharges.

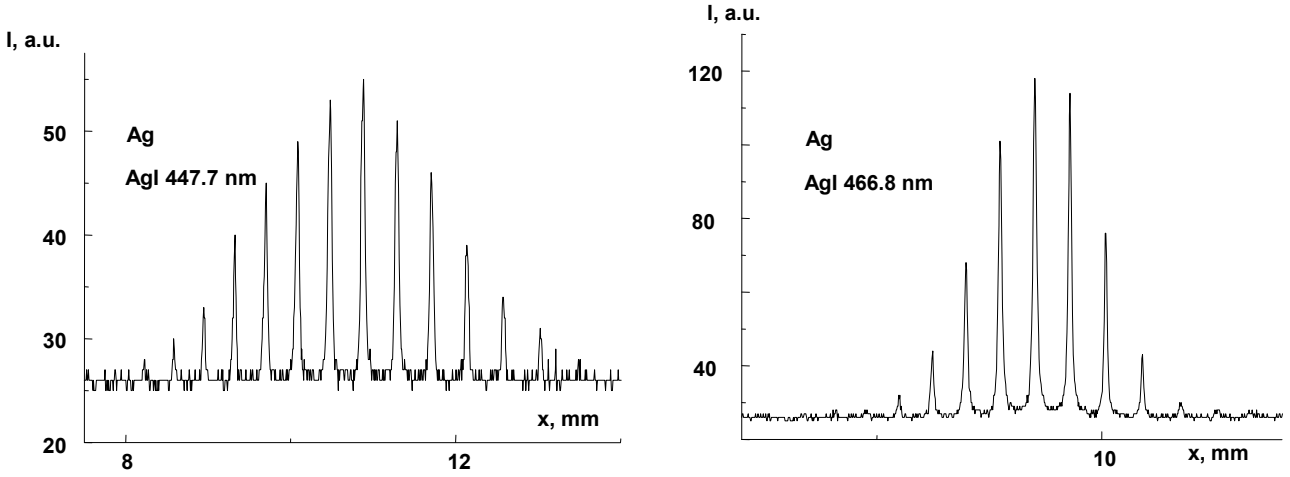

Fig. 2. Interferogramms of spectral line emissions in plasma of electric arc discharge between silver electrodes

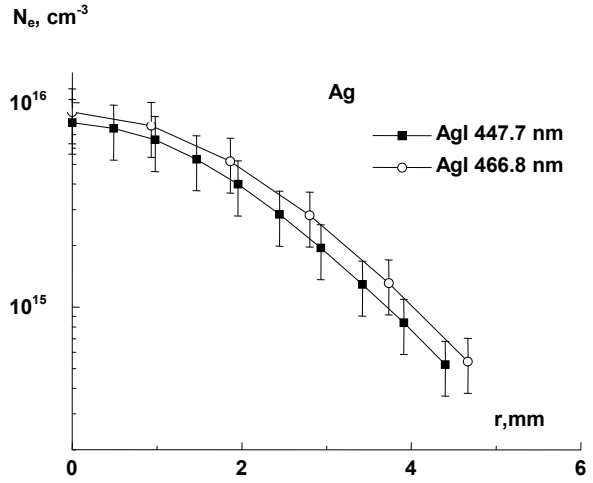

Fig. 3. Radial profiles of electron density in plasma of electric arc discharge between silver electrodes

Radial distribution of electron density. The radial distributions of electron density in plasma of electric arc discharge between composite Ag-CuO and silver electrodes were investigated. We studied interferograms of copper and silver spectral lines CuI 515.3 nm, CuI 448.0 nm, AgI 447.7 nm and AgI 466.8 nm. In the temperature range 5000-10000 K the typical value of line halfwidth, which is caused by Doppler effect, lies between 0.0021 and 0.0036 nm. The typical value of line halfwidth, which is caused by quadratic Stark effect, lies between 0.0190 and 0.0432 nm at electron density 10^{16} cm^{-3}. Necessary spectroscopic constants in such techniques were taken from papers [2, 4]. One can conclude that Doppler effect is negligible in comparison with quadratic Stark effect. So, in our investigation we supposed that the dominating broadening mechanism of these spectral lines is a quadratic Stark effect.

We measured the radial distributions of electron density in plasma of arc discharge between silver electrodes at the first stage of investigations. The spectral lines AgI 466.8nm and AgI 447.7nm as well were used (see Fig. 2, a-b). Obtained profiles of electron density are shown in Fig. 3. One can see that these profiles agree within the error of measurement. Therefore it is the reason to select these lines as well as appropriate spectroscopic constants for the purpose of diagnostics in our investigation.

At the next stage we studied interferogramms of spectral lines to measure the radial distribution of electron density in plasma of an arc discharge between composite electrodes on the base of silver Ag-CuO (see Fig. 4). Obtained profiles of electron density in such discharge column are shown in Fig. 5.

Obviously spectral line CuI 448.0 nm cannot be used in plasma diagnostics of an electric discharge between composite Ag-CuO electrodes. The matter is that this line coincides very closely with AgI 447.7 nm spectral line (see Fig. 4, a, b) in the free spectral range of FPI (0.33 nm). It was naturally to take into consideration additionally the copper spectral line CuI 515.3 nm in this case just because we successful used it in our previously investigations [1].

As it turned out the spectral lines AgI 466.848 nm unfortunately cannot be used in plasma diagnostics of an electric discharge between composite Ag-CuO electrodes too. It was found by detailed investigations of this line interferograms that it coincides very closely with CuII 466.729 nm ion copper or/and FeI 466.746 nm iron spectral lines (see Fig. 4, c). The addition of iron in composite electrons can be realized in the production process. If this is the case we can use this line in the testing of material purity. The additionally identification of spectra is still in progress and the reason of significant broadening of the spectral lines AgI 466.848nm is still to be determined.

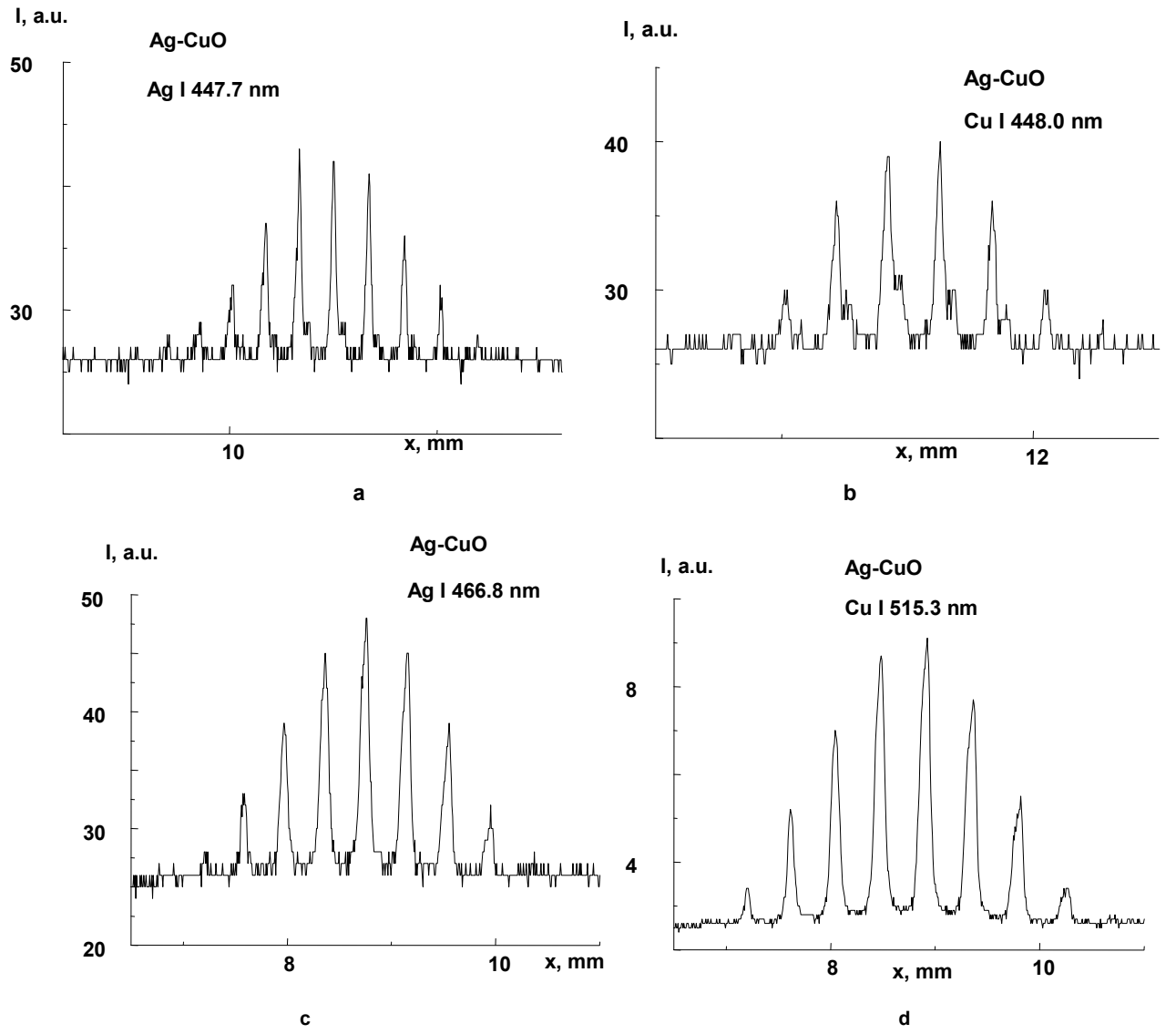

Fig. 4. Interferogramms of spectral line emissions in plasma of electric arc discharge between composite electrodes Ag-CuO

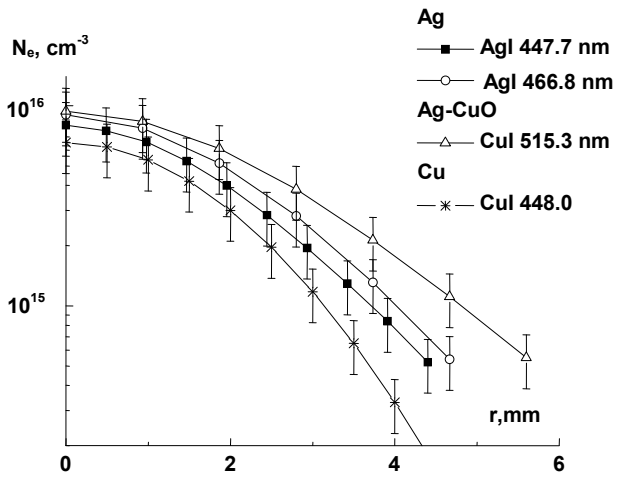

Fig. 5. Radial profiles of electron density in plasma of electric arc discharge between silver and composite Ar-CuO electrodes as well

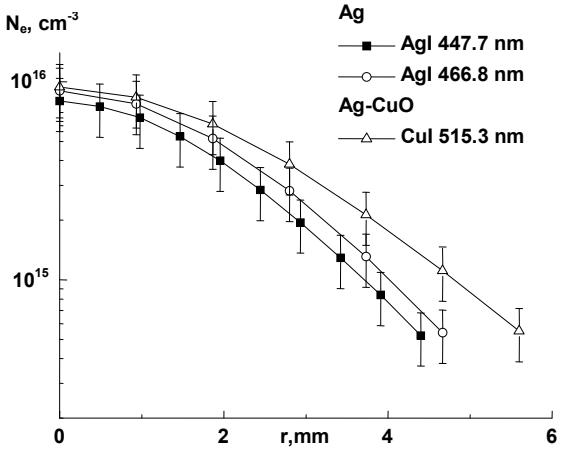

Fig. 6. Radial profiles of electron density in plasma of electric arc discharge between silver, composite Ar-CuO and copper electrodes as well

It was found that profiles of electron density obtained by various atom spectral lines agree as well within the error of measurement.

For the purpose to compare our results with the same results obtained in plasma investigation of arc discharges between copper electrodes in Fig. 6 the additional profile of electron density in this mode of arc operation is shown. We must be able to use in diagnostics the next one another copper spectral line CuI 448.0 nm in this case. Unfortunately spectral line CuI 515.3 nm was withdrawn from the consideration. The matter is that it was naturally supposed that copper atom concentration in plasma of free burning electric arc between copper electrodes is much more in comparison with an electric discharge between composite Ag-CuO electrodes. The mass ratio of component in such electrodes is 90(Ag)/10(CuO). Therefore in plasma of electric arc between copper electrodes the self-absorption of spectral line CuI 515.3 nm can be realized more significantly in a comparison with the line CuI 448.0 nm. One can be convinced of the correctness of this conclusion by comparison of corresponding spectroscopic constants of these spectral lines (see Table 1). Moreover, evaporation conditions of copper atoms from surface of copper electrodes can be differs essentially from those conditions at composite Ag-CuO electrodes. It is necessary to carry out additionally metallographic investigations of surface electrodes to found a real reason of this phenomenon.

Table 1. **Spectroscopic data for AgI and CuI spectral lines [3, 4, 5, 6].**

Element	λ, nm	E_i, eV	E_k, eV	g_i	g_k	$g_i \cdot f_{ik}$	Stark width, nm	
							T=5000, K	T=10000, K
Ag I	447.7	3.664234	6.433600	2	2	3.2e-02	0.019	0.0209
Ag I	466.8	3.778389	6.433600	4	2	6.1e-02	0.0206	0.023
Cu I	448.0	3.786150	6.552852	2	2	9.0e-03	-	0.0422
Cu I	515.3	3.786150	6.191593	2	4	4.8e-01	-	0.0346

So, to avoid any kind of experimental errors determined by probable self-absorption of spectral line CuI 515.3 nm we withdrew it from the consideration in plasma diagnostics of electric arc between copper electrodes.

Thus we can conclude that in electric arc discharges between various kinds of electrodes at arc current 30 A profiles of electron density obtained by various atom spectral lines agree within the error of measurement. Selected spectral lines as well as appropriate spectroscopic constants can be recommended to use in diagnostics of such kind plasma.

Conclusions. The radial distributions of electron density in plasma of electric arc discharges between silver electrodes or composite electrodes on the base of silver (Ag-CuO) were determinated.

The obtained results are in a good agreement with data of electron density in plasma of electric arc discharge between copper electrodes.

The selection of AgI and CuI spectral lines as well as appropriate spectroscopic constants for the purpose of diagnostics was realised. Namely, copper and silver spectral lines CuI 515.3 nm, CuI 448.0 nm, AgI 447.7 nm and AgI 466.8 nm can be used in a case of the quadratic Stark effect of the dominating broadening mechanism of these lines are recommended to use in investigations.

1. Babich I., Boretskij V., and Veklich A. Shapes of Spectral Lines of Nonuniform Plasma of Electric Arc Discharge Between Copper Electrodes // AIP Conference Proceedings. – 2007 – Vol. 938, pp. 252-257. 2. Dimitrijevic M. S., Sahal-Brechot S. Atomic Data and Nuclear Data Tables. – 2003. – V. 85 – p. 269-290. 3. Gleizes A., Gonzalez J. and Freton P. Thermal plasma modelling// J. Phys. D: Appl. Phys. – 38. – 2005. pp. R153–R183. 4. Konjevich R., Konjevich N. Stark broadening and shift of neutral copper spectral lines // Fizika. – 1986. – V. 18, № 4. – p. 327-335. 5. Ralchenko, Yu., Kramida, A.E., Reader, J., and NIST ASD Team (2008). NIST Atomic Spectra Database (version 3.1.5), [Online]. Available: http://physics.nist.gov/asd3 [2009, June 26]. National Institute of Standards and Technology, Gaithersburg, MD. 6. Smith P.L., Heise C., Esmond J.R., Kurucz R.L. Atomic spectral line database from CD-ROM 23 of R.L. Kurucz, http://cfa-www.harvard.edu/amp/ampdata/kurucz23/sekur.html, accessed May 25, 2008. 7. Veklich A. N., Osidach V. Ye. Spectroscopy of electric discharge plasma in metal vapours // Problems of Atomic Science and Technology. Series: Plasma Physics (11). 2005. №2. P. 229-231. 8. Zielinska S., Pellerin S., Valensi F., Dzierzega K., Musiol K., de Izarra Ch. and Briand F. Gas influence on the arc shape in MIG-MAG welding // Eur. Phys. J. Appl. Phys. – 43. – 2008. pp. 111–122. 9. Веклич А.М., Осідач В.Є. Визначення електронної концентрації в плазмі електродугового розряду // Вісник Київського університету. Серія: Фізико-математичні науки. Випуск N2. 2004. – С.428-435.

Submitted on 19.06.09

UDC 536.6

V. Sohatsky, Ph.D., Y. Shulimov, engineer

DETERMINATION OF CHARACTERISTICS OF COUPLED FERROMAGNETIC SPIN-VALVE LAYERS

The possibilities of coupled ferromagnetic layers characteristics determination by means of magneto-optical methods were considered. The accuracy and efficiency of their application were evaluated by means of comparison the results with electric measurements.

Key words: magnetization, spin-valve, magneto-optics.

Розглядаються можливості визначення характеристик зв'язаних феромагнітних шарів спінових клапанів магнітооптичними методами, точність та ефективність використання яких оцінюється порівнянням результатів з електричними вимірюваннями.

Ключові слова: намагнічування, спіновий клапан, магнітооптика.

Introduction. Magnetoresistive properties of sandwiches consisted of ferromagnetic nanolayers separated by non-magnetic sublayer – the so-called spin-valves (SV) are permanently the subject of interest after their discovering in 90th. This interest is caused by their extraordinary properties, that allows to use the SV as magnetic reading heads, magnetic field sensors, memory cells, etc. Studying of macroscopic magnetization reversal behaviour of exchange coupled Fe/Cu/Fe films at room temperature by means of magneto-optical Kerr effect (MOKE) magnetome-

try have some advances as e.g. the possibilities of local and total area measurements, accuracy, clearness, etc.

The absence of general theory of magnetic hysteresis and dynamics of spin reversal transition in ultra thin layers as well as necessity of improving the SV reading heads characteristics as e.g. resolution, frequency threshold, operating field range due to growing magnetic recording density caused further studying the effects of remagnetization in SV. Investigations of the equilibrium states of magnetization in SV allow to determine the dependence of electron potential on spin orientation, to evaluate the optima thicknesses of the SV layers. A lot of theoretical works using Monte Carlo simulations of the lattice Ising model, continuum model or phenomenological one, based on extensions of the classic Neel-Brown model do not give yet a complete description of the behaviour of magnetization in the SV layers with the domain structure (DS). There are also deficiencies in explanation of the role of interfaces, dynamic properties at the nanoscale, etc. Evaluation of the optima parameters of SV and correlation of calculated and experimental characteristics are still also the problem. Moreover the effects of remagnetization are too complicated for theoretical description especially in small fields because of inhomogeneities caused by the domain structure.

Experiment. MOKE magnetometry was used for studying the surface magnetization properties of the SV with various thicknesses of the layers from several monolayers till several tens of nanometres. The typical values of Kerr rotation angle of reflected from Fe plane polarized light were about 4'÷8', while the noise rate did not exceed 10''.

In order to approach to some of the above mentioned problems we've studied quasi-static and dynamic MOKE hysteresis loops, taken from the total film surface, or small local areas of the surface or from the separated cells, being also subjected to influence of the electric current in various geometries of the applied voltage. In order to clear the details of remagnetization a lateral size of the SV cells have been changed from the hundreds down to single micrometers.

The films consisted from the Fe layers with a Cu sublayer, that are modelled by non-symmetric Fe/Cu/Fe slabs could have both collinear and non-collinear magnetic configurations and the latter depends on the layers thicknesses [1]. The measurements were carried out in order to verify the availability of calculations, based on rather simple semiclassical model for description of the magnetization in SV layers and separated cells [2].

Due to complicated observation of the DS displacements on a short timescale by MOKE we used the Barkhausen jumps (abrupt changes of magnetization in changing applied field), appeared on the hysteresis loop. Variation of the focused laser beam diameter from 20 microns till several millimetres allowed to record the local and the total magnetization curves and to evaluate a velocity of the domain wall motion. The number of these jumps decreased with decreasing of the separate cells lateral sizes below several microns (depending on the ferromagnetic layer thickness) especially in the submicron range. The increasing role of rotating mechanism of remagnetization in low sized cells cause changes in the shape of the loop to more oval. Increasing of the magnitude of a.c. field as well as decreasing of the illuminated area gradually decrease a number of jumps and increase their height. At the same time decreasing of the cell size decreased MOKE signal that made more complicated application of the above method.

Technology. Three metal layers were consistently deposited by thermal method on the glass substrate in vacuum (10^{-5} Torr). The layers had various thicknesses from several nanometers till several tens nanometres that was measured by the optical transmittance. In some samples the non-magnetic intermediate Cu sublayer was done as wedge, i.e. with alternative thickness. This allowed to study the influence of thickness on hysteresis loop, magnetoresistance and other parameters of the SV. The directions of anisotropy axes of ferromagnetic layers was different because of the different position of the sources and correspondently different inclination angles of deposited substances (Fig.1a). Such a non-collinear configuration is convenient for investigations of remagnetization and perspective for creation of analogue sensors of magnetic fields.

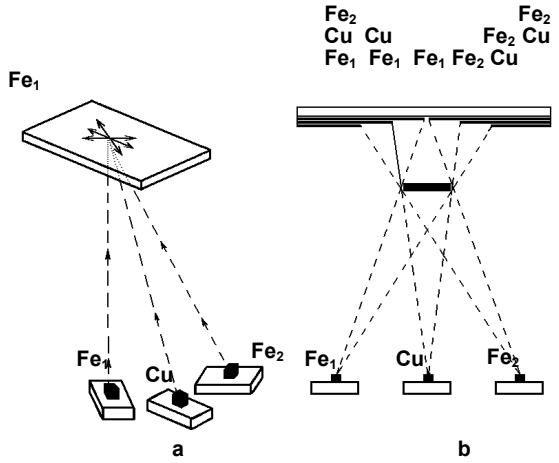

Fig.1 Spatial arrangement of the sources forming various anisotropy directions in SV layers (a) and separating layers by the shadow pattern method (b)

Additionally the individual layers of various thicknesses were deposited on another closely disposed substrates as it's shown on Fig.1b. The characteristics of such individual layers were measured for comparison with the coupled layers in sandwiched SV structures.

Results and discussion.

1. Anisotropy axes. The directions of magnetic anisotropy axes can be determined from the shape of the hysteresis loops obtained at various azimuthal directions of magnetization. The remagnetization occur from the opposite directions of $\mathbf{M}_0$ and $\mathbf{M}$ (the first is a magnetization of the hard and the last of the soft magnetic layer) to their parallel direction across the anisotropy axis. The influence of the latter leads to appearance of breaks on the hysteresis loops and to changes of their inclination (Fig. 3a,b). So the loops with breaks evidenced the existence of anisotropy axes in the soft layer and almost stable state of the hard layer magnetization $\mathbf{M}_0$.

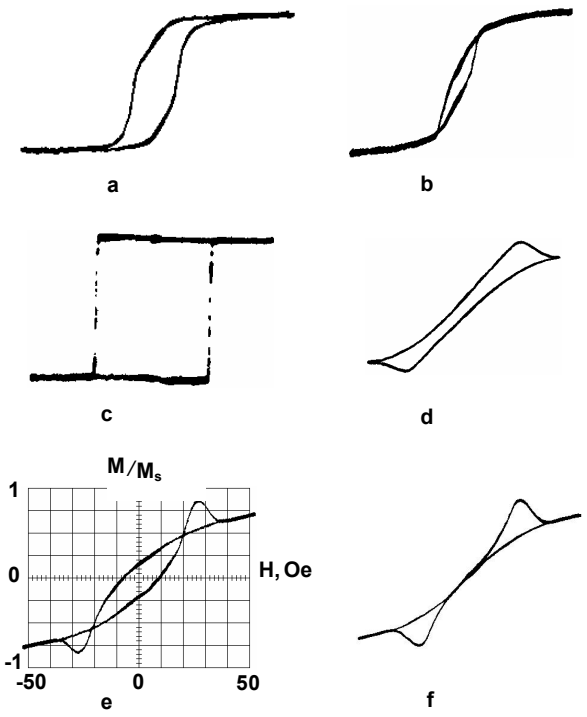

Fig. 2. Hysteresis loops taken from the top soft layer (a,c-f) and the bottom hard one (b)

Since the field of the bottom hard magnetic layer have strong influence on remagnetization of the top soft layer, so the most rectangular hysteresis loop would be in case of remagnetization along the light anisotropy axes of the top layer.

The interlaced hysteresis loop shown on Fig.2e is a result of join remagnetization of two SV layers. Initially a soft layer begins to demagnetize monotonously from saturation down to small remanence in decreasing down to zero field **H** . During the next magnetization in opposite field a monotonous increasing of magnetization (its absolute value) continue till **H** =27 Oe and then decrease in the range Δ**H** =8Oe from 27 till 35Oe. Such break of monotonous growing was caused by reorientation of the hard layer magnetization, that slightly pull the soft layer magnetization in the opposite direction. Then further growing external magnetic field again increases **M** .

A frequency threshold of the SV switching field strongly depends on mechanism of remagnetization in small fields. The motion of magnetic moment in every magnetic layer can be described by Landau's equation for magnetic moment of this layer, that have to be solved in quasi-classic approximation in order to evaluate time-dependent characteristics of magnetization:

$$\frac{\partial \overline{M_i}}{\partial t} = -\gamma_i \left[\overline{M_i} \times \overline{H_i^{Ef}} \right]$$

The effective field in equation includes external field, exchange coupling, anisotropy and demagnetizing field. The equilibrium directions of magnetization and their correlation with the layer parameters, can be obtained from the solution of the equation for free energy F dependence on the azimuthal angle:

$$\partial F / \partial \theta_i = 0$$

and the results [2] can be used for definition of the magnetization curve of SV with variable parameters:

$$M(H) = \sum_i M_i \cos(\theta_i^0)$$

This equation shows that a threshold value directly proportional to the exchange integral of the system and depends on the structure parameters and external magnetic field. So choosing parameters of the layers we can decrease a threshold current until the SV remains stable.

2. Optical transmittance and absorption. The transmittance was determined by means of optical spectrometer for visible and nearest UV and IR bands. We were able to measure optical transmittance of every layer separately due to a special mask used during the deposition and to determine the thicknesses of these layers, taking into consideration the known optical absorption and reflectance indexes of Fe and Cu surfaces. The total transmittance of three layers was also measured and compared with the values obtained for every layer.

The depth of visible light penetration in metal Fe layer $h = \frac{\lambda}{4\pi\chi}$ can be determined using of absorption index for Fe χ = 1,63. For visible spectral range one can obtain the approximate values as presented in the next table, which can be further used for evaluation of the layer thicknesses.

Table 1

λ, нм	400	500	600	700
h, нм	20	25	30	34
r, %		56	57	58

Using a formula for the intensity damping $I = I_0 e^{-\frac{4\pi\chi L}{\lambda}}$, where I_0 is an initial intensity of light; L - thickness of the layer, one can evaluate the layer thickness as $L = -\frac{\lambda}{4\pi\chi}\ln\frac{I}{I_0}$ or after substitution $L_{Fe} \approx 25\cdot\ln\left(1-\frac{T}{0{,}674}\right)$, where T is a transmittance intensity in percents.

The obtained experimental results of transmittance somewhat differ from the values, calculated with formula for reflectance $r = \frac{(n-1)^2+\chi}{(n+1)^2+\chi}$ as well as from the literature experimental data mainly because of the rough and oxidized Fe surface. Once more reason is availability of some not registered admixtures. Thus comparison of the differences of such parameters allows to roughly evaluate the quality of the surface and purity of the substance, although it's complicated to separate the contribution of the above reasons. Some conclusions can be done by exploration of the surface with scanning probe microscope but at the moment we were more interested in magnetic parameters, that also usually noticeably depends on roughness of the layer interfaces.

3. Resistivity. The resistivity of sandwiches was measured in order to determine the upper voltage limits to prevent any thermal effects of the electric current. The films demonstrate not rigorous correlation between the resistivity and optical absorption since both parameters tend to increase with increasing thickness (Fig.3).

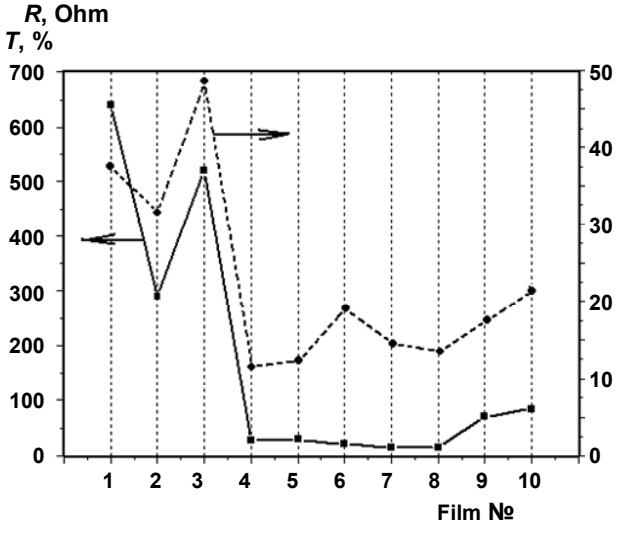

Fig. 3. Resistivity (*R*) and transmittance (*T*) of Fe/Cu/Fe and Fe/Cu/Ni (№4,5,7,8) and Ni/Cu/Ni (6) films

Break of the correlation for some films especially for №6 can be explained by much higher absorption index χ for Ni, that was used in this film as a material for both layers.

The pulses of electric current were created by means of two needle electrodes that touched the surface of top layer, which had a specific resistivity p=10^{-7} Ohm·m. The resistance of film layer between the electrodes was determined from the equation:

$U = \frac{\sigma}{2\pi\varepsilon_0}\int_a^{b-a}\left(\frac{1}{s}+\frac{1}{b-s}\right)ds \approx \frac{\sigma}{\pi\varepsilon_0}\ln\frac{b}{a}$, so the corresponding current and resistivity were as the following: $I = 2\pi ahj = 2\pi ahE/r = \frac{h\sigma}{r\varepsilon_0} = \frac{\pi hU}{r\ln(b/a)}$ and $R = \frac{r\cdot\ln(b/a)}{\pi\cdot h}$ was the typical value of resistivity, that was usually in the range 4÷40Ohm. That gives a possibility to evaluate the increasing of a local film temperature in degrees under current influence as $\Delta T = \frac{U\cdot I\cdot\Delta t}{C_{Fe}\cdot\rho_{Fe}\cdot S\cdot h+\chi\cdot S\cdot\Delta t}$. For typical indexes of the heat scattering by the surface q ~5W/m^2·deg (C_{Fe}=450J/kg·deg; ρ_{Fe}=7880kg/m^3), the increasing of the temperature for film area S=1cm^2 and thickness h=10 нм could be higher than $\Delta T \geq 100^{\circ}$C. In order to prevent the heat effects we used the short pulses less than τ <0,01s. In such a case it's possible not to take into account a scattering heat $W = \chi\cdot S\cdot\Delta T$, and the temperature shift would be:

$$\Delta T_{\max} = \frac{UI\tau}{Cm} = \frac{\pi U^2\tau}{rC\rho S\ln(b/a)} \approx 2\cdot10^4 U^2\tau .$$

So making the distance b between the electrodes shorter than 1 mm it is possible to rich the current density $j = \frac{I}{S} = \frac{I}{2\pi\cdot s\cdot h}$ ~10^6÷10^7 A/cm^2 without essential heating of the sample. The currents of just such densities are used for remagnetization of the SV soft layer by polarized electron transport [3, 4]. The films studied in this work were intended just for the experiments with polarized currents. Moreover, the DS of the films with rectangular hysteresis loop can be simply changed by moving of the domain wall. The energy of such remagnetization is much lower [5] than in case of magnetization vector rotation, considered in [3, 4]. Thus we can evaluate a total magnetic moment carrying by the polarized electrons as $M = \frac{DI\mu_B}{e_V hc}$, where μ_B is Bohr magneton and use the equations for energy balance and magnetic moment motion [5] for further calculations of the SV parameters, that are fit in the best way for such a remagnetization, caused in particular by polarized current [6].

Conclusions. Magneto-optical method is an effective tool for investigation of remagnetization in ferromagnetic layers of the SV up to mesoscopic scale. Remagnetized soft layer of the SV tends to break on non-periodic domains with a variable size in case of the structural inhomogeneities availability. It's stayed monodomain in case of regular crystallography with minor admixtures. Comparison of the observed differences between the local and integrated characteristics of the SV have shown the tendency of increasing coercivity, switching field with decreasing of lateral sizes of the separated SV cells.

1. Qian D., Jin X. F., Barthel J., Klaua M., and Kirschner J. // Phys. Rev. Lett. – 2001.– 87. 2. Сохацький В.П., Макаров Д.Г. // Неоднорідне перемагнічування спінових клапанів. Вісник Київського університету. Сер. фіз.-мат. науки. – 2005.- №3. 3. Slonczewski J.C. Current-driven excitation of magnetic multilayers // Journal of Magnetism and Magnetic Materials. 1996.– 159, №1-2. 4. Katine J.A., Albert F.J. et.al. Current-Driven Magnetization Reversal and Spin-Wave Excitations in Co/Cu/Co Pillars // Phys. Rev. Lett.–2000.– 84. 5. Гуляев Ю.В., Зильберман П.Е., Панас А.И., Эпштейн Э.М. Спинтроника: обменное переключение ферромагнитных металлических переходов при малой плотности тока // УФН.- 2009.- 179, №4. 6. Sohatsky V., Shulimov Y. Effect of current on spin-valve layer magnetization. Abstr. of V Int. Conf. "Functional Materials" (ICFM-2009), Oct. 5-10, Partenit, Ukraine. – P.172.

Submitted on 30.03.10

UDC 621.382

M. Tyhanskyi, Ph. D., A. Partyka, master,
O. Kharko, student.

THE EFFECT OF THE DURATION OF OPERATIONAL CURRENT IMPULSES ON THE SPEED AND STABILITY OF JOSEPHSON CRYOTRONS

В даний час на основі джозефсонівських тунельних переходів S-I-S типу та джозефсонівських контактів містко-вого типу створено такі логічні пристрої як запам'ятовуючі елементи та зсувні регістри. Труднощі, пов'язані із розробкою та створенням таких структур, мають як технологічний, так і фізичний характер. Фізичні проблеми пов'язані з тим, що ще не повністю вивчені особливості перехідних процесів, які проходять в таких елементах пам'яті під час керування їх логічним станом та зміни логічного стану, оскільки джозефсонівські логічні пристрої є складними нелінійними квантовими коливними системами.

Ключові слова – джозефсонівський кріотрон, інформаційний перетворювач, квантова комірка пам'яті, перехідні характеристики, логічний перехід.

To date, based on S-I-S Josephson tunnelling junctions and Josephson bridge contacts, such logical devices as memory cells and shift registers have been created. The development of these devices faces difficulties of both technical and physical character. The physical problems are due to the fact that the transitional processes that take place in such memory cells during the change of their logical state have not yet been fully understood since Josephson logical devices are complex non-linear oscillatory systems.

Key words – Josephson cryotron, information transformer, quantum memory cells, transitional characteristics, logical transition.

Introduction. Nowadays, there have been developed such logical devices as memory cells and shift registers, created on a basis of S-I-S Josephson tunnelling junctions and Josephson bridge contacts [1-3, 6, 8]. Josephson logical devices have relatively high operation speed, low power consumption during the logical state switching, and small sizes in the micron and submicron range. Besides, it is technologically possible to combine individual Josephson elements into high-density matrices. The development of such structures is connected with technological as well as physical complications. The physical problems are mainly due to our insufficient understanding of the transitional processes that take place in these memory devices during the change of their logical state since Josephson logical devices are complex non-linear quantum oscillatory [5, 7].

In our previous publications [4, 9, 10], we reported on having created a mathematical model of transitional processes in Josephson memory cells (cryotrons) based on S-I-S Josephson structures. The transitional characteristics of the cryotrons based on high-temperature superconductors for direct ("0" $\rightarrow$ "1") and inverse ("1" $\rightarrow$ "0") logical transitions, that were obtained by means of mathematical modeling, let us conclude that the operation speed of such cryotrons, whose commutation time was found to be 2-5 ps, can considerably exceed that of traditional computer memory cells. In the present work, we perform further investigations of physical processes in Josephson cryotrons. Namely, we calculate the cryotrons' transitional characteristics for the case when the change in their logical state is triggered by current impulses and analyze the influence of the controlling impulses' duration on the commutation time, which defines the cryotrons' operation speed.

Mathematical model of transitional processes. The mathematical model of transitional processes in Josephson cryotrons is based on the following differential equation [4]

$$I_P = I_C \sin\phi + \frac{C\hbar}{2e}\frac{d^2\phi}{dt^2} + \frac{G(V)\hbar}{2e}\frac{d\phi}{dt}\ , \qquad (1)$$

where I_P is the operational electrical current flowing through the cryotron, I_C is the cryotron's critical current, C is the junction's capacity, $G(V)$ is the tunnel junction's conductance in the case of single-electron tunneling (in general, the conductance G depends on the voltage V across the cryotron), $\hbar$ is the Planck's constant, e is the electron charge, $\phi(t)$ is the unknown function that describes the time dependence of the phase difference of the superconductors' wave-functions on both sides of the tunnel barrier. Once $\phi(t)$ is found, one can use the well-known equation for the non-stationary Josephson effect,

$$V(t) = \frac{\hbar}{2e}\frac{d\phi}{dt} = \frac{\hbar}{2e}\phi'\,, \qquad (2)$$

and find the cryotron's transitional characteristic $V(t)$ – the time dependence of voltage $V(t)$ during the change of the cryotron's logical state – that contains the information about the course of transitional processes and allows to determine the commutation time – the characteristic time of a transitional process.

For the operation temperature T = 11,6 K, the voltage to current (V-I) characteristic was approximated by a simple mathematical function:

$$I(V) = G_0 \cdot \left[0{,}942 \cdot V - \frac{0{,}940V}{1+(0{,}054V)^{15{,}5}}\right], \qquad (3)$$

where G_0 is the normal conductance of the tunneling junction in the range of voltages, where the junction becomes ohmic. In the model, we used the V-I characteristic for the temperature that is by a few degrees higher than the boiling temperature of liquid helium in order to account for the cryotron's local heating. On the other hand, it is known that the V-I characteristics of a S-I-S structure are weakly dependent on temperature provided that it is much lower that the critical temperature [10]. The logical state of the cryotrons was controlled by external current impulses, whose shape was given by the mathematical function: $I_i(t) = I_0 \exp\left(-\frac{(t-t_n)^4}{t_{0n}{}^4}\right)$, where I_0 is the amplitude of the current impulse, the parameter t_{0n} defines the average duration of the nth impulse Δt_n (Δt_n = $2t_{0n}$), t_n is the time when the nth current impulse was applied. Such a shape of $I_i(t)$ was chosen among a series of impulses $e^{-t^2}, e^{-t^4}, e^{-t^6}, e^{-t^8}$, … because of the following reasoning. First, the e^{-t^4} impulses are more localized in time compared with the e^{-t^2} impulses. Second, mathematical expressions with the e^{-t^4} impulses do not complicate the

working differential equations as much as the e^{-t^6} or e^{-t^8} impulses do [9]. In order to obtain the transitional characteristic of the cryotron $V(t)$, we solved the differential equation:

$$I_p + I_0 \exp\left(-\frac{(t-t_1)^4}{t_{01}^{\ 4}}\right) - I_0 \exp\left(-\frac{(t-t_2)^4}{t_{02}^{\ 4}}\right) = \frac{C\hbar}{2e}\phi'' + \left[G_0 \cdot \left[0{,}942 \cdot V - \frac{0{,}940 \cdot V}{1+(0{,}054 \cdot V)^{15{,}5}}\right]\right] \times \frac{\hbar}{2e}\phi' + I_c \sin\phi\,, \qquad (4)$$

where t_1 and t_2 are the times when the first and the second impulses were applied, t_{01} and t_{02} are the halved durations of the first and the second impulses, respectively.

Determination of the commutation time. In Fig. 1, we present the transitional characteristic of the cryotron $V(t)$ during logical transitions "0" $\rightarrow$ "1" and "1" $\rightarrow$ "0", calculated by solving Eq. (4) with the following model parameters: I_C = 0,0155 mA, I_P = 0,008 mA, C = 0,82 $\times 10^{-3}$ pF, G_0 = 0,58 $\times 10^{-3}$ Ω^{-1}, I_0 = 0,008 mA, t_1 = 10 ps and t_2 = 30 ps. At t_1 = 10 ps, a current impulse was applied to the cryotron, causing the increase of the operation current by the value of I_0, which then led to the increase of the cryotron's current and initiated a transitional process corresponding to a logical transition "0" $\rightarrow$ "1". After the logical transition had been completed, the voltage V_0 set on across the cryotron. The value of this voltage is determined by the V-I characteristic of the Josephson tunneling junction and is approximately equal $\frac{\Delta}{e}$, where Δ is the energy gap of the superconductors that are used in the S-I-S tunneling junction. The commutation time of the cryotron in the case of logical transitions "0" $\rightarrow$ "1", $\Delta\tau_1$, was defined as a time interval during which the voltage $V(t)$ changed from $0{,}1V_0$ to $0{,}9V_0$.

Analogously, we defined the commutation time of the cryotron in the case of a logical transition "1" $\rightarrow$ "0", $\Delta\tau_2$, that started at t_2 = 30 ps, after the second current impulse had been applied. As can be seen from Fig. 1, this transitional process was not smooth, but rather had an oscillatory character, with damped oscillations of voltage $V(t)$ across the cryotron. The commutation time of the cryotron in the case of the logical transition "1" $\rightarrow$ "0", $\Delta\tau_2$, was defined as a time interval from the moment when the transitional process began to the moment when the amplitude of the voltage oscillations became less than $0{,}1V_0$. So far we believe that it is impossible to obtain logical transitions "1" $\rightarrow$ "0" without voltage oscillations.

The cryotron's transitional characteristic shown in Fig. 1 corresponds to a stable operation regime since it demonstrates that the logical transitions "0" $\rightarrow$ "1" and "1" $\rightarrow$ "0" took place, i. e., that the cryotron changed its logical state.

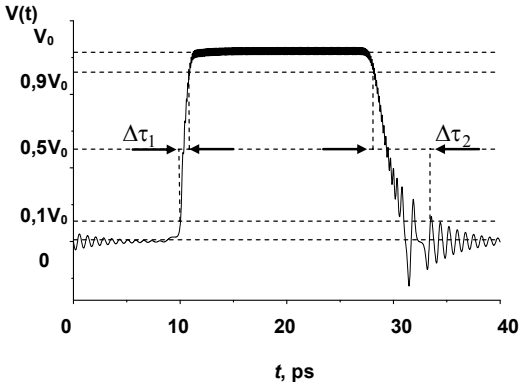

Fig. 1. The transitional characteristic of a cryotron during logical transitions "0" $\rightarrow$ "1" and "1" $\rightarrow$ "0".

The dependence of the commutation time on the duration of controlling impulses. In order to obtain the dependence of the commutation times of direct and inverse logical transitions ($\Delta\tau_1$ and $\Delta\tau_2$, respectively) on the duration of controlling impulses, we calculated transitional characteristics for different Δt_1 and Δt_2 values and determined $\Delta\tau_1$ and $\Delta\tau_2$ from them. The amplitudes of the controlling impulses as well as the rest of the model parameters were fixed. We took into account only those transitional characteristics that demonstrated stable operation. In the case when the cryotron's operation is unstable, i. e., the controlling impulses do not trigger an expected transition, it is meaningless to speak about a commutation time. In Fig. 2, we present the calculated dependence of the commutation time $\Delta\tau_1$ of direct logical transitions on the duration of controlling current impulses Δt_1. One should note that $\Delta\tau_1(\Delta t_1)$ does not behave monotonously, but instead has a well pronounced minimum at Δt_1 = 2 ps. This dependence can be used for optimization of the cryotrons' parameters and enhancing their operation speed. In the range from Δt_1 = 1 ps to Δt_1 = 3 ps, the commutation time $\Delta\tau_1$ is minimal and does not exceed 3 ps. When the duration of controlling impulses is less than 0,5 ps, the cryotron does not change its logical state from the initial state of logical "0", i. e., the direct logical transition "0" $\rightarrow$ "1" does not occur. Such a regime is classified as unstable. In the interval Δt_1 > 3 ps, the increase of the duration of controlling impulses leads to increasing of the commutation time as well, and for Δt_1 > 6 ps the cryotron's operation becomes unstable. For a given set of model parameters, we found that the optimal duration of controlling current impulses is Δt_1 = 2 ps, which provides the commutation time as short as $\Delta\tau_1$ = 1 ps.

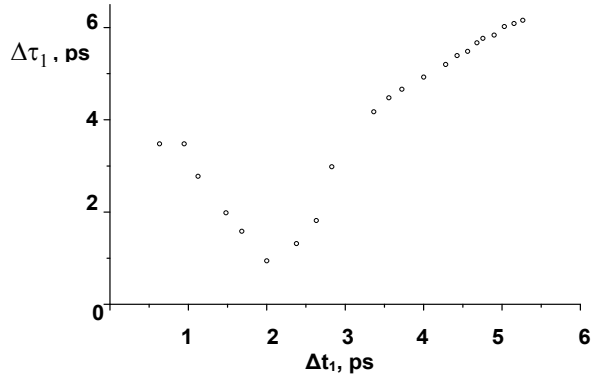

Fig. 2. The dependence of the commutation time $\Delta\tau_1$ on the duration of controlling current impulses Δt_1 for logical transitions "0" → "1"

Similarly, we obtained the dependence $\Delta\tau_2(\Delta t_2)$ for inverse transitions "1" → "0" (Fig. 3). In this case, however, $\Delta\tau_2(\Delta t_2)$ does not have a well pronounced minimum. In the interval from Δt_2 = 3 ps to Δt_2 = 6 ps the commutation time increases, while in the interval from 6 ps to 10 ps it almost does not depend on the duration of controlling impulses Δt_2 and varies only slightly from 6,5 ps to 7 ps. When the duration of controlling current impulses Δt_2 is less than 3 ps, the cryotron enters an unstable operation regime, i. e., the inverse logical transition "1" → "0" does not occur. For Δt_2 > 10 ps the commutation time considerably increases, and for Δt_2 > 15 ps the cryotron's operation also becomes unstable. We therefore conclude that the duration of controlling current impulses Δt_2 = 4 – 6 ps should be regarded as optimal, which allows to decrease the commutation time down to 5 – 7 ps.

By comparing the results that we obtained for direct logical transitions "0" → "1" and inverse logical transitions "1" → "0", we can arrive at the following conclusions: i) the duration of controlling current impulses Δt_1 has no effect on the transitional processes during inverse logical transitions "1" → "0" and the commutation time $\Delta\tau_2$, and *vice versa*; ii) it is required that the duration of controlling impulses for inverse logical transitions "1" → "0" be by a factor of 2 -3 longer than that for direct logical transitions "0" → "1"; iii) in the optimal operation regime, the speed of the cryotrons is larger in the case of direct logical transitions "0" → "1" since $\Delta\tau_1 \approx$ 2 ps while $\Delta\tau_2 \approx$ 5 – 7 ps.

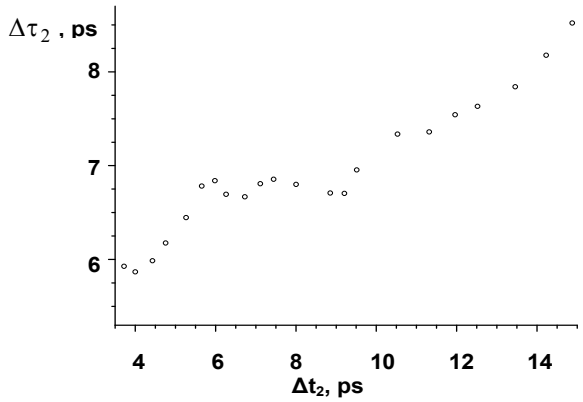

Fig. 3: The dependence of the commutation time $\Delta\tau_2$ on the duration of controlling impulses Δt_2 for logical transitions "1" → "0"

Conclusions. The dependences of the commutation time on the duration of controlling current impulses are obtained from the calculated transitional characteristics of the Josephson cryotrons. These dependences are then used for determination of intervals of stable operation of the cryotrons and for optimizing the model parameters such as to achieve higher operation speeds of the cryotron-based memory cells. The analysis of the obtained results leads us to the following conclusions:

1) the duration of controlling current impulses that trigger direct logical transitions "0" → "1" does not affect in any way the transitional processes during inverse logical transitions "1" → "0" and their commutation time, and *vice versa*;

2) for inverse logical transitions "1" → "0", the controlling current impulses have to be of 2 – 3 times longer duration than those for direct logical transitions "0" → "1";

3) in the optimal operation regime, the operation speed of the cryotrons is higher in the case of direct logical transitions since their commutation time $\Delta\tau_1 \approx$ 2 ps while the commutation time for inverse logical transitions $\Delta\tau_2 \approx$ 5 – 7 ps.

1.Ilyin Y., Nijhuis A. and H.H.J. ten Kate Interpretation of conduit voltage measurements on the poloidal field insert sample using the CUDI–CICC numerical code // Cryogenics. – 2006. – Vol. 46. Is. 7-8. – P. 517-529. 2. Kwanwoo N., Sangkwon J. Novel flow analysis of regenerator under oscillating flow with pulsating pressure // Cryogenics. – 2005. – Vol. 45. Is. 5. – P. 368-379. 3. Plantenberg J. H., P. C. de Groot, C. J. P. M. Harmans, and J. E. Mooij Demonstration of controlled-NOT quantum gates on a pair of superconducting quantum bits // Nature -- June 14, 2007 -- Volume 447, Issue 7146, pp. 836-839. 4. Tyhanskyj M.V., Partyka A.I. Determination of stability intervals for Josephson cryotrons // Thematic Issue "Electronics and Communications", p.2, № 4-5, 2009., p.11-16. 5. Yerin Y.S. and Omelyanchouk A.N. Coherent current states in a two-band superconductor // Fizika Nizkikh Temperatur, – 2007, – v. 33, – No.5, p. 538–545. 6. [Yoshinao Mizugaki, Yoko Namatame and Masaaki Maezawa Design and operation of a series array of voltage doubler cells for rapid-single-flux-quantum digital-to-analog converters // Supercond. Sci. Technol. 20 S315-S317, Issue 11, 2007. 7. Глухов А.М., Турутанов О.Г., Шнырков В.И., Омельянчук А.Н. Стохастический резонанс в сверхпроводящих контурах с контактами Джозефсона. Численный эксперимент // Физика низких температур, – 2006, – т. 32, № 11, – с. 1477–1487. 8. [Зуев А. Г. Инновации в криоэлектронике // СПб. : Бизнес-пресса, 2002, 58 с. 9. Тиханський М.В., Партика А.І. // Вісник НУ "ЛП" "Електроніка", №592, 2007р., с. 143-148. 10. Тиханський М.В., Шуригін Ф.М., Тиханська К.М. // Вісник НУ "ЛП" "Електроніка", №482, 2003р., с. 152-161.

Submitted on 26.09.09

UDC 5681.325.5:533.9.082.5

S. Fesenko, stud., V. Boretskij, post grad. stud.,
A. Veklich, Ph. D.

PULSE POWER SUPPLY OF ELECTRIC ARC DISCHARGES

В роботі наведені результати розробки імпульсного джерела живлення із стабілізацією струму для виконання досліджень плазми дуги, що горить між плавкими електродами. Розглянуті проблеми створення такого джерела та запропоновані шляхи їх вирішення. З метою балансування схеми розроблений оригінальний програмний алгоритм для реалізації широтно-імпульсної модуляції із залученням мікроконтролера ATtiny2313 фірми Atmel.

Ключові слова: джерело живлення, широтно-імпульсна модуляція, мікроконтролер.

The development of the pulse power supply with a current stabilization is discussed. The problems of this power supply development as well as methods of such problems solving are considered. The original program algorithm is realized on the base of Atmel microcontroller ATtiny2313 to provide the pulse-duration modulation in balancing scheme.

Keywords: power supply, pulse-duration modulation, microcontroller.

Introduction. The research and development activity in the field of the low-temperature plasma deals often with a thermal arc technology. Such kind of industrial branch is based on the application of electric arc discharges with the aim to have a source of a heat power. Many of these techniques have been used over many years. Nevertheless the base physics processes in plasma of such sources must be still clarified. The additional investigations of plasma parameters are carried out by many scientific groups nowadays. That is why the development of the stabilized power supplies of such electric arc discharges is the goal of great importance. The many kind of commercial or experimental prototypes of such supplies are well known [1-3]. But the sufficient disadvantage of industrial units is that the ratio of quality and price is unacceptable.

The main aim of this paper is the development of the pulse power supply of electric arc discharges with a current stabilization.

Development and discussion. In Fig. 1 the block diagram of this power supply is shown.

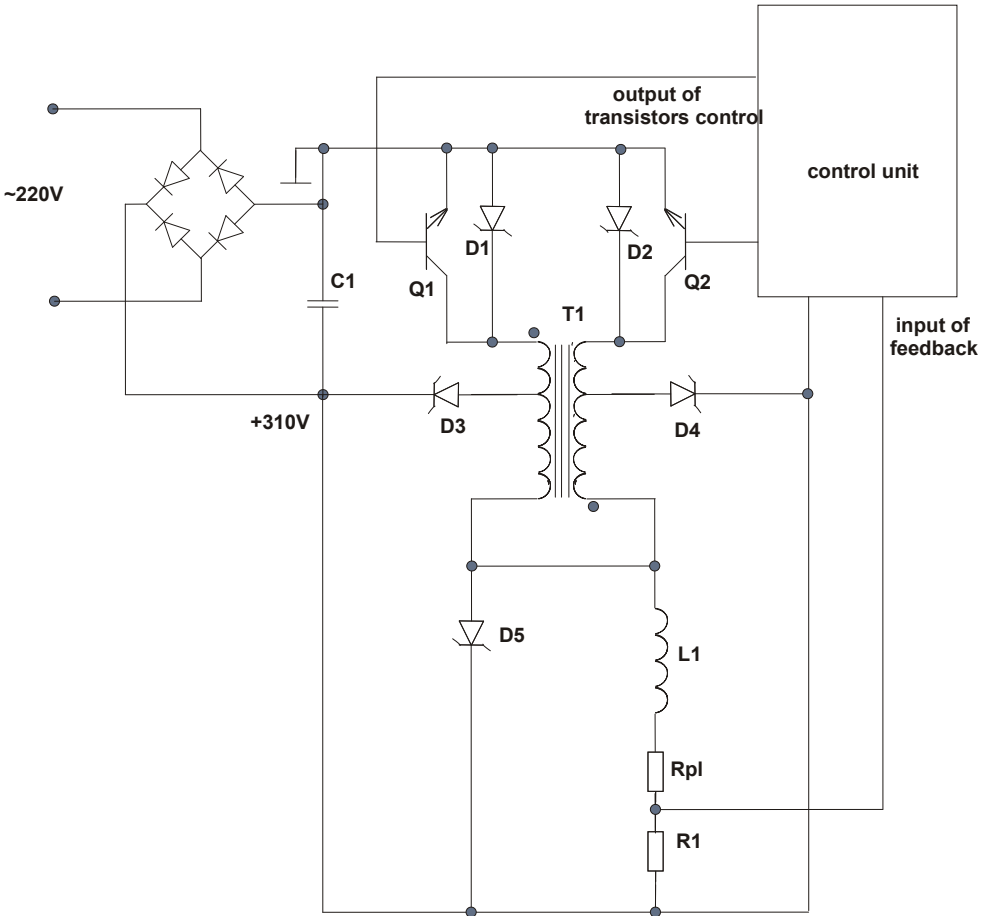

Fig. 1. The block diagram of the pulse power supply of electric arc discharges with a current stabilization

The general principle of this scheme operation is next. The AC voltage enters the AC/DC converter which is assembled by the bridge circuit. The no-load DC voltage of 310 V is smoothed by the electrolytic capacitor C1 of high capacity. At the next step the DC voltage is converted by power transistors to the AC voltage of high frequency. The matching load is realized by pulse transformer T1. Then the AC voltage is rectified by high frequency diodes D3 and D4. This DC voltage is smoothed by the choke L1. Then it enters the load (the electric arc discharge Rpl).

The control unit monitors transistors performance. It measures the current in the resistance Rpl by the measuring of the standard resistor R1 voltage and the following comparing with a reference one. So, the feedback signal is

generated to the stabilization of the arc discharge current by the transistor current cutoff. This pulse-duration modulation (PDM) method is chosen with the aim of the current rise acceleration in the load on the power supply up.

The unit of the PDM controller as a base of the power supply unit is shown in Fig.2. The eight-bit Atmel microcontroller ATtiny2313 was used in this scheme. The operation of the PDM controller is in the following. The microcontroller renders one of two transistors conductive and makes a zeroing of the counter register TCNT0 of the eight-bit timer-counter T0. When the counter register TCNT0 achieves the value, which is wrote down to the register OCR0A, the interruption is called by a channel A.

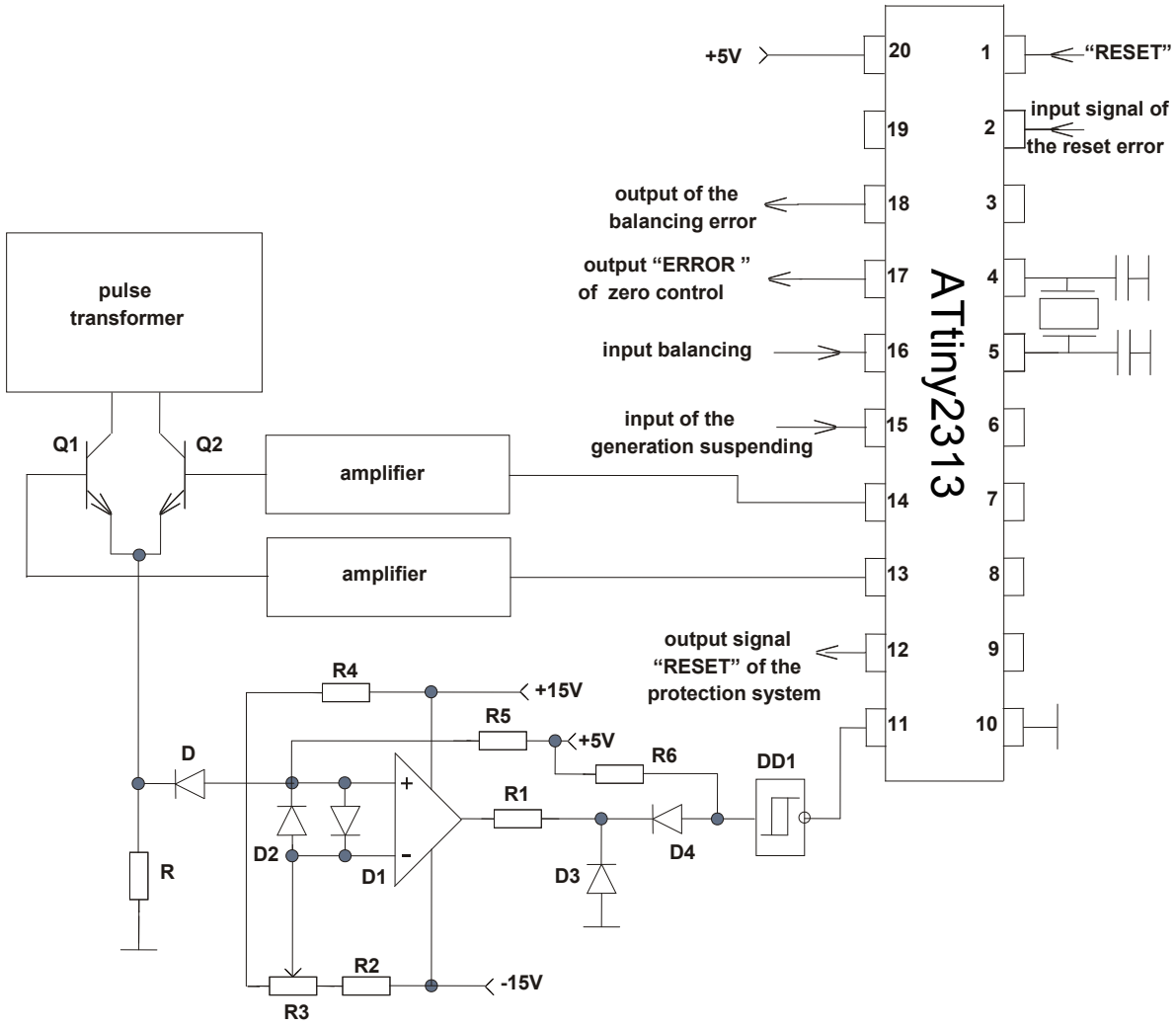

Fig. 2. The unit of PDM controller

The drive transistor is cut-off and microcontroller's input signals are red as well by the interrupt-handling procedure. When this procedure is finished the current balance check of transistors is realised by operational amplifier which is shown in the scheme. It is performed to avoid the simultaneous rendering of both transistors conductive as soon as this situation looks like the short circuit of the power supply 310 V.

If the both transistors current is nonzero then the microcontroller generates the output error signal on the lead "17" and waits the transistors current cut-off. After that it renders another transistor conductive. Until this transistor is rendered the test of the balancing scheme signal takes place (the lead "16" of the microcontroller).

Sometimes the asymmetrical winding at the stage of a production of the pulse transformer was taken place. In this case transformer windings afford the different incremental inductance. Therefore the demagnetization of the transformer will be insufficient at the alternate switching of transistors. As a result the saturation will take place.

To avoid this situation the balancing scheme is realised on a base of the special designed program algorithm. Its hardware implementation is performed by the microcontroller. Namely, the lead "16" of the microcontroller takes part in this algorithm realization (see Fig.2).

The additional special stabilization unit (see Fig.3) was developed to form the signal of the generation suspending. This signal is formed when the load current takes the maximal defined value. As a load current probe the standard resistor is used. This resistor R1 is shown in Fig.1. The stabilization is realised due to the comparison of the resistor voltage with the standard one. As a result of comparison the feedback signal to the microcontroller is formed. This signal terminates the generation until the decreasing of the load current.

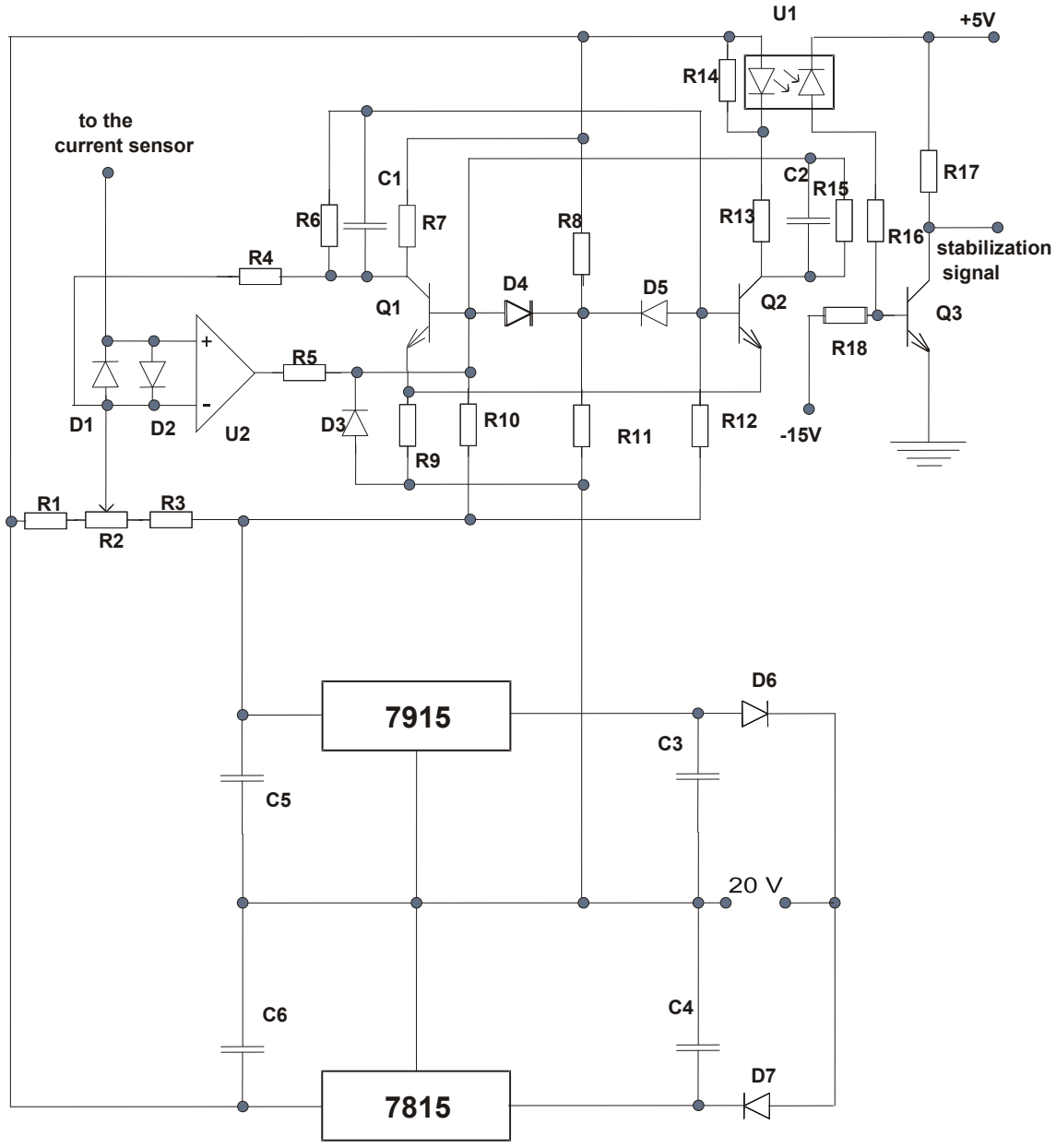

Fig. 3. The special stabilization unit to form the signal of the generation suspending

Conclusions. The original pulse power supply of electric arc discharges with a current stabilization was developed. The universal Atmel microcontroler ATtiny2313 was used to realize the pulse-duration modulation. The scheme balancing is provided by the special original program algorithm of the microcontroller in the case of asymmetrical transistors currents.

1. Hartman D. Design & Build your own Arc Welder. – http://www.dansworkshop.com/electricity-and-electronics /homebuilt-arc-welder.htm 2. Володин В. Сборник статей. – http://valvolodin.narod.ru/articles.html 3. Сварочные аппараты. – http://corason.com.ua/db1/ mag/495

Submitted on 19.06.09

UDC 303.714, UDC 681.5.01

N. Yaremchuk, Ph. D., V. Shvedova, assist.

THE MONITORING OF DISTANT EDUCATIONAL SYSTEMS AND AUTOMATICALLY TESTING SYSTEMS

На основі аналізу показників якості тестових просторів, їх метрик та шкал оцінювання обрано ті з них, що можуть бути використані при проведенні пілотного експерименту та моніторингу систем дистанційного навчання (СДН) та систем автоматизованого тестування (САТ). Удосконалено відомі способи оцінювання показників якості тестових просторів СДН та САТ на основі введення непараметричних оцінок. Запропоновано інформаційно-вимірювальне та алгоритмічне забезпечення СДН та САТ.

Ключові слова: показники якості тестових просторів, пілотний експеримент, моніторинг систем дистанційного навчання та систем автоматизованого тестування.

On basis of the analysis the characteristics of quality of tests spaces, its metrics and evaluation scales chose such that can be used for realization pilot experiment and monitoring distant educational systems (DES) and automatically testing systems (ATS). Improved known means for quality evaluation of the such characteristics by introducing non-parametric estimations. Propose the information-measuring and algorithmic support for monitoring of DES and ATS.

Key words: characteristics of quality of tests spaces, pilot experiment, monitoring distant educational systems and automatically testing systems.

Introduction. Wide development of distant educational systems (DES) and automatically testing systems (ATS) need to elaboration algorithmic support for monitoring such systems. The monitoring DES and ATS should be developed on the all stages of working up these systems: creation the project, strategic calculation, developing, pilot experiment and exploitation [1], in such of which must be realized fixed tasks. The special importance the monitoring of DEC and ATS mean during of standardization and exploitation. If the systems destination for small samples of students, than execution of effective standardization such systems can not be realized, because are not enough experimental data for estimation characteristics of quality. Therefore, the monitoring of systems allows to receive experimental data for more precise preliminary results and for decreasing uncertainty of obtained estimations. So, solution the task of estimation the characteristics of quality DES and ATS, that are based on experimental data, were offered in this article.

Theoretical study the problem. With that end in view carried out investigation of the characteristics of quality DEC and ATS, its metrics and evaluation scales, that can be measured during pilot experiment and experimental exploitation. The characteristics of quality, which was examined: reliability of testing procedure, validity, differential ability and difficulty of test's items.

On basis of analysis and systematization existence methods were chose such us can be used as base on different stages of life cycle DEC and ATS.

As a base means for estimation of reliability the testing procedure on the stages of pilot experiment and exploitation chose mean with evaluation the reliability of each test's items by cross-correlation of results obtained for this items. For calculation reliability of the test on the whole as a base chose Spearman-Brown's formula.

The survey and analysis the kinds of validity, methods and means for its estimation allows to chose as a base algorithm by rank biserial correlation of test execution results.

The analysis of a posteriori methods of estimation the item test's difficulty allows to chose the means by appraisement the statistic level of accomplish the test's items. For estimation of differential ability was chose coefficient of Yule.

The calculation of its indexes of quality in the classic theory carry out with using primary marks of test's items (the sum of correct answers on each test's items) and primary marks of students (the sum of correct answers on test's items for each student), that are sufficient statistics of multitude of primary data of test's results. At the same time show up the contradiction, that is as follows. The multitude of primary marks of test's items and marks of students are empirical system with behavior manifestations – ratio of equivalence and ratio of order:

$$\mathrm{Q} = \langle Q; \sim; \succ \rangle,$$

where Q – behavior manifestations, $\sim;\succ$ empirical manifestations of equivalence and ratio of order.

For said above statistics is absent the ratio of size proportionality behavior and ration for intervals. Therefore basic data of the test's results are reflected ordinary scale $\mathrm{N} = \langle N; =; > \rangle$ with allowable dealerships at elements of scale in list: bigger, smaller, equal.

But most of means for estimation the quality indexes DEC and ATS based on using operations for metrical scales (calculation of simple average, quadratic mean such as in Spearman-Brown's formula, act). Such contradiction the scale using pedagogical measurement was notice in [2].

Therefore during estimation of quality indexes for DEC and ATS expedient to modify chose base means by using nonparametric estimations for central tendency and for dispersion of test's results. In particular, offered to use stable methods of estimation, based on median. It is correct because: first – in respect to theory of scales and it is optimal approach than have a small samples with unknown distribution.

Thus propose use median as a central tendency and use as measure of dispersion chose estimation dispersion. For improvement of base methods of estimation the quality indexes for DEC and ATS during pilot experiment and exploitation were applied follow modifications [3].

The estimation of reliability the testing procedure.

During pilot experiment proposed use modified Kuder-Richadson formula:

$$R_{KR} = \frac{L}{L-1}\left(\frac{S_x^2 - \sum_{j=1}^{L} p_j q_j}{S_x^2}\right),$$

where L – quantity of test's items, p_j – part of students who answered on test item, $q_j = p_j - 1$; S_x – dispersion dispersion.

The standard uncertainty of reliability by modified Kuder-Richadson formula can be calculate as :

$$u[R_{KR}] = \frac{4}{\sqrt{3}} \cdot R_{KR} \cdot \Delta_z \cdot e^{2Z_{KR}} \left(\Delta_z \cdot e^{2Z_{KR}} + 1\right)\left(e^{4Z_{KR}} - 1\right)$$

where Z_{KR} – Fisher transformation R_{KR}, Δ_Z – expanded uncertainty of Z_{KR}, $\Delta_Z = Z_\kappa (n-3)^{-\frac{1}{2}}$, Z_κ critical value with given confidence level.

The reliability the testing procedure during exploitation proposed to estimate by modified Spearman-Brown's formula:

$$R_{SB} = \frac{L \cdot \underset{j=1,2...L}{med}\left\{r_j\right\}}{1+(L-1)\cdot \underset{j=1,2...L}{med}\left\{r_j\right\}}, \qquad r_j = \sqrt{\underset{i=1,2...L}{med}\left\{r_{ij}\right\}}$$

where $\underset{j=1,2...L}{med}\left\{r_j\right\}$ – median of rang consecution row of correlation coefficients each test's items.

$$r_{ij} = \frac{p_{ji} - p_j p_i}{\sqrt{p_j q_j p_i q_i}},$$

p_{ji} – part of students who answered on both test's items, p_j – part of students who answered on one test item ($q_j = 1 - p_j$), p_i – part of students who answered on other test item ($q_i = 1 - p_i$).

The standard uncertainty of reliability by modified Spearman-Brown's formula can be calculate as:

$$u[R_{SB}] = \frac{S \cdot k \cdot \left(2 - \underset{j=1,2...k}{med}\left\{r_j\right\}\right)}{1+(k-1)\cdot \underset{j=1,2...k}{med}\left\{r_j\right\}}.$$

The estimation of test item validity. For estimation of test validity proposed use modified rank biserial correlation:

$$r_{bis} = (med\left\{r_B\right\} - med\left\{r_H\right\})\frac{2}{N},$$

where $med\left\{r_B\right\}$ – median of rang primary marks of students who answered on test item, $med\left\{r_H\right\}$ – median of rang primary marks of students who do not answered on test item, N – quantity of students.

The standard uncertainty of test item validity can be calculate as:

$$u[r_{bis,i}] = \frac{\left[b'_{Bv,i} + b'_{Hv,i} - b'_{Bu,i} - b'_{Hu,i}\right]}{n\sqrt{3}},$$

where $b'_{Bu,i}, b'_{Bv,i}, b'_{Hu,i}, b'_{Hv,i}$ – elements of rang primary marks of students who answered and do not answered on test item by fractile of normal distribution.

The estimation of test item difficulty. For estimation of test difficalty proposed use modified formula [4]:

On the base of proposed algorithms was developed information-measuring and algorithmic support for monitoring of distant educational systems and automatically testing systems.

$$T_{\Pi j} = \frac{N_{Hj}}{N} \cdot \frac{med\left\{x_j\right\}}{med\left\{x\right\}},$$

where N – quantity of students who took part in the testing, N_{Hj} – quantity of students who answered on test item, $med\left\{x_j\right\}$ – median of rang primary marks of students who answered on test item, $med\left\{x\right\}$ – median of rang primary marks of students who took part in the testing.

The standard uncertainty of test item difficulty can be calculate as:

$$u[T] = \sqrt{\frac{T_\Pi \cdot (1 - T_\Pi)}{N}}.$$

The estimation differential ability of test's items. For estimation of differential ability test's items proposed coefficient of Yule:

$$Q = \frac{N_{11}N_{22} - N_{12}N_{21}}{N_{11}N_{22} + N_{12}N_{21}},$$

N_{ij} – quantity of students in criteria groups.

The standard uncertainty of estimation can be calculate as:

$$u[Q] = \sqrt{\frac{1}{4}(1-Q^2)^2\left(\frac{1}{N_{11}} + \frac{1}{N_{12}} + \frac{1}{N_{21}} + \frac{1}{N_{22}}\right)}.$$

Practical realization. At the chair of information-measuring systems National Technique University "Kiev Polygenic Institute" on the base of proposed metrics was developed information-measuring and released algorithmic support for monitoring of distant educational systems and automatically testing systems.

The genera scheme of monitoring DES (ATS) what was used illustrated by fig 1.

The estimation of quality coefficients released with using special software and are using at the chair for monitoring test area of real DES during last few years.

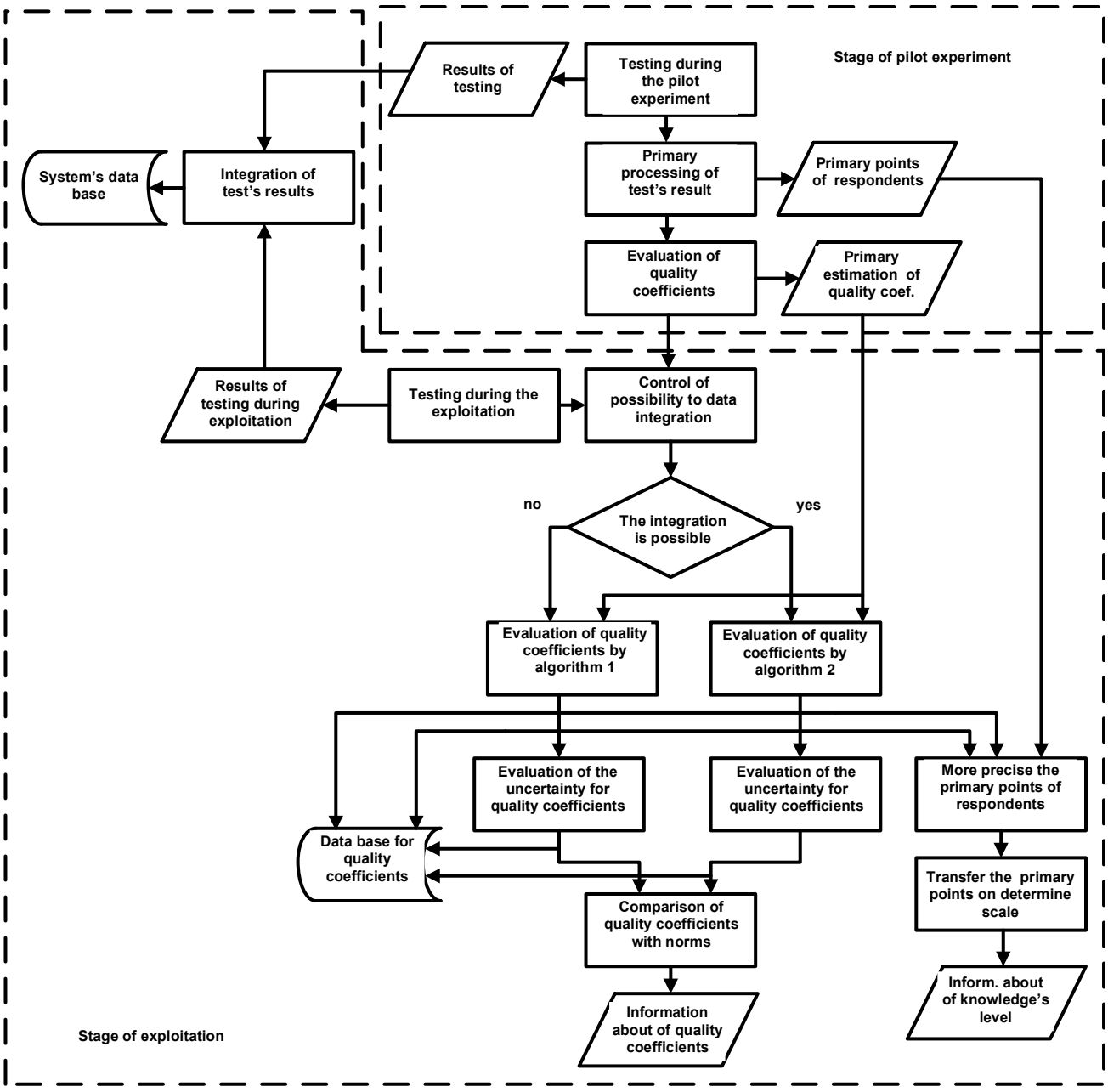

Fig.1. Scheme of monitoring DES (ATS)

Conclusions. On the base of systematization legacy methods of quality coefficients, its metrics and estimation scales chose methods and means that can be use during pilot experiment and exploitation DES and ATS. Chose means modified by using non parametric estimations. On the base of developed information-measuring support was released algorithmic support for monitoring DEC and ATS, created software and carried out approbation on real DES.

1. Ціделко В.Д., Яремчук Н.А., Шведова В.В. Опыт создания дистанционных курсов общеинженерного профиля // Вища технічна освіта: перспективи розвитку в контексті болонського процесу: Матер. VIII Міжнар. наук.-метод. конф., Київ, 2007 р. 2. Нейман Ю.М., Хлебников В.А. Введение в теорию моделирования и параметризации педагогических тестов. – М., 2000. 3. Yaremchuk N. A., Shvedova V. V. The Problems of evaluation the quality coefficients of distant educational systems (DES) // release of IX international young scientists' conference on applied physics, Kyiv, 2009. 4. Шведова В.В. Оцінювання показників якості контролюючих тестів при пілотному експерименті та в режимі дослідної експлуатації систем дистанційного навчання // Наукові вісті. – 2007. – № 3.

Submitted on 19.06.09

UDC 548.24

A. Kosogor, Ph. D. stud., V. L'vov, Doct. Sci.

AFFECT OF INTERNAL STRESSES ON CYCLIC MARTENSITIC TRANSFORMATIONS OF TI–NI–FE ALLOY

The influence of preliminary mechanical/thermal cycling on the transformational and deformational properties of shape memory alloys has been analysed in the framework of ferroelastic model of martensitic phase transformations. The Ti–Ni–Fe alloys, which undergo the phase transformations of cubic-rhombohedral type, have been considered. The physical effect of destabilisation of martensitic phase due to the mechanical/thermal cycling of the single crystalline alloy specimen has been explained. To this end the phase transformation temperatures have been determined for the different numbers of preliminary cycles. It has been shown that the cycling reduces the martensite start temperature on the value of about 5 K. The non-linear stress–strain dependencies that are relevant to the stress-induced martensitic transformations have been computed. The experimentally observed elevation of the threshold stress value that is needed for the triggering of stress-induced martensitic transformation has been explained.

Keywords: martensitic transformation, martensite destabilisation, defect reconfiguration.

З використанням фероеластичної моделі мартенситних фазових перетворень проаналізовано вплив циклічної зміни механічного навантаження (або температури) на трансформаційні та деформаційні властивості сплавів з ефектом пам'яті форми. Розглянуто сплави Ti–Ni–Fe, у яких відбуваються фазові перетворення кубічно-ромбоедричного типу. Надано пояснення фізичному ефекту дестабілізації мартенситної фази, що виникає завдяки циклічній зміні механічного навантаження (або температури). Із цією метою визначено температури фазових перетворень, які відбуваються після різної кількості попередньо здійснених циклів. Показано, що попередні цикли знижують температуру початку мартенситного перетворення на величину близько 5 К. Розраховано нелінійні залежності механічного напруження від деформації, які притаманні тим мартенситним перетворенням, що спричинені механічним напруженням. Пояснено експериментально спостережене зростання порогової величини напруження, необхідного для здійснення такого мартенситного перетворення.

Ключові слова: мартенситне перетворення, дестабілізація мартенситу, реконфігурація дефектів.

1. Introduction. The Ti–Ni–Fe alloys undergo the martensitic transformation (MT) on cooling [7]. The MT transformation can also be induced by the axial compression of alloy specimen in certain crystallographic directions (see e.g. [8] and references therein). It was discovered very recently that the transformation properties of martensitic alloys can be changed by the mechanical/thermal cycling thought the MT stress/temperature value [1, 2]. The internal mechanical stresses, which are induced in the alloy specimen by the reconfiguration of crystal defects, were assumed to be the reason of the observed changes in the transformation behaviour of martensitic alloys [2]. On the other hand, the reconfiguration of crystal defects causes the well-known effect of martensite stabilization [6]. The macroscopic theory of this effect was proposed in [5]. The theory is based on the conception of internal mechanical stresses, which arise in the alloy due to the reconfiguration of crystal defects. As it was assumed in [2], the internal stresses are also responsible for the changes of critical stress/temperature values observed in the course of mechanical/temperature cycling of the single crystalline specimens of martensitic alloys.

In the present article this assumption was confirmed by the theoretical analysis of cyclic stress/temperature-induced MT-s. The analysis was carried out in the framework of well-grounded ferroelastic model of MT-s.

2. Results. In the work [5] the multicomponent order parameter η_α, which describes the slow reconfiguration of lattice defects after MT, was proposed for the description of martensite aging. The Gibbs potential of the crystal with defects was presented in the form

$$G = F_e(u_\alpha) + F_r(\eta_\alpha) + F_{er}(u_\alpha, \eta_\alpha) - 3\sigma_1 u_1 - 2(\sigma_4 u_4 + \sigma_5 u_5 + \sigma_6 u_6), \quad (1)$$

where $F_e(u_\alpha)$ and $F_r(\eta_\alpha)$ are the free energies describing the elastic and defect subsystems, $F_{er}(u_\alpha, \eta_\alpha)$ is the energy of interaction between these subsystems, $\sigma_1 = (\sigma_{xx} + \sigma_{yy} + \sigma_{zz})/3$ and $\sigma_4 = \sigma_{zy}$, $\sigma_5 = \sigma_{xz}$, $\sigma_6 = \sigma_{xy}$, σ_{ik} are the stress tensor components (u_α are related to the strain components as the values σ_α are expressed through the components of the applied mechanical stress).

We consider that the coordinate axes are aligned with the $\langle 111 \rangle$ crystallographic directions and the cubic-rhombohedral MT, which is induced by the loading of single crystalline specimen in [111] direction, is studied. In this case $\sigma_4 = \sigma_5 = \sigma_6$, $u_4 = u_5 = u_6$, and the energy is expressed as

$$F_e = c_1 u_1^2/2 + 6C_{44}u_4^2 + 3a_3 u_1 u_4^2/2 + a_5 u_4^3 + 3bu_4^4/4 + b_8 u_1 u_4^3, \quad (2)$$

c_1, $a_{3,5}$, b and b_8 are the phenomenological parameters introduced in [3], C_{44} is a temperature-dependent shear elastic modulus.

The energy of defect reconfiguration in the course of MT is expressed by the equation

$$F_r = \gamma_1 \eta_1^2/2 + 3\gamma_3 \eta_4^2/2 \quad (3)$$

and the interrelation between the defects configuration and strains is described by the term

$$F_{er} = -d_1 \eta_1 u_1 - 3d_3 \eta_4 u_4, \quad (4)$$

where $\gamma_{1,3}, d_{1,3}$ are phenomenological parameters.

The condition $\partial G/\partial u_1 = 0$ allows to express the u_1 variable through u_4, σ_1 and η_1. The substitution of expressed variable into Eq. (1) results in the following renormalization of the phenomenological parameters and stresses:

$$C_{44}(T) \to C_{44}^*(T,n) = C_{44}(T) + 3a_3\sigma_1^{(eff)}(n)/c_1,$$
$$a_5 \to a_5^*(n) = a_5 + 3b_8\sigma_1^{(eff)}(n)/c_1, \quad (5)$$
$$b \to b^*(n) = b - 3a_3^2/2c_1,\ \sigma_{1,4} \to \sigma_{1,4}^{(eff)}(n),$$

where n is the number of cycles. The effective stresses $\sigma_\alpha^{(eff)}(n)$ are defined as $\sigma_\alpha^{(eff)}(n) = \sigma_\alpha + \sigma_\alpha^{(i)}(n)$, where the values

$$\sigma_1^{(i)}(n) = d_1\eta_1(n)/3, \quad \sigma_4^{(i)}(n) = d_3\eta_4(n)/2 \quad (6)$$

can be interpreted as the internal stresses (IS), which are induced by the mechanical or thermal cycling. These stresses are caused by the disturbance of the equilibrium state of compound system consisting of the atoms situated in the regular crystallographic positions (quickly deformed subsystem) and crystal defects (slow subsystem evolving due to the diffusion processes).

According to Ref. [2] the IS, which arises in the course of cyclic stress-induced MT, can be subdivided into the isotropic Destabilising Pressure (DP) and Stabilising Axial Stress (SAS). The IS tensor has the following structure:

$$\sigma_1^{(i)}(n) = -p(n),\ \sigma_4^{(i)}(n) = \sigma_5^{(i)}(n) = \sigma_6^{(i)}(n) \equiv \sigma^{(i)}(n), \quad (7)$$

where $p(n)$ is the DP and $\sigma^{(i)}(n)$ is SAS.

The dependencies of components of reconfiguration order parameter on cycle number n are expressed as

$$\eta_\alpha = \eta_\alpha^{(eq)}\left[1-\exp(-n/n_\alpha)\right], \quad (8)$$

where $n_{1,4}$ are the characteristic integers prescribing the variation rate of these components [5].

To describe the influence of mechanical/thermal cycling on the transformational behaviour of the martensitic alloys the stress–temperature phase diagram must be constructed using the minimum conditions for Gibbs potential. The equations for the lability lines of cubic and rhombohedral phase can be obtained following the Ref. [3] and expressed as

$$\sigma_{\min}(\theta) = -\frac{1}{27}R_-(9\theta - 12R_- - 4R_-^2),$$
$$\sigma_{\max}(\theta) = -\frac{1}{27}R_+(9\theta - 12R_+ - 4R_+^2), \quad (9)$$

where $R_\pm = 1 \pm \sqrt{1-3\theta/4}$, the variables $\sigma = \sigma_4 a_5^*(t)/2c_R^2(t)$ and $\theta = c_3^*(t)/c_R(t)$ may be thought of as the dimensionless stress and temperature, respectively, $c_R = (a_5^*)^2/4b^*$. The austenitic phase is stable under the condition $\sigma > \sigma_{\min}$ while the martensitic state can be observed when $\sigma < \sigma_{\max}$; in the interval $\sigma_{\min} < \sigma < \sigma_{\max}$ both austenitic and martensitic phases coexist. The solutions of Eq. (9) form the phase diagram, which can be plotted in both $\sigma - \theta$ and $\sigma_{yz} - T$ (stress-temperature) planes. The stress-temperature phase diagram constructed for Ti–Ni–Fe alloy is shown in Fig. 1. The values of the coefficients involved in Eq. (5) are presented in Table 1. (These values were obtained in Ref. [4]). The temperature dependencies of shear modulus $C_{44}(T)$ and order parameter $u_R(T)$, which were used for computations, have been determined from these values as explained in Ref. [4]. Besides that, the following values of parameters involved into Eq. (6), (8) were chosen: $p(0) = -5$ GPa, $\sigma^{(i)} = 10$ MPa, $n_1 = 10$ and $n_4 = 5$.

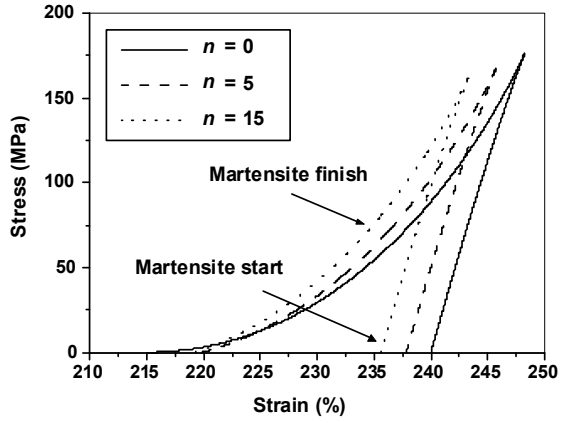

Fig. 1. Theoretical phase diagrams of Ti–Ni–Fe alloy corresponding to the MT that goes *on cooling* of the alloy before mechanical cycling ($n = 0$), after five and fifteen ($n = 5$ and $n = 15$) stress-strain cycles. These phase diagrams correspond also to the first, sixth and sixteenth stress-induced MT-s

Table 1. **Numerical values used for computations**

$a_5(0)$ [GPa]	$b_5(0)$ [GPa]	T_1 [K]	T_2 [K]
$-2.4\cdot10^4$	$1.2\cdot10^6$	240	215
a_3/c_1	b_8/c_1	$C_{44}(T_1)$ [GPa]	c_R [GPa]
1.8	18	30	120

The constructed phase diagram enables a theoretical analysis of those changes in the transformational properties of Ti–Ni–Fe alloy, which are caused by the preliminary mechanical cycling of single crystalline alloy specimen. It shows that the cycling narrows the temperature range of martensitic phase, i.e. causes the destabilisation of martensite. The reduction of martensite start temperature after 15 cycles is of about 5 K.

The shifts of characteristic transformation temperatures are presented in Fig. 2 for the different numbers of preliminary cycles. The Fig. 2 shows the dependencies of martensite start and finish temperatures, i. e. the values $\Delta_{MS} \equiv T_2^*(n) - T_2^*(0)$ and $\Delta_{MF} \equiv T_1^*(n) - T_1^*(0)$, respectively. The value $\Delta_{MT} = (\Delta_{MS} + \Delta_{MF})/2$ can be referred as the shift of MT temperature. The value $\Delta_{12} \equiv T_1^*(n) - T_2^*(n)$ is the narrowing of the temperature range of two-phase (i.e. mixed austenitic-martensitic) state. The results of computations show that the cycling causes:

i) the monotone decrease of the martensite start temperature and the narrowing of the temperature range of mixed austenitic-martensitic state;

ii) the non-monotone change of the martensite finish and MT temperatures;

iii) the change of sign of MT temperature after the rather large ($n > 10$) number of cycles.

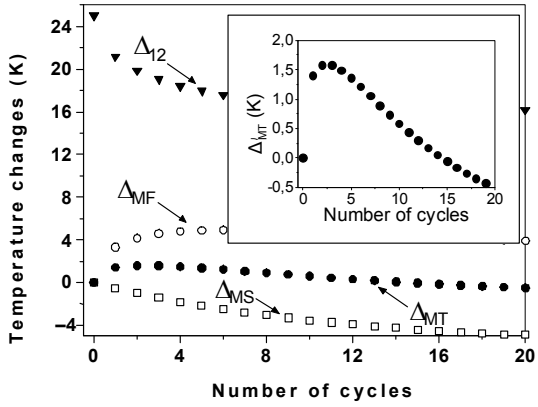

Fig. 2. The shifts of the characteristic temperatures of MT caused by the cyclic mechanical loading of the alloy specimen. The inset illustrates the non-monotony and change of sign of the MT temperature shift

The mechanical/thermal cycling of the alloy specimen not only causes the shifting of characteristic transformation temperatures, but also changes the threshold stress value that is needed for the initiation of the stress-induced MT. This effect is pronouncedly illustrated by the solid and dashed lines ($n = 0$ and $n = 5$) in Fig. 3, which shows the computed stress–strain dependencies. The dotted and dash-dotted lines illustrate the non-linear stress-strain dependencies computed for the case when the alloy temperature exceeds the critical temperature, which corresponds to the end point of the lability lines shown in Fig. 1.

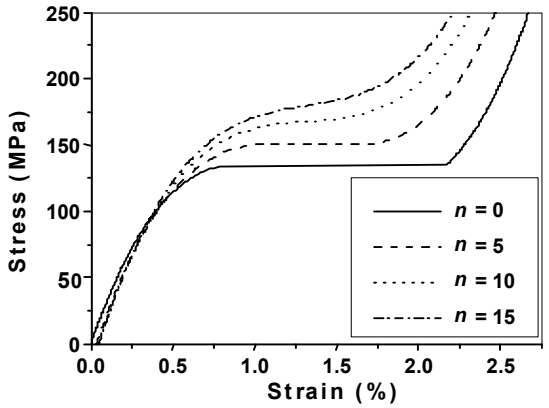

Fig. 3. The stress–strain dependencies taken after the different number of mechanical loading-unloading cycles

The affect of mechanical cycling on the stress-strain dependencies has clear physical reasons. The martensite destabilisation originated by cycling is, in the same time, a stabilisation of austenitic phase. Due to this stabilisation the stress value that is needed for the transformation of austenitic phase into the martensitic one increases after the preliminary cycling of the alloy specimen.

3. Conclusion. The reported above theoretical results substantially expand a conception of slowly variable mechanical stresses, which are originated in the crystal by the reconfiguration of crystal defects after the martensitic phase transformation. (This conception was proposed very recently in Refs. [5,4]). The computations show that the internal stressing not only causes the well-known effect of martensite stabilisation, but also explains the physical reasons of recently discovered in Refs. [1,2] strong dependence of the transformational and deformational properties of shape memory alloys on the preliminary mechanical/thermal cycling of the single crystalline specimens. Moreover, the theoretical analysis predicts the non-monotone character of the dependence of MT temperature on the number of preliminary cycles. The shift of MT temperature changes sign after the rather large number of cycles.

Physically, the influence of mechanical and thermal cycling on the transformational properties of shape memory alloys represents the destabilisation of martensitic phase. This physical effect is opposite to the well-known phenomenon of martensite aging and can be called the martensite youngering.

1. Chernenko V.A, Villa E., Besseghini S., Barandiaran J.M. High-temperature tensile superelasticity in Ni-Mn-Ga alloys // E-MRS, 2010. 2. Chernenko V.A., Villa E., L'vov V.A. et al. Ultra-large tensile strains and martensite destabilization observed in high-temperature Ni57.5Mn22.5Ga20.0 single crystal // Art. in press. 3. Gomonaj E.V., L'vov V.A. Martensitic phase transition with two-component order parameter in a stressed cubic crystal // Phase Transitions. – 1994. – Vol. 47. – P. 9. 4. Kosogor A., L'vov V.A, Söderberg O., Hannula S-P. Stabilizing internal stress as the universal factor of martensite aging effects // Art. in press. 5. L'vov V.A., Kosogor A., Söderberg O., Hannula S-P. The symmetry-conforming theory of martensite aging // Mater. Sci. Forum. – 2010. – Vol. 635. – P. 13. 6. Ren X., Otsuka K. Origin of the rubber-like behavior in metal alloys // Nature. – 1997. – Vol. 389. – P. 579. 7 Saburi T., Nenno S., Fukuda T. Crystal structure and morphology of the metastable X phase in shape memory Ti-Ni alloys // Less Com. Metals. – 1986. – Vol. 125. – P. 157. 8. Sehitoglu H., Karaman I., Anderson R. et al. Compressive response of NiTi single crystals // Acta mater. – 2000. – Vol. 48. – P. 3311.

Submitted on 24.03.10

Наукове видання

ВІСНИК

КИЇВСЬКОГО НАЦІОНАЛЬНОГО УНІВЕРСИТЕТУ ІМЕНІ ТАРАСА ШЕВЧЕНКА

РАДІОФІЗИКА ТА ЕЛЕКТРОНІКА

Випуск 14

Друкується за авторською редакцією

Оригінал-макет виготовлено Видавничо-поліграфічним центром "Київський університет"

**Підписано до друку 04.10.10. Формат 60x84$^{1/8}$. Вид. № 156. Гарнітура Arial. Папір офсетний.
Друк офсетний. Наклад 300. Ум. друк. арк. 7,2. Обл.-вид. арк. 10,0. Зам. № 210-5376**

**Видавничо-поліграфічний центр "Київський університет"
01601, Київ, б-р Т. Шевченка, 14, кімн. 43
☎ (38044) 239 32 22; (38044) 239 31 72; (38044) 239 31 58; факс (38044) 239 31 28
e-mail: vpc@univ.kiev.ua**